Spectroscopic studies and characterization of laser produced plasmas

A THESIS

Submitted for the Award of Ph. D degree of

MOHANLAL SUKHADIA UNIVERSITY

in the

Faculty of Science

by

Bhavesh G. Patel

Under the Supervision of

K. P. Subramanian, Reader, Physical Research Laboratory, Ahmedabad

DEPARTMENT OF PHYSICS

FACULTY OF SCIENCE

MOHANLAL SUKHADIA UNIVERSITY

UDAIPUR

Year of submission: 2007

CERTIFICATE

I feel great pleasure in certifying that the thesis entitled *Spectroscopic studies and characterization of laser produced plasmas* *embodies a record of the results of investigations carried out by* *Mr. Bhavesh G. Patel* *under my guidance. I am satisfied with the analysis of data, interpretation of results and conclusions drawn.*

He has completed the residential requirement as per rules

I recommend the submission of thesis

Date:

Name and Designation of Supervisor

DECLARATION

I hereby declare that the work incorporated in the present thesis entitled "Spectroscopic studies and characterization of laser produced plasmas" is my own work and is original. This work (in part or in full) has not been submitted to any University for the award of a Degree or a Diploma

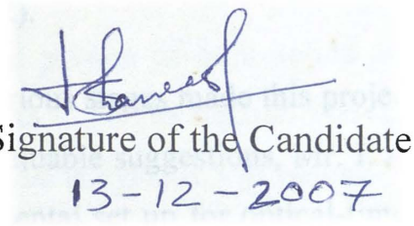

Signature of the Candidate

13-12-2007

Acknowledgements

"This morning I took out a comma and this afternoon I put it back in again."

Oscar Wilde

Gladly, the time has arrived to express my gratitude to everyone who helped me one way or other. I am deeply indebted to my supervisor Dr. K. P. Subramanian for all concern he has shown towards my research. I have greatly benefited by his immaculate knowledge of Physics and experimental acumen. In the same spirit I wish to express my gratitude to Dr. Ajay Kumar (IPR).

I am grateful to many other people whose help at various stages made this project possible. I sincerely thank Dr. B. Bapat for all his valuable suggestions, Mr. I. A. Prajapati for his support in establishing the experimental set up for optical-time-of-flight plasma spectroscopy, Mr. A. P. Gohil for his painstaking efforts to maintain laser and Mr. V. K. Lodha for his help during the experiments.

I thank Dharmesh, Vandana, Rajesh, and Nabi for providing an amicable atmosphere in lab and for all their help. I am thankful to the Dr. Rajesh, Sunil, Kiran, Kaushal, Ranjeet and Vishnu (IPR Team) whose wonderful company made the time I spent at IPR a memorable one.

Finally, I am grateful to Physical Research Laboratory for all its support and funding.

Abstract

A multitude of applications of pulsed laser ablation (PLA) of the solid targets has lead to an extensive research in the field of laser produced plasmas. The most successful and important applications include pulsed laser deposition of high temperature superconducting films without significantly changing the stoichiometry of superconducting material, elemental analysis of solids, production of atomic beams for reaction dynamics studies, nano-particle and cluster generation, and extreme-ultraviolet (EUV) lithography sources. The Knowledge of the mechanisms that lead to the formation and evolution of the plasma plume is of due importance in this context.

In this dissertation the evolution of laser generated plasma of bulk solids and multi-component LiF-C thin film have been dealt with in greater details. The role of atomic mass of plasma species in governing the plasma dynamics in vacuum as well as in ambient at pressure of 1 mbar of argon and the dynamics of carbon and lithium species in laser-blow-off plasma have been investigated. Besides this an attempt has been made to elucidate the role of ion dynamics in causing the splitting of plume into fast and slow components. The morphological difference between laser produced plasma and laser-blow-off plasma also form the subject of investigations for the present work. The present thesis also includes a discussion on the component specific analysis of the temporal profiles wherein a logistic approach has been propounded to numerically isolate the different velocity components of the species constituting the plasma plume.

Contents

List of Figures

List of Tables

Chapter 1
Introduction

1.1 Overview of laser produced plasma

The interaction of light with matter has been a subject of active research, both theoretically and experimentally for many years. With the advent of lasers, the pace of research in this field accelerated and it was soon realized that laser offered itself as a convenient tool to study the interaction of intense electromagnetic radiation with matter. Besides the fundamental aspects of laser-matter interaction, the multitude of applications of pulsed laser ablation (PLA) of the solid targets has attracted a great deal of attention. Major applications of PLA include inertial confined fusion [1], laser-based semiconductor fabrication [2], elemental analysis of solids [3], thin film deposition [4], nano-particle and cluster generation [5], extreme-ultraviolet (EUV) lithography [6], production of atomic beams for reaction dynamics studies [7] and laboratory simulation of astrophysical environment [8].

The understanding of the mechanisms that lead to the formation and evolution of the transient plasma plume is basic to the field of laser induced plasmas. Besides its growing application in applied fields, the study of the basic mechanism of ablation and plasma plume formation continues to be a challenging field. Laser pulses with pulse widths ranging from 10 to 100 ns and an energy fluence of 1–10 J /cm^2 are often used to produce plasma. The generation of plasma strongly depends not only on the laser parameters like wavelength, pulse duration and fluence and but also on the thermo-physical properties of the target. Extensive work has been done on the effect of laser parameters on generation and evolution of plasma plume [9, 10]. The main conclusion of these studies was that at low laser fluence, the ablation of matter by a nanosecond laser involves heating of the target up to melting point and then to vaporization point. However, for femto- or pico- second laser, the time duration of pulse is too short that the conduction of heat into the target is almost negligible and direct vaporization takes place. At higher laser fluence, the vapour temperature is high enough to

cause excitation and ionization of the atomic species. The ionized vapor then efficiently absorbs the laser radiation leading to a breakdown process, which marks the onset of plasma formation.

The absorption of light by matter depends on the processes at play. For transparent dielectrics devoid of any impurities and defects, the threshold intensity required to cause breakdown is very high. Here, the breakdown occurs when the electron generated by multiphoton ionization grow further by their impact on the neutrals or ions in the lattice and populate the conduction band [11]. In case of metals, the incident laser energy is first absorbed by the free conduction electrons which then transfer their energy to lattice vibrations via thermal equilibration process [12]. Generally, the absorption of laser light by the ablated cloud of material and its subsequent conversion to plasma is attributed to atomic processes like inverse bremsstrahlung and photoionization [13]. Other important processes that regulate the plasma plume are electron and ion impact processes, three body recombination and photo-recombination [13, 14]. The plasma plume being transient in nature, the plasma parameters like temperature and density are constantly evolving. The atomic processes discussed thus far are intimately related to plasma kinematics and hence their relative importance changes with time.

The expansion of plasma plume in vacuum and its interaction with the background gas is an equally complex hydrodynamic phenomenon. In vacuum, the plume is suggested to expand self-similarly with a constant plasma front velocity. Here it is assumed that initially the plume expands adiabatically and then isothermally during its later phase of evolution [15]. The evolution of plume in a background medium is quite complex and is usually explained jointly by drag and shock wave model. During initial stages of plume expansion, the plasma species are scattered by ambient gas atoms thereby emulating the drag or viscous effect. At latter stages when the pressure of background gas is equal to the plume pressure, the leading edge of plasma act like a piston and compresses the ambient gas. This compression causes formation of shock wave which evolves according to point blast wave model [16].

Numerous experimental and theoretical attempts have been made by many authors to model the physical processes involved in laser-solid interaction. In the models concerning the laser-solid interaction and plasma expansion, ablation of matter is usually simulated by thermal approach while processes like photoionization and inverse bremsstrahlung are invoked to estimate the absorption of laser light by plasma [17-19]. Besides this, collision processes like electron and ion impact processes and recombination processes have also been included to simulate the exact conditions of transient plasmas [20]. Such modeling enables one to study the temporal as well as spatial variation in plasma parameters like temperature, density, etc. Despite these efforts, the mechanisms involved in laser ablation and the expansion dynamics of the plume in vacuum as well as in background gas have yet to be understood in entirety to completely characterize the evolution of the plasma plume. The present thesis deals with dynamics of the plasma plume produced in two different configurations, *viz.* ablation from solids *vis-à-vis* from thin films. The interaction of laser is expected to exhibit remarkable differences in these two cases, due to the differences in length scale and time scale of laser interaction with matter. The thicknesses of the thin films are often less than the 'skin-depth', the penetration depth of the laser in corresponding bulk medium. Therefore, the ionization process in the film-ablated plume is expected to show more correlation with the laser parameters. We have effectively used this technique to explain the plume stratification due to which the evolving plume shows the presence of fast and slow moving components. The present thesis reports experimental results from the plume characterization studies which have provided detailed information with regard to plume stratification, onset of instabilities and ambient gas interaction with the evolving plume. The different expansion models are verified for different phases of expansion of the plume. The role of atomic mass of the target species on plume evolution is also studied.

1.2 Scope of the thesis

Laser-produced plasma being a rapidly expanding structure, the plasma parameters like velocity and temperature are transient in nature and evolve

quickly with respect to time and space. These parameters strongly depend on the experimental parameters like incident laser intensity and pulse duration, laser wavelength and ambient pressure. A host of physical mechanisms *viz.* laser absorption, evaporation, transient gas dynamics, radiation transport, condensation, ionization, and recombination involved in laser ablation and plasma formation makes the study of evolution of plasma all the more complex. This thesis deals with the evolution of laser generated plasma from solids (metals) and multi-component thin film. Most of the studies reported in literature have been carried out by using typical investigation techniques of atomic and molecular physics, such as optical emission spectroscopy [21, 22], laser induced fluorescence spectroscopy [23], time-of-flight (TOF) mass spectroscopy [24] and charge collection measurements [25]. Imaging of the plumes by ICCD camera [26, 27] also has been used to study the evolution of plasma plume. In the present work, optical time-of-flight spectroscopy technique has been employed to study the expansion dynamics of the plume. Besides plume splitting, the role of atomic mass of plasma species in governing the plasma dynamics in vacuum as well as in ambient at pressure of argon and the dynamics of carbon and lithium species in laser-blow-off plasma have been investigated in detail.

An attempt has been made to understand the phenomenon of plume splitting within the purview of the ion dynamics of the plume. Towards this, a comparative study of the temporal profiles of neutral and the ionic lithium species was carried out. The present thesis also deals with the influence of ambient medium on the dynamics of the plume. In this context, the regime of validity of the point blast wave and drag model were identified. Further, the temporal profiles of neutral species of various metals were studied to establish the dependence of the transition point on the atomic mass of the target. Transition point here refers to the spatial distance away from the target where the plasma plume changes from blast wave like expansion to drag like expansion. The effect of laser fluence on the evolution of plasma plume and the ionic composition of the plume has also been dealt with in the present work.

Scant studies are available on evolution of the neutral species of the plasma plume. In this regard, a non-intrusive optical time of flight spectroscopy has been employed to study the temporal evolution of the neutral at various distances away from the target. In order to infer the translational temperature of the neutral species, the temporal profiles were first transformed to the velocity domain. The present work includes an extensive treatment on the methodological aspects of fitting a Multi-Shifted-Maxwell-Boltzmann model to the velocity distribution of the neutral species and subsequently retrieving the relevant thermal parameters.

1.3 Outline of the thesis

This manuscript is organized into six chapters and the contents of each of these chapters have been briefly summarized below.

- Chapter 2 presents a brief review of the formation mechanisms of the laser produced plasma. Besides discussing the fundamentals of light absorption by matter and consequent heating of matter, a special emphasis is laid on the absorption and emissive processes that control the ignition of plasma.

- Chapter 3 discusses the evolution of plasma after the cessation of laser pulse. In this chapter various models concerning the expansion of plasma in vacuum as well as in background gas have been dealt with.

- Chapter 4 deals with the data analysis. This chapter begins the rationale behind using temporal profile as time-of-flight profile. Further, it includes a discussion on transforming a temporal profile into a velocity distribution of the species being probed. The chapter ends with a short discussion on a method to evaluate the kinetic energy of the plume species.

- Chapter 5 describes the experimental setup designed to study the expansion of plasma plume. Here, the necessary details regarding the optics, experimental chamber, target motion in vacuum, detector, and data acquisition system shall be presented.
- Chapter 6 concerns the observations made on the plasma plume of the solid targets. The evolution of plasma plume in vacuum and in the background gas forms the main theme of this chapter. Besides this, a methodology has been developed to isolate the different velocity components of the plasma plume and spatial variation in the component parameters has been studied.
- Chapter 7 encapsulates the important observations pertaining to the evolution of the plumes resulting from the bulk targets and thin films. It contains a discussion on the evolution dynamics of the Li and C species of the laser blow-off LiF plasma. A comparative study of Li I and Li II species has been made. In context of C II ion, an alternate mechanism explaining the plume splitting has been discussed. Besides plume splitting, the other relevant features like enhancement in intensity of plume emissions due to the plume-background gas interaction have been dealt with in greater details.
- Chapter 8 briefly summarizes the main outcomes of the thesis and also presents the future outlook for the thesis.

References

1. Epstein R., (1997). "Reduction of time-averaged irradiation speckle nonuniformity in laser-driven plasmas due to target ablation". *Journal of Applied Physics*, **82**(5): pp. 2123-2139.

2. Pearce C. W. and Zaleckas V. J., (1979). "A New Approach to Lattice Damage Gettering". *Journal of The Electrochemical Society*, **126**(8): pp. 1436-1437.

3. Lee W.-B., Wu J., Lee Y.-I., and Sneddon J., (2004). "Recent Applications of Laser-Induced Breakdown Spectrometry: A Review of Material Approaches". *Applied Spectroscopy Reviews*, **39**(1): pp. 27 - 97.

4. Chrisey D. B. and Hubler G. K., eds. *Pulsed Laser Deposition of Thin Films*. 1 ed. 1994, Wiley-Interscience: New York. 648.

5. Tillack M. S., Blair D. W., and Harilal S. S., (2004). "The effect of ionization on cluster formation in laser ablation plumes". *Nanotechnology*, **15**(3): pp. 390-403.

6. Stamm U., (2004). "Extreme ultraviolet light sources for use in semiconductor lithography—state of the art and future development". *Journal of Physics D: Applied Physics*, **37**(23): pp. 3244-3253.

7. Cross J. B. and Cremers D. A., (1985). "High kinetic energy (1-10 ev) laser sustained neutral atom beam source." *Nuclear Instruments and Methods in Physics Research, Section B: Beam Interactions with Materials and Atoms*, **13**(1-3): pp. 658-662.

8. Remington B. A., Arnett D., Paul R., Drake, and Takabe H., (1999). "Modeling Astrophysical Phenomena in the Laboratory with Intense Lasers". *Science*, **284**(5419): pp. 1488 - 1493.

9. Baseman R. J., Froberg N. M., Andreshak J. C., and Schlesinger Z., (1990). "Minimum fluence for laser blow-off of thin gold films at 248 and 532 nm". *Applied Physics Letters*, **56**(15): pp. 1412-1414.

10. Allmen M. V., *Laser-Beam Interactions With Materials: Physical Principles and Applications*. Springer Series in Materials Science, ed. D.M.B. Panish. 1986, New York: Springer-Verlag. 232.

11. Gamaly E. G., Juodkazis S., Nishimura K., Misawa H., Luther-Davies B., Hallo L., Nicolai P., and Tikhonchuk V. T., (2006). "Laser-matter interaction in the bulk of a transparent solid: Confined microexplosion and void formation". *Physical Review B –Condensed Matter and Materials Physics*, **73**: pp. 214101 (15 pages).

12. Radziemski L. J. and Cremers D. A., eds. *Lasers-induced Plasmas and Applications*. 1989, Marcel Dekker, Inc.: New York. 445.

13. Amoruso S., Bruzzese R., Spinelli N., and Velotta R., (1999). "Characterization of laser-ablation plasmas". *Journal of Physics B: Atomic, Molecular and Optical Physics*, **32**(14): pp. R131-R172.

14. Rosen D. I., Mitteldorf J., Kothandaraman G., Pirri A. N., and Pugh E. R., (1982). "Coupling of pulsed 0.35-μm laser radiation to aluminum alloys". *Journal of Applied Physics*, **53**(4): pp. 3190-3200.

15. Singh R. K. and Narayan J., (1990). "Pulsed-laser evaporation technique for deposition of thin films: Physics and theoretical model". *Physical Review B –Condensed Matter and Materials Physics*, **41**(13): pp. 8843 – 8859.

16. Amoruso S., Bruzzese R., Spinelli N., Velotta R., Vitiello M., and Wang X., (2003). "Dynamics of laser-ablated MgB_2 plasma expanding in argon probed by optical emission spectroscopy". *Physical Review B –Condensed Matter and Materials Physics*, **67**(22): pp. 224503.

17. Chen Z., Bleiner D., and Bogaerts A., (2006). "Effect of ambient pressure on laser ablation and plume expansion dynamics: A numerical simulation". *Journal of Applied Physics*, **99**(6): pp. 063304.

18. Bogaerts A., Chen Z., Gijbels R., and Vertes A., (2003). "Laser ablation for analytical sampling: what can we learn from modeling?" *Spectrochimica Acta Part B: Atomic Spectroscopy*, **58**(11): pp. 1867-1893.

19. Vertes A., Juhasz P., Wolf M. D., and Gijbels R., (1989). "Hydrodynamic modelling of laser plasma ionization processes". *International Journal of Mass Spectrometry and Ion Processes*, **94**(1-2): pp. 63-85.

20. Stapleton M. W., McKiernan A. P., and Mosnier J.-P., (2005). "Expansion dynamics and equilibrium conditions in a laser ablation plume of lithium: Modeling and experiment". *Journal of Applied Physics*, **97**(6): pp. 064904.

21. Abhilasha, Prasad P. S. R., and Thareja R. K., (1993). "Laser-produced carbon plasma in an ambient gas". *Physical Review E*, **48**(4): pp. 2929-2933.

22. Kerdja T., Abdelli S., Ghobrini D., and Malek S., (1996). "Dynamics of laser-produced carbon plasma in an inert atmosphere". *Journal of Applied Physics*, **80**(9): pp. 5365-5371.

23. Nakata Y., Kumuduni W. K. A., Okada T., and Maeda M., (1995). "Two-dimensional laser-induced fluorescence imaging of non-emissive species in pulsed-laser deposition process of $YBa_2Cu_3O_{7-x}$". *Applied Physics Letters*, **66**(23): pp. 3206-3208.

24. Choi Y.-K., Im H.-S., and Jung K.-W., (1999). "Temporal Evolution and Ablation Mechanism of Laser-induced Graphite Plume at 355 nm". *The Bulletin of the Korean Chemical Society*, **20**(12): pp. 1501.

25. Amoruso S., Armenante M., Berardi V., Bruzzese R., Pica G., and Velotta R., (1996). "Chargel species analysis as a diagnostic tool for laser produced plasma characterization". *Applied Surface Science Proceedings of the Second International Conference on Photo-Excited Processes and Applications*, **106**: pp. 507-512.

26. Harilal S. S., Bindhu C. V., Tillack M. S., Najmabadi F., and Gaeris A. C., (2003). "Internal structure and expansion dynamics of laser ablation plumes into ambient gases". *Journal of Applied Physics*, **93**(5): pp. 2380-2388.

27. Geohegan D. B. and Puretzky A. A., (1995). "Dynamics of laser ablation plume penetration through low pressure background gases". *Applied Physics Letters*, **67**(2): pp. 197-199.

Chapter 2

Plasma formation by laser-matter interaction

2.1 Introduction

The nature of the interaction of laser with matter is largely governed by the properties of the matter and incident laser parameters. When an intense laser pulse is focused on the target, the breakdown of target may take place which is generally characterized by an appearance of a luminous plasma plume. The threshold power density required to produce such a plume depends not only on the laser parameters like wavelength and pulse duration but also on the thermophysical properties of the target material. Knowledge of the mechanisms that lead to the formation and evolution of the plasma plume is of due importance in this context. Further, the understanding of the atomic processes is important from the view point that the plasma parameters like temperature, density and velocity, which have important bearing on various applications of laser produced plasma, critically depend on the amount of laser energy coupled to the target. The present chapter briefly overviews the phenomenon of absorption of light by matter and the various atomic processes that take place in the plasma plume. Section 2.2 deals with absorption of light by solids *viz.* metals and dielectrics. Section 2.3 describes the heating of target due to absorption of light. Here, on the basis of the diffusion length, the ablation of target has been categorized into surface ablation and volume ablation. Finally, section 2.4 describes the other relevant atomic processes and their significance as the plasma evolves.

2.2 Absorption of light by matter

The interaction of laser with a matter depends largely on the nature of the target material. Depending on the property of the solid target, the absorption of light can be attributed to either of the below mentioned mechanisms [1].

1. Intra-band absorption and contribution of free charge carriers in metals and semiconductor.

2. Inter-band transitions and molecular excitations..
3. Absorption by collective excitations (excitons, phonons).
4. Absorption due to impurities and defects.

On the basis of the response of solids to the laser radiation, they can be categorically classified into transparent and absorptive solids [2]. In this context, the term transparent refers to those classes of solids for which the absorption length is very long even at low irradiance while absorptive solids are those for which the absorption length is small.

For transparent dielectrics devoid of impurities and defects, the breakdown due to laser-matter interaction takes place at very high values of incident laser intensity [2]. The destruction of dielectric by laser obviates absorption of some of the incident energy. Such absorption is only explicable if one considers the generation of electron-hole pairs. Generation of electron hole pair in a dielectric is mainly governed by wavelength and intensity of the incident laser beam. The absorption is more prominent at lower values of wavelength where the photon energy exceeds the band gap value of the concerned dielectric. It is important to notice that the laser induced breakdown is very similar to that of gases. Here, the band gap of dielectric plays the same role as the ionization potential of the gas. As most dielectrics have a band gap of order of 5 eV, it is not possible to cause breakdown of dielectrics by visible or infrared light. However, breakdown does occur at these wavelengths when the intensity of the incident laser is very high. Such a breakdown is explicable only when one considers nonlinear mechanisms like multiphoton ionization (MPI) and electronic avalanche (EA) [3]. MPI can be described by the reaction

$$M + mh\nu \rightarrow M^{+} + e^{-} \tag{2.1}$$

If E_g represent the band gap energy between conduction and valence band, the minimum number of photons (m) required to cause ionization is given by

$$m = \text{integer part of} \left\{ \frac{E_g}{h\nu} + 1 \right\} \tag{2.2}$$

In order to have an estimate of the wavelength regime in which the above process is relevant, consider a dielectric having a band gap of 5 eV being irradiated by infrared light (wavelength~10μm). The number of photons required to cause ionization turn out to be ~50. Simultaneous absorption of 50 photons is highly improbable. Thus MPI is relevant only at wavelengths shorter than 1μm. EA is an alternate mechanism which can lead to breakdown of dielectric. A few electrons are already present in the conduction band due to presence of impurity in the dielectric. These conduction band electrons acquire enough energy from the ambient field to promote the electrons in the valence band to conduction band by means of impact ionization. The nonlinear processes discussed thus far work in unison to cause breakdown of dielectric. MPI creates initial 'seed' electrons which then multiply rampantly by means of electronic avalanche.

Specifically, in case of semiconductors, the absorption of photon of appropriate energy leads to creation of free carriers *viz.* electrons and holes with certain kinetic energy. Both these carriers now contribute to the absorption coefficient. Once these energetic carriers equilibrate and attain a common carrier temperature, they transfer their energy to the lattice via recombination and phonon generation, thereby causing lattice heating and melting.

In metals, the photon-matter interaction begins with the absorption of the photons by the conduction band electrons. The deposited energy is quickly (within femtoseconds) equilibrated among the electrons. The energy of the electron is then transferred to the lattice vibrations. This process takes place rather slowly and is controlled by the strength of the electron-phonon coupling. It can take from fractions of a picosecond to several tens of picoseconds. Finally, a thermal equilibrium is established between the electrons and phonons, and the common thermal diffusion can be used to describe the heat flow into the bulk of the irradiated target. For metals, the absorption coefficient is close to zero for radiation with frequencies smaller than the plasmon frequency and it increases with increase in the frequency of the radiation. The absorption coefficient is very high in the entire wavelength ranging from 10μm to 100nm. Thus the overall effect of the photon-matter interaction is to heat the solid. If the intensity of the

laser pulse is sufficiently high, enough heat may be generated so as to cause evaporation. The removal of the material by an intense laser is often referred to as ablation. The ablation threshold not only depends on the wavelength and the intensity of the incident laser pulse, but also on the thermo-physical parameters like cohesive energy and thermal conductivity of the metal under study. The cohesive energy for *sp*-bonded metals like Pb and Cd is less than 3 eV per atom. For such metals the ablation threshold energy can be as low as 0.1 J/cm^2 [4]. The transition metals like Ti, Fe and Co and noble metals like Ag or Au have intermediate binding energies ranging from 3-5 eV per atom and these metals have intermediate ablation threshold. Typically, the ablation threshold for Cu, when irradiated by 1064 nm/10 ns laser pulses, is found to be 2 J/cm^2. The refractory metals like Mo, Re and W have the binding energy in excess of 6 eV per atom. The ablation threshold of these metals can be as high as 10 J/cm^2 [4]. Thus except for the *sp* bonded metals, the ablation threshold for most metals are about an order of magnitude greater than that for the materials with a band gap. The threshold fluence to cause ablation is often achieved by focusing the laser beam to a small spot.

The intensity of the incident laser light at a point within the surface of the target is often given by Beer-Lambert law [5].

$$I(z) = (1-R) I_0 e^{(-\alpha z)} \tag{2.3}$$

Here I_0 is the intensity of the incident light. R and α are the reflectivity and the absorption coefficient. z is the distance measured normal to the target. For most metals the attenuation length ($1/\alpha$) is typically around 10 nm. It is important to note that the above relation is only correct approximately as the reflectivity and the absorption coefficient strongly depend on the roughness and the temperature of the surface respectively. Hence the end result of the interaction of laser beam with matter is its heating to very high temperatures.

2.3 Heating and melting of target surface

As described in earlier section the absorption of the laser light by matter can briefly be summarized in three points:

1. The absorption of the laser photons *via* electronic excitations in metals or *via* inter-band transitions in semiconductors and insulators.
2. Equilibration of energetic carriers and transfer of energy to lattice.
3. Heating of target and dissipation of energy by means of conduction.

The heating of the target due to pulsed laser matter interaction causes the surface temperature of the target to rise up to several thousands Kelvin. For most materials, the temperature of the surface reaches the melting and boiling point in a fraction of a nano-second. In the case where femto-second laser pulses are used the rise in temperature is even faster.

The conduction of the heat produced at the target surface is described by the equation [5]

$$\rho(T)c_p(T)\frac{\partial T(z,t)}{\partial t}-\nabla\left[\kappa(T)\nabla T(z,t)\right]= (1-R)I_0(t)\alpha e^{-(\alpha z)} \tag{2.4}$$

where the term on the left hand side represents the energy deposited at the target surface. $\rho(T)$, $\kappa(T)$ and $c_p(T)$ are the mass density, thermal conductivity and specific heat of the target respectively. For conducting materials, there is a significant diffusion of the energy deposited by the laser light on the target surface. Thermal diffusivity and heat diffusion length are the two important parameters that characterize the loss of the deposited energy due conduction. These parameters are defined as follows

$$\text{Thermal Diffusivity (D)}: \quad D=\frac{\kappa}{\rho c_p} \tag{2.5}$$

$$\text{Heat diffusion length } (L_{th}): \quad L_{th}=2(D\tau_L)^{1/2} \tag{2.6}$$

where τ_L is the pulse width laser pulse. The typical values of the absorption length and thermal diffusion length, in case of silver target irradiated by a 6 ns laser pulse at wavelength, are 20 nm and 1μm respectively. It is evident that for the highly conducting metal (silver) the thermal diffusion length is several orders of magnitudes larger than the absorption length. A detailed investigation was carried out by Matthias et al.[6] to study the correlation between thickness of the target film and the fluence thresholds for melting and evaporation. It was observed that the fluence linearly depended on the thickness of the film as long as the thickness of the target is larger than the optical absorption length and smaller than the heat diffusion length. In fact, the ablation of the target can be distinctly categorized into two regimes *viz.* surface heating regime and volume heating regime. The occurrence of ablation in either of these regimes is governed by laser parameters and thermophysical properties of the target [7]. Surface heating regime is defined as one in which the optical absorption depth is much smaller than the thermal diffusion distance i.e. $\alpha\sqrt{2Dt_p} \gg 1$ while in volume heating regime the optical absorption depth is much larger than the thermal diffusion distance i.e. $\alpha\sqrt{2Dt_p} \ll 1$. In surface heating the laser energy is absorbed in the surface layer and the thermal diffusivity controls the heating and ablation characteristics. Here, the vaporization interface formed during ablation propagates from the surface into the bulk of the target. However, for larger values of the fluences, sub-surface heating also takes place causing explosive removal of material from the target. Contrary to the case discussed above, when the optical absorption length of the laser light is very large compared to the thermal diffusion length, the ablation depth is determined by the optical absorption length. In this regime the laser light penetrates deep into the surface leading to volumetric removal of the particles [7].

For insulators, the depth up to which the laser energy is deposited is solely determined by the absorption length. Owing to negligible heat conduction, the surface temperature rises rapidly for insulators than for the metals. For the values of the laser light fluence ranging from 1-10 J/cm^2, the ablation yield varies from around 10^{15} to 10^{16} atoms/pulse. A detailed investigation of pulsed laser ablation by a nanosecond pulses with fluence at the value 9 J/cm^2 revealed that

immediately after the laser pulse is extinguished, the temperatures within the plasma will be around 2×10^4K. In the initial stage of formation, thickness of the plasma is around a fraction of a millimeter. Assuming the particle density at this stage to be 10^{15} particles per pulse and that the plasma follows ideal gas equation, the pressure of the plasma plume is estimated to be around 10^9 Pa [8]. The high pressure gradient between the plasma plume and the ambient gas drives its violent expansion in vacuum or in the background gas.

2.4 Absorption and emission processes in plasma plume

When laser beam is focused on the target, the energy density at the target surface can be as high as 1-10 J/cm^2 depending on the laser parameters. Such a high energy density causes the temperature of the target surface to exceed the melting point of the target. However, this temperature cannot account for the degree of ionization observed in the plasma plume. For a gas at local thermodynamic equilibrium, the density of the singly ionized species in cm^3 is given by Saha's equation [8].

$$n_i = \left(2.4\times10^{15}\, T^{3/2}\, n_n\, e^{U_i/kT}\right)^{1/2} \tag{2.7}$$

where T is gas temperature in K, n_n is the gas density of neutrals (in cm^3), and U_i is the first ionization potential of the gas atoms in electron volts. Willmott [8] modeled the degree of ionization of the plasma of a titanium target. He considered the Gaussian laser pulse with 20 ns pulse width, creating an energy density of 10 J/cm^2 at the surface of the target. Assuming the temperature of the plasma to be vaporization temperature (T=3562 K), the numeric of equation (2.5) indicate that the degree of ionization of the plasma is less than 10^{-3}. However, the degree of ionization, as observed experimentally, in the initial stage of plasma formation is found to be between 0.1 and 1. Such a high degree of ionization is only plausible at a temperature around 10^4K. Since the initial plasma temperature is much less than 10^4K, the observed degree of ionization cannot be explained by mere thermionic emission of positive ions and electron due to heated surface. The unexpected ionization of the plume has been attributed to the higher temperatures

induced by absorption of laser light by the ablated material. The absorption of laser by plasma depends on the electron-ion density, temperature and wavelength of the laser light. For absorption to take place, the plasma frequency should lower than the laser frequency. The plasma frequency is given by [7]

$$\nu_p = 8.9\times10^3 n_e^{0.5} \tag{2.8}$$

Here n_e is the electron concentration of plasma. To illustrate the role of electron density in absorption of laser beam, consider the ablation of target by excimer laser. Using above relation the value of the critical density turns out to be $1\text{-}3\times10^{22}/cm^3$. This means that if the density of electrons in the plasma exceeds this value, there will be no further absorption. In present case, the density of plasma gradually decreases away from the target owing to the plasma expansion and hence the plasma density always remains lower than the critical plasma density. The losses due to reflection of the laser beam are insignificant and can be neglected. Besides this, the ablated cloud of target material is further heated by non-thermal processes like inverse bremsstrahlung (IB) and photoionization (PI). These processes largely depend on the intensity and wavelength of the laser pulse used for ablation. If the intensity of the incident laser pulse is low (<1 J/cm^2), the temperature of the ablated material is too low for it to interact with the laser pulse. The laser beam passes unattenuated through the ablated vapor cloud. In this regime the main outcomes of laser-target interaction are heating, melting and vaporization of the target. When the intensity of the incident laser beam is high (1-10 J/cm^2), the temperature of the target surface rises to a point where there is appreciable atomic excitation and ionization. In this regime, there is substantial absorption of laser energy by the vapor species which causes vapor breakdown and plasma formation. The two dominant photon absorption processes involved in plasma formation are IB and PI. In IB, free electrons gains energy by absorbing laser photons under the influence of two-body potentials of electron-neutral/ion scattering. The probability of the photon absorption due to electron-ion collisions is far exceeds that due to electron-neutral collision. However, the large density of neutral in the initial stage of plasma formation significantly increases IB

absorption of photons *via* electron-neutral scattering. The IB cross-sections due to electron-ion and electron-neutral are given by [9]

$$\sigma_{ion} \approx 1.27\times10^{-46}\, Z^2\, \lambda^3\, T_e^{-0.5}\, N_i \left[1-e^{(h\nu/T_e)}\right] \tag{2.9}$$

$$\sigma_{neu} \approx 2.2\times10^{-32}\, \sigma_{coll}\, \lambda^2\, T_e^{-0.5}\, N_n \tag{2.10}$$

where λ is the laser wavelength in nm, T_e is the electron temperature in eV, $h\nu$ is the energy of the laser photon in eV, Z is the ionic charge, N_i and N_n are number densities of ions and neutrals respectively and σ_{coll} is the cross-section for electron-neutral collisions in cm^2.

The efficacy of the IB process to absorb photon is often expressed in terms of IB absorption coefficient α_{IB} as given below.

$$\alpha_{IB} = \sigma_{IB} N_e = \left(\sigma_{neu} + \sigma_{ion}\right) N_e \tag{2.11}$$

where N_e is the electron density in cm^{-3} and σ_{IB} (cm^2) is the total cross-section of the process and it includes the contribution from ions and neutrals.

It is evident from equation (2.6) and (2.7) that IB process is less efficient in the UV region than in the visible and IR region. However, as IB process depends on the number densities of ions and neutrals, it is apparent that it also depends on the thermo-physical properties of the target material. In order to illustrate this consider the ablation of a solid target by CO_2 laser. For laser pulse with wavelength at 1064 nm σ_{IB} is higher than 10^{-19} cm^{-2} for a very low plasma temperature and electron density [10]. At this wavelength, the laser intensity of $10^7 Wcm^{-2}$ corresponds to 5×10^{25} photons $cm^{-2}s^{-1}$. The product of photon flux and cross-section of IB gives the probability of 50% for an IB photon absorption in 10ns. The energetic electrons produced by the virtue of IB further collide with excited and ground state atoms causing their ionization and excitation.

Besides IB, photoionization (PI) play a vital role in increasing the degree of ionization of the vapor cloud. PI is particularly important in visible and UV

laser ablation of metals. In fact, an approximate expression for photoionization cross-section is given by [9]

$$\sigma_{PI} \approx 2.9\times10^{-17}\frac{\left(\varepsilon_I-\varepsilon^*\right)^{2.5}}{\left(h\nu\right)^3} \tag{2.12}$$

where ε_I is the ionization potential of the atom and ε^* is the energy of the excited state in which the atom to be ionized resides. It is to be noted that all the energy terms appearing in above equation are in eV. An important caveat in using above equation is that $h\nu > \varepsilon_I - \varepsilon_I^*$. The efficacy of the photons to ionize the excited atoms is evident from above equation. The energy of the UV and visible photon is of same order as the ionization energy of the excited metal atoms making the energy terms in numerator and denominator of equation (2.9) almost equal. Hence the PI cross-section turns out to be of order of 10^{-17}cm^2. With very high laser intensities the probability of atom being ionized by UV photon almost becomes 1.

The above two processes together increase the degree of ionization. In this context it is worth mentioning that electron impact (EI) excitation and ionization time constants are of order of 0.1 ns. Hence, a laser pulse with a pulse width around 10 ns provides sufficient time for considerable enhancement in the population of excited and ionized species. The resultant increase in the number densities of electron and ionized species leads to an increased probability of photon absorption by IB due to electron-ion collision.

Besides the absorption mechanisms described above, the other important chemical and radiative processes within the plasma can be broadly categorized as electron and ion impact processes. The possible processes in typical laser produced plasma are listed next [11].

1. electron-impact excitation and deexcitation of neutral atom

$$A+e+\Delta E \rightleftharpoons A^+ + e$$

2. ionization of ground state atom and three-body recombination into ground state

$$A + e + \Delta E \rightleftharpoons A^+ + 2e$$

3. ionization of excited state atom and three-body recombination into an excited state

$$A^* + e + \Delta E \rightleftharpoons A^+ + 2e$$

4. radiative quenching of excited atom and reabsorption of this resonant photon

$$A^* \rightleftharpoons A + h\nu$$

5. photorecombinitation and photoionization by reabsorption of this resonant photon

$$A^+ + e \rightleftharpoons A + h\nu$$

6. collisional relaxation of electrons and heavy-body temperatures

7. excitation, ionization, deexcitation, and recombination through atomic and ionic collisions

$$A + A + \Delta E \rightleftharpoons A^* + A$$
$$A + A + \Delta E \rightleftharpoons A^+ + A + e$$
$$A + A^* + \Delta E \rightleftharpoons A^+ + A + e$$
$$A^+ + A + \Delta E \rightleftharpoons A^* + A^+$$
$$A + A + \Delta E \rightleftharpoons A^+ + A^+ + e$$
$$A^+ + A^* + \Delta E \rightleftharpoons A^+ + A^+ + e$$

Of all the processes listed above the important processes that counter balance the electron enhancing mechanisms in the plasma plume are three-body recombination (TBR) and photo-recombination (PHR) [10]. The absorption of photons by IB is primarily governed by the recombination time constants of these

processes. If the recombination time constants are equal to or larger than the duration of the laser pulse, then the electrons effectively absorb energy by IB. in order to understand the relevance of these recombination processes at various stages of plasma evolution, consider the expression for their relaxation times [10].

$$\tau_{TBR} \approx 1.1\times10^{26}\, Z^{-3}\, T_e^{9/2}\, N_e^{-2} \tag{2.13}$$

$$\tau_{PHR} \approx 3.7\times10^{12}\, Z^{-2}\, T_e^{3/4}\, N_e^{-1} \tag{2.14}$$

The electron densities and electron temperature in a typical plasma is around 10^{18}-10^{20} $cm^{-3}$and several eV respectively. Under these conditions the recombination time constant of TBR is much smaller than that of photoionization and hence TBR is a dominant recombination process. As plasma evolves, its density as well as temperature decreases. Thus at latter times when plasma has expanded in space, the PHR becomes an important over TBR.

The above discussed ionization and recombination processes work in unison and decide the effective degree of ionization of the laser produced plasmas. Further, these processes are governed by the plasma parameters *viz.* electron density and the temperature and the incident flux at the target surface. The processes discussed thus far not only decide the degree of ionization of the plume but also serve as marker for important plume phenomena like plume splitting. The effect of laser intensity on population density of the ions in the plume and the relation between fast velocity component and the atomic processes has been explored chapter 7.

References

1. Gamaly E. G., Juodkazis S., Nishimura K., Misawa H., Luther-Davies B., Hallo L., Nicolai P., and Tikhonchuk V. T., (2006). "Laser-matter interaction in the bulk of a transparent solid: Confined microexplosion and void formation". *Physical Review B –Condensed Matter and Materials Physics*, **73**: pp. 214101.

2. Radziemski L. J. and Cremers D. A., eds. *Lasers-induced Plasmas and Applications*. 1989, MARCEL DEKKER, INC.: New York. 445.

3. Quéré F., Guizard S., and Martin P., (2001). "Time-resolved study of laser-induced breakdown in dielectrics". *Europhysics Letters*, **56**(1): pp. 138-144.

4. Chrisey D. B. and Hubler G. K., eds. *Pulsed Laser Deposition of Thin Films*. 1 ed. 1994, Wiley-Interscience: New York. 648.

5. Allmen M. V., *Laser-Beam Interactions With Materials: Physical Principles and Applications*. Springer Series in Materials Science, ed. D.M.B. Panish. 1986, Berlin: Springer-Verlag. 232.

6. Matthias E., Reichling M., Siegel J., Käding O. W., Petzoldt S., Skurk H., Bizenberger P., and Neske E., (1994). "The influence of thermal diffusion on laser ablation of metal films". *Applied Physics A: Materials Science & Processing*, **58**(2): pp. 129-136.

7. Singh R. K. and Kumar D., (1998). "Pulsed laser deposition and characterization of high-T_c $YBa_2Cu_3O_{7-x}$ superconducting thin films". *Materials Science and Engineering: R: Reports*, **22**(4): pp. 113-185.

8. Willmott P. R. and Huber J. R., (2000). "Pulsed laser vaporization and deposition". *Reviews of Modern Physics*, **72**(1): pp. 315 - 328.

9. Amoruso S., (1999). "Modeling of UV pulsed-laser ablation of metallic targets". *Applied Physics A: Materials Science & Processing*, **69**(3): pp. 323-332.

10. Amoruso S., Bruzzese R., Spinelli N., and Velotta R., (1999). "Characterization of laser-ablation plasmas". *Journal of Physics B: Atomic, Molecular and Optical Physics*, **32**(14): pp. R131-R172.

11. Rosen D. I., Mitteldorf J., Kothandaraman G., Pirri A. N., and Pugh E. R., (1982). "Coupling of pulsed 0.35-μm laser radiation to aluminum alloys". *Journal of Applied Physics*, **53**(4): pp. 3190-3200.

Chapter 3

Gas dynamics of laser produced plasmas

3.1 Introduction

This chapter deals with the gas dynamics of the plasma formed at the end of laser pulse. It provides a brief review of various models which explain the evolution of plasma plume in vacuum as well as in ambient argon environment at various pressures. The evolution of the plume is largely governed by the nature as well as the pressure of the ambient gas. While in vacuum the expansion of plume is explained by free-expansion model, a combination of drag and point blast wave model is needed to understand the expansion of plasma in ambient medium. The expansion of plasma in vacuum has been treated in considerable detail in section 3.1. In section 3.2 the expansion of plume in ambient gas environment is discussed. Here, the theory of point blast wave model and drag model has been discussed in greater detail.

3.2 Expansion of plasma plume in vacuum

The course of plasma evolution, after the laser pulse extinguishes, is largely decided by the intensity of the incident laser beam. If the intensity of the laser pulse is low, less ablation takes place and as a result a collisionless low density vapor cloud is formed in front of the target. In such a case the angular distribution of the expanding vapor atoms is described by thermal $cos(\theta)$ law and the velocity distribution of plasma constituents follows a Maxwellian function limited to half-space.

However, if the laser intensity is high, the amount of the matter ablated increases and a high density vapor cloud is formed at the target surface. The increased density of cloud leads to larger number collision which causes the formation of Knudsen layer where half range Maxwellian velocity distribution function of the vapor atoms is transformed into a full range Maxwellian with a center-of-mass velocity in the direction perpendicular to the target surface.

Interestingly, it has been found that only 3-5 collisions per particle, a condition common in most pulsed laser deposition processes involving moderate fluences, are enough for such an equilibration to happen [1]. An overview of the processes involved in equilibration of the vapor cloud at the surface is presented in the below figure.

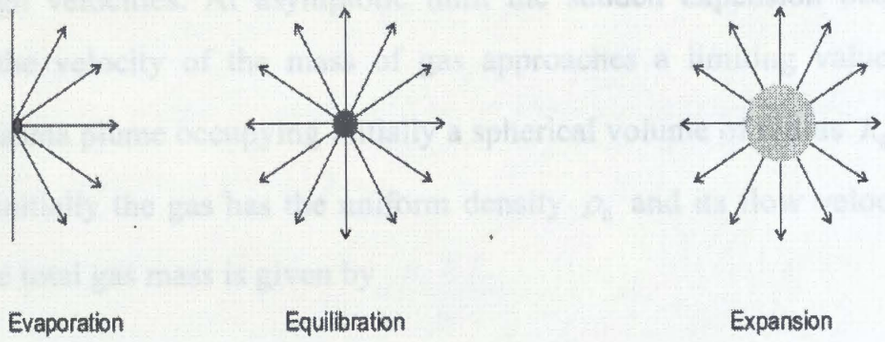

Figure 3-1 Various stages of plasma plume evolution. The arrows represent the expansion of the plasma species. Initially, the whole of the energy of the gas cloud generated at solid surface is in form of thermal energy. During equilibration phase the collisions among the plasma species convert the thermal energy of plasma into its kinetic energy. Finally, the system relaxes to MB behavior in its COM system and subsequently the gas cloud expands.

For larger laser fluences more than one monolayer of the target is ablated. As the quantity of the ablated particles is larger, the flow evolves into an 'unsteady adiabatic expansion' (UAE). This regime of expansion is marked by prominent peaking of the ablated particle in forward direction. In this regime, the distribution of the ablated particles can scale anywhere between $\cos^8\theta$ to $\cos^{30}\theta$ [1].

The problem of the plasma plume expansion closely resembles the sudden unsteady adiabatic expansion of a spherical gas cloud into vacuum. In vacuum, where the mean free path of the plasma particle is much longer than the dimensions of the vacuum system, the adiabatic expansion of plasma takes place and the temperature and the dimensions of the plume are related by the thermodynamic relation [2].

$$T\left[X(t)\,Y(t)\,Z(t)\right]^{\gamma-1} = const \qquad (3.1)$$

where γ is the ratio of the specific heat capacities at constant pressure and volume and $X(t), Y(t)$, and $Z(t)$ are the dimensions of the expanding plasma at time t. As evident from relation (3.1), the temperature of the plasma drops off rapidly as the plasma expands. The thermal energy of the plasma is rapidly converted into the kinetic energy as result of which the plasma front acquires extremely high velocities. At asymptotic limit the sudden expansion becomes inertial and the velocity of the mass of gas approaches a limiting value u_{max}. Consider a plasma plume occupying initially a spherical volume of radius R_0. We assume that initially the gas has the uniform density ρ_0 and its flow velocity is zero. Thus the total gas mass is given by

$$M = \frac{4}{3}\pi R_0^3 \rho_0 \tag{3.2}$$

Assuming the initial pressure of the cloud to be uniform with a value p_0, the total energy of the gas at the time when the plasma plume has just been formed (time $t = 0$) is

$$E_0 = \left[\frac{\gamma}{1-\gamma}\right] \frac{4}{3}\pi R_0^3 \, p_0 \tag{3.3}$$

It is to be noted that the time when plasma just formed the total energy of the plume exists as the thermal energy. At time $t = 0$ the plasma cloud starts expanding in the vacuum. In this process of expansion, work is done by the expanding gas. During the expansion process the gas is accelerated, and its initial internal energy E_0 is gradually transformed into kinetic energy of radial motion. The motion is isentropic since we have ignored heat conduction and viscous stress of the gaseous plume. Finally, when sufficient time has elapsed, the whole of the thermal energy is converted to the kinetic energy and the energy of the plume is then expressed as

$$E_f = \frac{1}{2} M u_{max}^2 \tag{3.4}$$

Now since the energy needs to be conserved we must have

$$E_0 = E_f \tag{3.5}$$

Using Eqs. (3.2),(3.3),(3.4) and (3.5), one obtains the relationship

$$u_{\max} = \sqrt{\frac{2\gamma}{\gamma-1}}\sqrt{\frac{p_0}{\rho_0}} \tag{3.6}$$

As the plasma plume is assumed to be an ideal gas at temperature T_0, the equation-of-state equation is given by

$$p_0 = \frac{\rho_0 R T_0}{w} \tag{3.7}$$

Here w is the molecular weight of the plasma species and R is gas constant. Substituting Eq. (3.7) in Eq. (3.6), the maximum velocity of the plasma front turns out to be

$$u_{\max} = \sqrt{\frac{2\gamma R}{\gamma-1}}\sqrt{\frac{T_0}{w}} \tag{3.8}$$

Thus, the expansion of the plasma plume is characterized by a constant expansion velocity which not only depends on the energy of the plasma plume but also on the mass of the plasma species. The position of the plasma front at any time t is then written as

$$R(t) = u_{\max} \times t + R_0 \tag{3.9}$$

where $R(t)$ is the position of the plasma front at time t and R_0 is a constant.

3.3 Expansion of plasma in ambient gas

The evolution of plasma plume in a buffer gas above a certain pressure is a far more complicated gas dynamic process as compared to the expansion of plume in vacuum. It involves physical processes such as deceleration, attenuation, thermalization of the ablated species, diffusion, recombination, formation of

shock waves, and clustering [3-6]. Besides these processes, the buffer gas notably influences the plume chemical kinematics [7]. In this context it is important to notice that the mean free path of the plasma species strongly depends on the buffer gas pressure. For instance, the mean free path of the magnesium atom with kinetic energy of tens of eV in an argon background ranges from few tens of cm at 10^{-3} mbar to a tenth of mm at 1mbar of argon [8]. Depending on the ambient pressure condition, the expansion of the plasma plume in vacuum is often described by a point blast wave model and the drag model. A brief overview of these models and their validity is discussed next.

3.3.1 Point-blast-wave model

The expansion of plasma plume in the ambient pressures greater than 1 mbar leads to formation of shock wave. The generation of shock wave depends not only on the ambient pressures but also on other factors like molecular weight of the plume and background species, initial plume velocity, and density [9]. When a high-pressure plume expands, it compresses the surrounding gas, thereby acting like a piston. The braking effect of the background gas on plume expansion becomes prominent when the plasma plume pressure becomes comparable to the pressure of the gas surrounding the plume periphery. Such a braking effect of the ambient gas causes the nonlinear dependence of the plume front position on time [10]. It is important to note that the energy required for the generation of the shock wave is provided through collisions of the energetic ablated particles with the ambient gas atoms. This process leads to plume thermalization, thereby making the energy distribution of plasma particle isotropic. Thermalization of plume further leads to a hemispherical shape of the shock wave which propagates through the buffer gas.

The problem of plasma expansion in buffer gas closely resembles the classical problem of strong explosion in a homogenous atmosphere. The propagation of strong shock also known as blast wave produced due to strong explosion was first studied by Taylor and Sedov. The Sedov-Taylor model holds good only when the following two conditions are satisfied [11].

- The incident energy is dissipated in a volume that is very small as compared to the dimensions of the plume. *i.e.* explosion must involve a point source release.

- The energy liberated in the explosion must be very large so that the ambient pressure is negligible in comparison to the pressure of the plasma plume. In other words the explosion energy must far exceed the internal energy of the gas which has been set in motion.

In view of the above conditions, we consider a perfect gas with constant specific heats and density ρ in which a large amount of energy E has been released in a small volume during a short time interval. In order to meet the requirement restricting the mass of the ambient gas set in motion by shock wave to be greater than mass of the plasma plume, we consider the explosion at a stage when the shock wave has moved a distance which is large in comparison to the dimensions of the region where explosion has occurred. It is must be remembered that the shock wave should not have moved too far away from the point of explosion otherwise the pressure in the plume will be less than the ambient pressure thereby violating the second condition. With these prime conditions the expression for the position of a strong shock (plume front) in a one-dimensional flow shall be derived [12].

Consider an expression for the conservation of the energy of the plasma plume.

$$E = C_N \int_0^{R(t)} \left[\frac{1}{2} u^2 + e \right] \rho \, r^N dr, \quad N = 0, 1, 2 \tag{3.10}$$

where E is the initial energy release, ρ, u, and e are the mass density, flow speed, and specific internal energy, respectively behind the shock front. C_N and N are the geometrical factors whose values are enlisted below

Geometry of Propagating wave	N	C_N
Plane	0	Cross-sectional Area of plane wave (A)
Cylindrical	1	$2\pi \times$ length of cylindrical wave (2πL)
Spherical	2	4π

Table 3-1 The geometry factors C_N and N for wave with different geometries.

The Figure 3-2a depicts a discontinuity (shock wave) traversing the medium towards right with the velocity v_0 in the frame of reference of the undisturbed medium. Here, ρ_0, T_0, and P_0 are the density, temperature and pressure of the unperturbed medium while ρ_1, T_1, and P_1 are the density, temperature and pressure behind the shock wave. When viewed from the frame of reference of the shock wave, the unperturbed medium advances the shock wave at velocity v_1, while the shocked medium recedes away from the shock wave at the velocity v_0 (*cf.* Figure 3-2b).

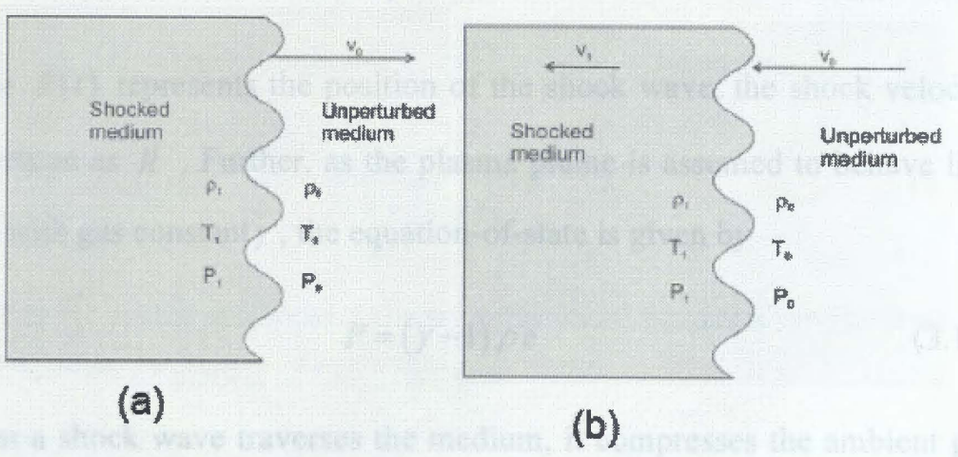

Figure 3-2 (a) Shock front as viewed from the frame of reference of unperturbed medium. (b) shocked medium and unperturbed medium as viewed from the frame of reference of the shock front

It is important to note that in the reference frame of the unperturbed medium, v_0 is the speed of the propagating shock and $v_0 - v_1$ is the speed with which the shocked fluid is seen to move forward. In the reference frame of the shock wave, the laws of conservation of mass, momentum, and energy, when

applied to the medium on the either side of the side of the shock front, results in the following equations.

$$\begin{aligned} \rho_0 v_0 &= \rho_1 v_1 \\ P_0 + \rho_0 v_0^2 &= P_1 + \rho_1 v_1^2 \\ \frac{\gamma}{\gamma-1}\frac{P_0}{\rho_0} + \frac{1}{2}v_0^2 &= \frac{\gamma}{\gamma-1}\frac{P_1}{\rho_1} + \frac{1}{2}v_1^2 \end{aligned} \tag{3.11}$$

The above conservation relationships are known as shock jump condition or Rankine-Hugoniot relation [13]. The energy of the plume (E) is assumed to be large. Hence, the temperature and pressure of the plume are very high. In such a condition the ambient pressure is very small in comparison to plume pressure and hence it can be neglected. Simplifying the above relations and using $P_0 = 0$, the expressions for ρ_1, v_1 and P_1 are as follows

$$\begin{aligned} \rho_1 &= \frac{\gamma+1}{\gamma-1}\rho_0, \\ v_1 &= \frac{2}{\gamma+1}\dot{R}, \\ P_1 &= \frac{2}{\gamma+1}\rho_0 \dot{R}^2, \end{aligned} \tag{3.12}$$

Since $R(t)$ represents the position of the shock wave, the shock velocity v_0 is also written as $\dot{R}$. Further, as the plasma plume is assumed to behave like an ideal gas with gas constant γ, the equation-of-state is given by

$$P = (\gamma-1)\rho e \tag{3.13}$$

When a shock wave traverses the medium, it compresses the ambient gas at its periphery into a thin shell. Such a compression is prominent for gases with $\gamma = 1$. The integral (3.10) now needs to be evaluated over a thin shell of shocked medium in conjunction with Rankine-Hugoniot relations (3.12) and the equation-of-state (3.13). The thickness of the shell can be estimated using the conservation of mass.

Mass of shell = Mass swept up by shock,

(3.14)

$$\Rightarrow C_N \int_{R-\Delta R}^{R} \rho_1 r^N \, dr = C_N \int_0^R \rho_0 r^N \, dr$$

Here R is the position of the shock front and ΔR is the thickness of the shock front. Evaluating the above integral and using relation (3.12) to eliminate ρ_1, the relation (3.14) finally simplifies to

$$\Delta r = \frac{\gamma - 1}{(N+1)(\gamma+1)} R \tag{3.15}$$

As the thickness, ΔR of the mass shell is small; the values of v_1 and P_1 can be conveniently assumed to be constant across the mass shell and equal to that at the shock front. The integral (3.10) can now be simply written as the product of the energy per unit volume and the volume of the mass shell.

$$E_0 = \rho_1 \left[\frac{1}{2} v_1^2 + \frac{P_1}{(\gamma-1)\rho_1} \right] \left[C_N R^N \Delta r \right] \tag{3.16}$$

Now, using the Rankine-Hugoniot relations i.e. Eq. (3.12), to eliminate ρ_1, v_1 and P_1 and Eq. (3.15) to eliminate ΔR, Eq. (3.16) now becomes

$$\frac{E_0}{\rho_0} = \frac{C_N}{N+1} \frac{4}{(\gamma+1)^2} R^{N+1} \dot{R}^2 \tag{3.17}$$

Solving the above nonlinear ordinary differential equation for the position of the shock front as a function of time, one gets

$$R(t) = \left[\frac{(N+3)(\gamma+1)}{4} \right]^{\frac{2}{(N+3)}} \left[\frac{N+1}{C_N} \right]^{\frac{1}{(N+3)}} \left[\frac{E_0}{\rho_0} \right]^{\frac{1}{(N+3)}} t^{\frac{2}{(N+3)}} \tag{3.18}$$

As discussed earlier the plasma expansion is isotropic in nature. Hence the shock front is approximately hemispherical and N assumes value 2. The relation (3.18) then reduces to

$$R(t) = \xi \left[\frac{E_0}{\rho_0}\right]^{\frac{1}{5}} t^{\frac{2}{5}} \tag{3.19}$$

Here ξ is a dimensionless constant.

3.3.2 Drag model

As discussed earlier, one of the prime assumptions for the formation of the blast wave is that the mass of the ablated fragments be small as compared to the mass of the gas compressed by the shock wave. This ensures a free propagation of the shock wave diverging from the point explosion. If the mass of the shocked gas is negligible in comparison to the mass of the ablated matter, the matter is least affected by the background gas and it expands linearly with time. The expansion in such a case is similar to the expansion of the plume in vacuum. For the formation of shock wave it is essential that the thickness of the compressed gas layer be significantly larger than the mean free path of the molecules in the undisturbed gas [14, 15]. Thus, it is expected that as the background density of the gas decreases, the shock wave will be formed at larger distances away from the target with a considerable reduction in its strength. At pressures lower than 1mbar the elastic scattering of the plume species by the background gas atoms causes the slowing of the plasma plume front. This type of slowing is accounted for by the drag model proposed by Geohegan to predict the expansion of the plume front in its early stage of evolution [16]. According to this model the plasma plume is regarded as an ensemble which experiences a viscous force proportional to its velocity through the background gas. The equation of motion is then written as

$$a = -\beta v \quad \Rightarrow \quad \frac{d^2R}{dt^2} = -\beta \frac{dR}{dt} \tag{3.20}$$

where a and v are acceleration and velocity of the plume, β is the slowing coefficient and R is the position of the plume front. The solution of the above differential equation turns out to be

$$R = R_f \left[1 - e^{-\beta t}\right] \tag{3.21}$$

Here R_f is the distance at which the plume stops. It is important to notice that this model is valid only during the initial stage of expansion when the mass of the plume far exceeds the mass of the compressed background gas at the periphery of the plume.

In this thesis, the models discussed thus far have been extensively used to predict the motion of the shock front produced due to the plasma plume. The dependence of the shock front velocity on the atomic mass of the target and the validity regime of these models also forms one of the topics of present research.

References

1. Kelly R., Miotello A., Braren B., Gupta A., and Casey K., (1992). "Primary and secondary mechanisms in laser-pulse sputtering". *Nuclear Instruments and Methods in Physics Research Section B: Beam Interactions with Materials and Atoms*, **65**(1-4): pp. 187-199.

2. Pai S. I., *Introduction to the theory of compressible flow*. 1970: Affiliated East-West press.

3. Harilal S. S., Bindhu C. V., Tillack M. S., Najmabadi F., and Gaeris A. C., (2003). "Internal structure and expansion dynamics of laser ablation plumes into ambient gases". *Journal of Applied Physics*, **93**(5): pp. 2380-2388.

4. Geohegan D. B. and Puretzky A. A., (1995). "Dynamics of laser ablation plume penetration through low pressure background gases". *Applied Physics Letters*, **67**(2): pp. 197-199.

5. Harilal S. S., (2001). "Expansion dynamics of laser ablated carbon plasma plume in helium ambient". *Applied Surface Science*, **172**(1-2): pp. 103-109.

6. Ventzek P. L. G., Gilgenbach R. M., Ching C. H., and Lindley R. A., (1992). "Schlieren and dye laser resonance absorption photographic investigations of KrF excimer laser-ablated atoms and molecules from polyimide, polyethyleneterephthalate, and aluminum". *Journal of Applied Physics*, **72**(5): pp. 1696-1706.

7. Gupta A., (1993). "Gas-phase oxidation chemistry during pulsed laser deposition of $YBa_2Cu_3O_{7-}$ films". *Journal of Applied Physics*, **73**(11): pp. 7877-7886.

8. Westwood W. D., (1978). "Calculation of deposition rates in diode sputtering systems". *Journal of Vacuum Science and Technology*, **15**(1): pp. 1-9.

9. Amoruso S., Bruzzese R., Spinelli N., Velotta R., Vitiello M., and Wang X., (2003). "Dynamics of laser-ablated MgB_2 plasma expanding in argon probed by optical emission spectroscopy". *Physical Review B –Condensed Matter and Materials Physics*, **67**(22): pp. 224503.

10. Chen X. Y., Xiong S. B., Sha Z. S., and Liu Z. G., (1997). "The interaction of ambient background gas with a plume formed in pulsed laser deposition". *Applied Surface Science*, **115**(3): pp. 279-284.

11. Angleraud B., Aubreton J., and Catherinot A., (1998). "Expansion of the ablation plume created by ultraviolet laser irradiation of various target materials". *The European Physical Journal - Applied Physics*, **5**: pp. 303-310.

12. Hutchens G. J., (2000). "Approximate near-field blast theory: A generalized approach". *Journal of Applied Physics*, **88**(6): pp. 3654-3658.

13. Sachs R. G., (1946). "Some Properties of Very Intense Shock Waves". *Physical Review*, **69**(9-10): pp. 514 - 522.

14. Chen X. Y., Wu Z. C., Yang B., Lei X. Y., and Liu Z. G., (2000). "Four regions of the propagation of the plume formed in pulsed laser deposition by optical-wavelength-sensitive CCD photography". *Thin Solid Films*, **375**(1-2): pp. 233-237.

15. Gupta A., Braren B., Casey K. G., Hussey B. W., and Kelly R., (1991). "Direct imaging of the fragments produced during excimer laser ablation of $YBa_2Cu_3O_{7-}$.". *Applied Physics Letters*, **59**(11): pp. 1302-1304.

16. Geohegan D. B., (1992). "Fast intensified-CCD photography of $YBa_2Cu_3O_{7-x}$ laser ablation in vacuum and ambient oxygen". *Applied Physics Letters*, **60**(22): pp. 2732-2734.

Chapter 4

Analysis of the optical time-of-flight profiles

4.1 Introduction

The present chapter discusses the analysis of the temporal profiles. The determination of velocity from the temporal profiles is of main concern here. In this context, the validity of interpretation of temporal profile as time-of-flight spectrum and transformation of temporal profiles to velocity domain has been dealt with in greater detail. Besides this, from the view point of isolating different velocity components from the temporal profile, the analytic form of the shifted-Maxwell-Boltzmann distribution in time domain has been derived for both particle flux and particle density detector.

This chapter consists of five sections. Section 2 of this chapter explains the rationale behind accepting temporal profiles as the velocity distribution of the plasma species in the time domain. The section 3 discusses two different ways of attaining velocity distributions of the plasma species from the temporal profiles. The numerical transformation of temporal profiles as discussed in this chapter will be frequently used in chapter 6. The expression for shifted-Maxwell-Boltzmann distribution in time domain for both flux sensitive and density detectors have been discussed in section 4. The chapter finally ends with a section describing the method to determine the kinetic energy of the different velocity components of plasma plume.

4.2 Velocity determination using temporal profiles

The time resolved measurements of the plasma emission are often employed to study the TOF and the local population of a particular plasma species. The essence of this technique, widely known as optical time-of-flight spectroscopy, lies in the collisional re-excitation of the species in the plume. The collisional processes which populate the short-lived emissive state include three-body recombination of ions with electrons, electron-impact excitation of ground

and low-lying states of neutrals and ions, and collisional or radiative deactivation of Rydberg states [1]. These mechanisms have already been discussed in the chapter 1. The proposition, attributing the plasma emission to collisional re-excitation of atoms, stands well justified in the view that the time for which the plasma emissions are observed (typically more than 1μs) far exceed the lifetimes of the various species investigated (typically around tens of nanoseconds). This means that if the number density of the plasma species is higher, the probability of collision is higher and consequently the emission intensity observed is also higher. In other words, the peak intensity corresponds to the highest number density of particles in the plume. With this interpretation of the temporal profiles, they can be envisaged as the particle density distribution in time for a fixed location in plasma plume.

The time-of-flight spectroscopy is frequently used to study the gas dynamics of the shock front formed during the explosive expansion of the plume in the background gas. In such studies the intensity maximum of temporal profile corresponds to arrival of the shock front. In order to gain insight into correctness of this procedure, let us write an approximate expression for the intensity of the plasma emission. Consider the plasma species in an excited state corresponding to energy E_u. Assuming the temperature of the plasma to be $T(d)$ and that the number of atoms in excited state is given by Boltzmann distribution, the intensity of the plume at distance d from the target is then given by [2, 3]

$$I(d) \propto \rho(d) e^{\frac{-E_u}{k_B T(d)}} \tag{4.1}$$

Since the plasma density increases as one move from the plasma centre towards the shock front (while the temperature shows a decreasing trend), equation (4.1) predicts a difference in the location of the intensity maximum of the temporal profile and the shock front. To estimate this difference, consider an ideal blast wave model. The density and temperature varies with the distance according to the relations [4]

$$\frac{\rho(d)}{\rho(R)} = \left(\frac{d}{R}\right)^{\left(\frac{3}{\gamma-1}\right)} \tag{4.2}$$

$$\frac{T(d)}{T(R)} = \left(\frac{d}{R}\right)^{\left(\frac{-3}{\gamma-1}\right)} \tag{4.3}$$

Here R represents the location of the plasma front. The relations (4.3) and (4.2) in conjunction with relation (4.1) yields

$$I(z) = K\,\rho(R)\,z^{\frac{3}{\gamma-1}}\,e^{\left(\frac{-E_u}{k_B T} z^{\frac{3}{\gamma-1}}\right)} \tag{4.4}$$

Here $z = d/R$. The value of z at which the intensity maximum occurs is then given by

$$z = \left(\frac{k_B T}{E_u}\right)^{\frac{\gamma-1}{3}} \Rightarrow \frac{d_{\max}}{R} = \left(\frac{k_B T}{E_u}\right)^{\frac{\gamma-1}{3}} \tag{4.5}$$

The relative difference in the locations of the intensity maximum and the shock front is thus given as

$$\frac{R - d_{\max}}{R} = 1 - \left(\frac{k_B T}{E_u}\right)^{\frac{\gamma-1}{3}} \tag{4.6}$$

In order to illustrate the order of difference between the shock front and the intensity maximum of plasma emission, consider aluminum plasma. For neutral excited species corresponding to 396.15 nm transition, Eu ≈ 3.14 eV. At modest plasma temperature of 1 eV the relative difference in the location of the shock front and the intensity maximum as predicted by relation (4.6) turns out to be around 0.08. In other words, if one considers a plasma plume expanded to about 3 mm, the difference between the intensity maxima and the actual shock front is only about 0.2 mm.

The above calculations have shown that the difference between the spatial location of the shock front and the intensity maximum of the plume emission is

considerably low and that the intensity maximum can be reliably used to locate the shock front. In other words the temporal location of intensity maximum of the plume emission can be used to study the plume evolution in presence of ambient pressures.

4.3 Transformation of temporal profiles to velocity domain

As discussed in earlier section the fluorescence time of various excited species are very small and do not affect the TOF profiles in any way. This observation hints collisions of the high-energy atoms, ions, and electrons within plasma, as the most possible source of emission besides MPI, PHR, and IB. Hence the TOF profiles indeed reflect the temporal variation in the particle density of the observational volume of the plasma plume. However, a word of caution needs to be considered in construing temporal profiles. The luminescence intensity does not necessarily correspond to the overall plume density. In fact, the visible emission from excited states in the plume comprises just one observable component of the plume transport. Hence the wavelength selected temporal profiles reflect the dynamics of a particular species and not of the whole plume.

In order to elucidate the procedure of plasma front velocity determination using the temporal profile, consider the Al plasma plume profile recorded at a distance 10mm away from the target (cf. Figure 4-1).

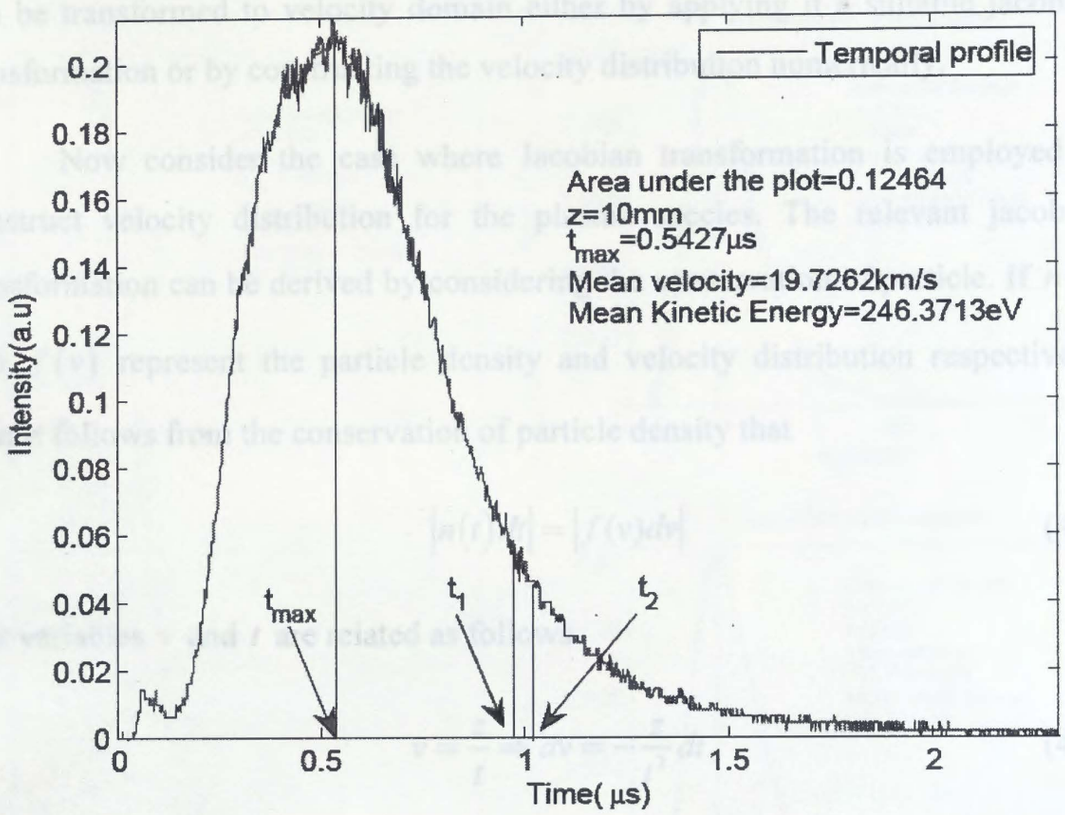

Figure 4-1 A typical temporal profile recorded at distance 10mm away from the target. The shaded area is proportional to the number of the particles that have crossed the field of view during time t to $t+dt$. t_{max} is the time when maximum particles have crossed the field of view.

The area contained within two lines at t_1 and t_2 in the figure is proportional to the number of particles that have taken time t to $t+dt$ to cross the predetermined distance of 10mm. In other words the shaded area represents the number of particles having velocities ranging from v to $v+dv$. Here $v=\frac{z}{t}$ and $dv=z\left(\frac{1}{t_1}-\frac{1}{t_2}\right)$. It is apparent from this interpretation of temporal profiles that the maximum number of particle crosses the field of view at the time, t_{max}, corresponding to the peak of the profile. Hence the most probable velocity of the probed species is given by

$$v_{mp}=\frac{z}{t_{\max}} \tag{4.7}$$

The above discussion clearly indicates that temporal profiles are the velocity distribution of the plasma species in time domain. Any temporal profile

can be transformed to velocity domain either by applying it a suitable jacobian transformation or by constructing the velocity distribution numerically.

Now consider the case where Jacobian transformation is employed to construct velocity distribution for the plasma species. The relevant jacobian transformation can be derived by considering the conservation of particle. If $n(t)$ and $f(v)$ represent the particle density and velocity distribution respectively, then it follows from the conservation of particle density that

$$|n(t)dt| = |f(v)dv| \tag{4.8}$$

The variables v and t are related as follows

$$v = \frac{z}{t} \Rightarrow dv = -\frac{z}{t^2}dt \tag{4.9}$$

Using relations (4.8) and (4.9), the velocity distribution is then expressed as

$$f(v) = \frac{t^2}{z}n(t) \tag{4.10}$$

Here z is the distance between the target surface and the field of view measured in direction normal to the target.

In the latter method (numerical transformation) the time interval over which the temporal profile is recorded is first divided into equal parts. The temporal profile is then integrated over each part. The value of this integral represents the number of particle having velocities appropriate to the time interval considered. The conservation of the particle number was taken care of by normalising the integrated area over a particular time interval by corresponding velocity spread. One advantage of numerically transformation of the temporal profile is that the noise gets averaged out and is reduced considerably. For the given velocity transformation to be valid, the mean velocity evaluated from the resulting velocity distribution and the area under the velocity distribution must be equal to those obtained from the original temporal profile. The correctness of the procedure employed to implement the transformation is evident from Figure 4-2.

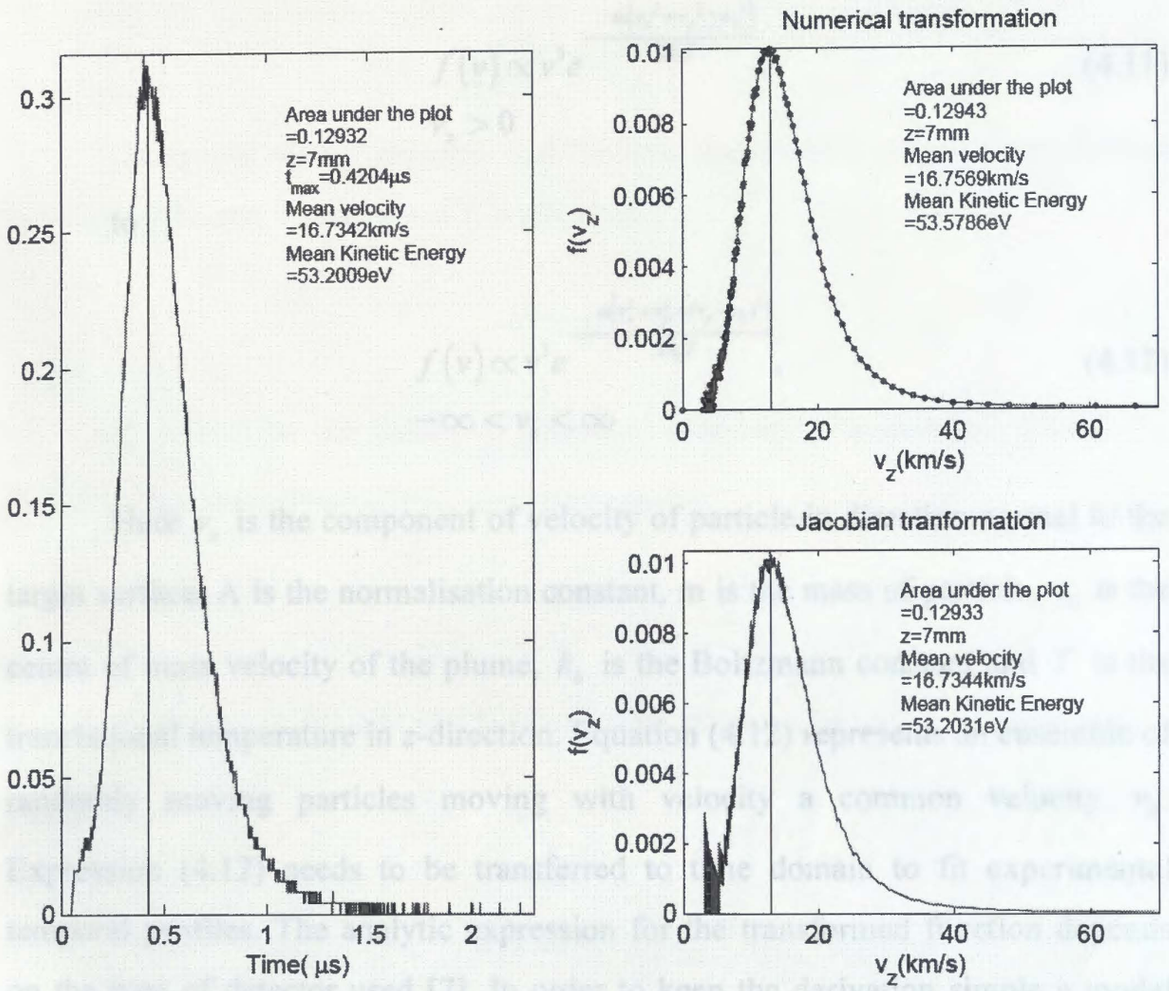

Figure 4-2 Transformation of temporal profile to velocity domain by jacobian tansformation and numerically. Notice that there is considerable reduction in noise if transformation is made numerically.

4.4 Modelling temporal profiles

An extensive study of pulsed laser ablation has shown that the velocity distribution function of the ablated particles is governed by the laser fluence. For the case of low laser fluence the particle number density of the plasma plume is very low. Hence, the inter-particle collisions are negligible and the velocities normal to the surface assume only positive values. The velocity distribution of particles in such a case thus takes the form of a "half-range" Maxwellian. However, when the laser fluence is high the particle density of the plume is high and the collisions among the particles cause the velocity distribution function to change from half-range Maxwellian to a full-range Maxwellian [5, 6]. In other words, the velocity distribution function for the normal component of the velocity changes from

$$f(v) \propto v^3 e^{-\frac{m\left(v_x^2+v_y^2+v_z^2\right)}{2k_bT}}, \quad v_z > 0 \tag{4.11}$$

to

$$f(v) \propto v^3 e^{-\frac{m\left[v_x^2+v_y^2+(v_z-v_0)^2\right]}{2k_bT}}, \quad -\infty < v_z < \infty \tag{4.12}$$

Here v_z is the component of velocity of particle in direction normal to the target surface, A is the normalisation constant, m is the mass of particle, v_0 is the centre of mass velocity of the plume, k_b is the Boltzmann constant and T is the translational temperature in z-direction. Equation (4.12) represents an ensemble of randomly moving particles moving with velocity a common velocity v_0. Expression (4.12) needs to be transferred to time domain to fit experimental temporal profiles. The analytic expression for the transformed function depends on the type of detector used [7]. In order to keep the derivation simple a model proposed by Utterback [8] has been adopted. A brief overview of this model of plasma expansion follows next. This model assumes that the laser energy deposited on the target causes vaporization from small region of the target. The resulting bubble of ablated material then expands against the substrate and imparts momentum to it. As a result the plasma bubble as a whole acquires a centre-of-mass (COM) velocity v_{cm} in laboratory frame. Owing to the symmetry of plasma expansion, v_{cm} is normal to the target surface. When the COM of the ablated bubble has moved a sufficient distance the density of particles in the bubble is still high enough so that most of the particles equilibrate at temperature T relative to the COM. The angular distribution of the particle as observed by the laboratory observer happens to be skewed owing to the COM velocity superimposed on the purely thermal velocity distribution. With these assumptions, the number density of the particle in the expanding plasma will be calculated. Let the prime denote the physical quantities in the COM frame. In COM frame the velocity distribution (4.12) is thus written as

$$f(v) = Av^3 e^{\frac{-mv^2}{2kT}} \tag{4.13}$$

Using the above velocity distribution, the number of particles having velocities between v and $v+dv$ is given by

$$dN = \left| f(v)dv \right| \tag{4.14}$$

If $n(r,t)$ be the density of plasma at time t and at a distance r in COM frame, the number of particles is then expressed as

$$dN = 4\pi r^2 n(r,t)dr \tag{4.15}$$

Equations (4.14) and (4.15), along with the transformation relation $v = \frac{r}{t}$ yields

$$n(r,t) = A\frac{r}{t^4} e^{\frac{-mv^2}{2k_b T}} \tag{4.16}$$

The optical time-of-flight spectroscopy essentially involves the measurement of optical intensity along the axis normal to the target surface. Hence the expression (4.16) needs to be expressed in one-dimensional form. With this consideration, the equation (4.16) when transformed to the laboratory reduces to

$$n(z,t) = A\frac{z}{t^4} e^{\frac{-m}{2k_b T}\left(\frac{z}{t} - v_0\right)^2} \tag{4.17}$$

As discussed earlier, the optical time-of-flight spectroscopy depends on the density of the plasma species. Hence the signal recorded can be expressed as

$$I(z,t) \sim n(z,t)$$

$$\Rightarrow I(z,t) = A\frac{z}{t^4} e^{\frac{-m}{2k_b T}\left(\frac{z}{t} - v_0\right)^2} \tag{4.18}$$

Where $I(z,t)$ corresponds to the optical intensity recorded at time t and at a distance z away from the target. For the flux sensitive detectors like faraday cup, the signal recorded is proportional to the incident flux [9]. The signal is thus represented as

$$\begin{aligned} & L(z,t) \sim n(z,t) v_z \\ & \Rightarrow L(z,t) = A \frac{z}{t^4} e^{\frac{-m}{2k_bT}\left(\frac{z}{t}-v_0\right)^2} v_z = A \frac{z}{t^4} e^{\frac{-m}{2k_bT}\left(\frac{z}{t}-v_0\right)^2} \frac{z}{t} \\ & = A \frac{z^2}{t^5} e^{\frac{-m}{2k_bT}\left(\frac{z}{t}-v_0\right)^2} \end{aligned} \tag{4.19}$$

Here $L(z,t)$ is the signal recorded by the flux sensitive detector. The optical time of flight profile essentially reflects the variation in the plume density. Hence equation (4.18) will be used to fit these temporal profiles. Figure 4-3 depicts a temporal profile recorded at a distance 5 mm away from the target. It is evident from the figure that the temporal profile constitutes more than one population of species each with a distinct velocity distribution.

4.5 Kinetic energy of plasma species

The kinetic energy of the plasma species was estimated using the temporal profile. The temporal profile recorded at various pressures and for different distances persistently showed the presence of two peaks *viz.* fast and slow peak. The time evolution of the slow moving plasma core was isolated by fitting shifted Maxwell-Boltzmann functions (SMB) to the observed temporal profile. The fast peak was well fitted by a single SMB while the slow consisted of about three SMB. Figure 4-3 shows a typical temporal profile fitted by four SMB's. As illustrated in the figure, the first SMB mimics the evolution of the rapidly evolving plasma envelope while the other three SMB's together describe the evolution of the plasma core.

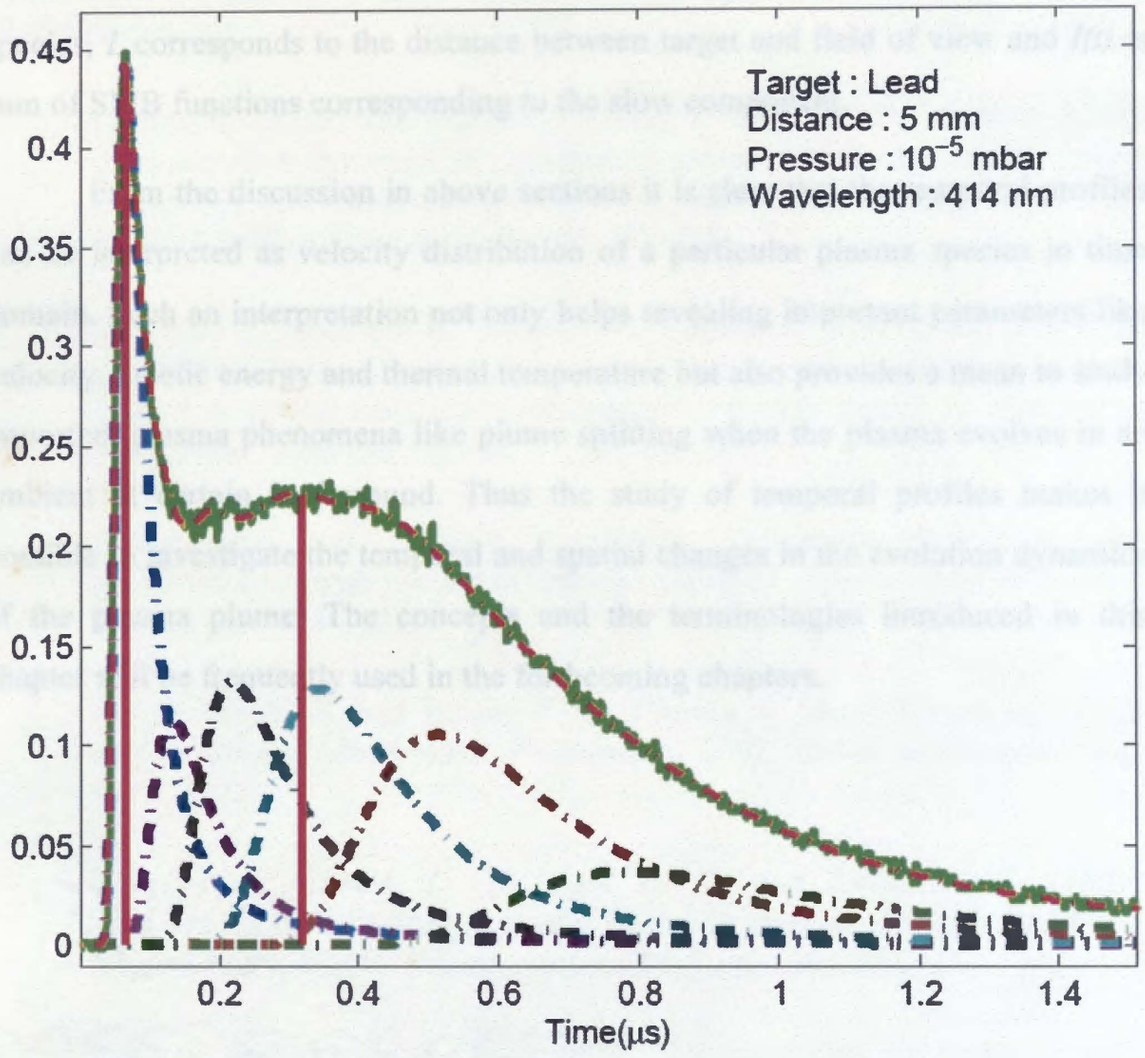

Figure 4-3 A temporal profile corresponding to Lead plasma is fitted by multi-SMB model. The presence of more than one distribution function may indicate that the plasma is not equilibrated at a distance 5mm away from the target surface.

The temporal evolution as described by the sum of these three SMB was then used to calculate the kinetic energy of the plasma species constituting the core of the plume. The mean kinetic energy of the species is given by [10]

$$\langle E_{kin} \rangle = \frac{1}{2} \frac{\int_0^\infty m[u(t)]^2 I(t)dt}{\int_0^\infty I(t)dt} = \frac{mL^2}{2} \frac{\int_0^\infty t^{-2} I(t)dt}{\int_0^\infty I(t)dt} \qquad (4.20)$$

where m is the mass of the plasma species investigated, u is the velocity of the species, L corresponds to the distance between target and field of view and $I(t)$ is sum of SMB functions corresponding to the slow component.

From the discussion in above sections it is clear that the temporal profiles can be interpreted as velocity distribution of a particular plasma species in time domain. Such an interpretation not only helps revealing important parameters like velocity, kinetic energy and thermal temperature but also provides a mean to study important plasma phenomena like plume splitting when the plasma evolves in an ambient at certain background. Thus the study of temporal profiles makes it possible to investigate the temporal and spatial changes in the evolution dynamics of the plasma plume. The concepts and the terminologies introduced in this chapter will be frequently used in the forthcoming chapters.

References

1. Geohegan D. B. and Puretzky A. A., (1996). "Laser ablation plume thermalization dynamics in background gases: combined imaging, optical absorption and emission spectroscopy, and ion probe measurements". *Applied Surface Science*, **96-98**: pp. 131-138.

2. Amoruso S., Bruzzese R., Spinelli N., Velotta R., Vitiello M., and Wang X., (2003). "Dynamics of laser-ablated MgB_2 plasma expanding in argon probed by optical emission spectroscopy". *Physical Review B –Condensed Matter and Materials Physics*, **67**(22): pp. 224503.

3. Sharma A. K. and Thareja R. K., (2007). "Anisotropic emission in laser-produced aluminum plasma in ambient nitrogen". *Applied Surface Science*, **253**(6): pp. 3113-3121.

4. Zel'dovich Y. B. and Raizer Y. P., *Physics of Shock Waves and High-Temperature Hydrodynamic Phenomena*. 2002: Dover publications, Inc., 944.

5. Zheng J. P., Huang Z. Q., Shaw D. T., and Kwok H. S., (1989). "Generation of high-energy atomic beams in laser-superconducting target interactions". *Applied Physics Letters*, **54**(3): pp. 280-282.

6. Kelly R. and Dreyfus R. W., (1988). "Reconsidering the mechanisms of laser sputtering with Knudsen-layer formation taken into account". *Nuclear Instruments and Methods in Physics Research Section B: Beam Interactions with Materials and Atoms*, **32**(1-4): pp. 341-348.

7. Miotello A. and Kelly R., (1999). "On the origin of the different velocity peaks of particles sputtered from surfaces by laser pulses or charged-particle beams". *Applied Surface Science*, **138-139**: pp. 44-51.

8. Utterback N. G., Tang S. P., and Friichtenicht J. F., (1976). "Atomic and ionic beam source utilizing pulsed laser blow off". *Physics of Fluids*, **19**(6): pp. 900-905.

9. Kelly R. and Dreyfus R. W., (1988). "On the effect of Knudsen-layer formation on studies of vaporization, sputtering, and desorption". *Surface Science*, **198**(1-2): pp. 263-276.

10. Torrisi L., Gammino S., Andò L., Nassisi V., Doria D., and Pedone A., (2003). "Comparison of nanosecond laser ablation at 1064 and 308 nm wavelength". *Applied Surface Science*, **210**(3-4): pp. 262-273.

Chapter 5
Instrumentation

5.1 Introduction

The details of experimental set-up used for time-resolved spectroscopy of the plumes in the pulsed laser ablation (PLA) are described in this chapter. Using time-resolved measurements, plume profiles were recorded at a pre-determined distance from the target. This was achieved by the standard method, where the line emissions originating from the spatially-resolved regions of the plume were recorded as a function of time. Provisions were made to vary this distance, *viz.* the distance between the target (from where plume originates) and the space-resolved region in the plasma (along its direction of expansion) from where emission signals were recorded. Both in laser ablation of solids as well in thin film ablation, similar method were employed. The different components of the experiment and details of data acquisition are described below. For the sake of bringing out the major differences in these two experiments *viz.* bulk ablation and thin film ablation, they are described in separate sub-sections.

5.2 Instrumentation

5.2.1 For laser ablation from solids

Laser ablation of metals Al, Cu, Pb and Sb were carried out in a specially designed LPP spectrometer which was made from a 25.6 cm ID, 36 cm long stainless steel shell, provided with two ISO250K flanges as the end flanges. At 11 cm away from far-side end-flange, three radial vacuum ports (two ISO100K and one ISO160K) were provided for mounting vacuum pumps and other auxiliary units. Further 16.5 cm away from this plane, six radial ISO63K ports were provided for observation of the plume using various diagnostic tools. The target was arranged in the neighbourhood of this plane, so that the emission was observed in an orthogonal direction to the evolving plasma. The near-side end-flange was provided with an axial ISO63K, which served as the window for the

laser beam. Another inclined ISO63K (30^0 with respect to the axis) was provided on this end-flange which either could be used as an inclined laser beam window or simply as a view-port. The chamber was pumped down to a base pressure of 5×10^{-6} mbar using a turbo pump (Pfeiffer TMH261). The sketch of the apparatus is shown in Figure 5-1.

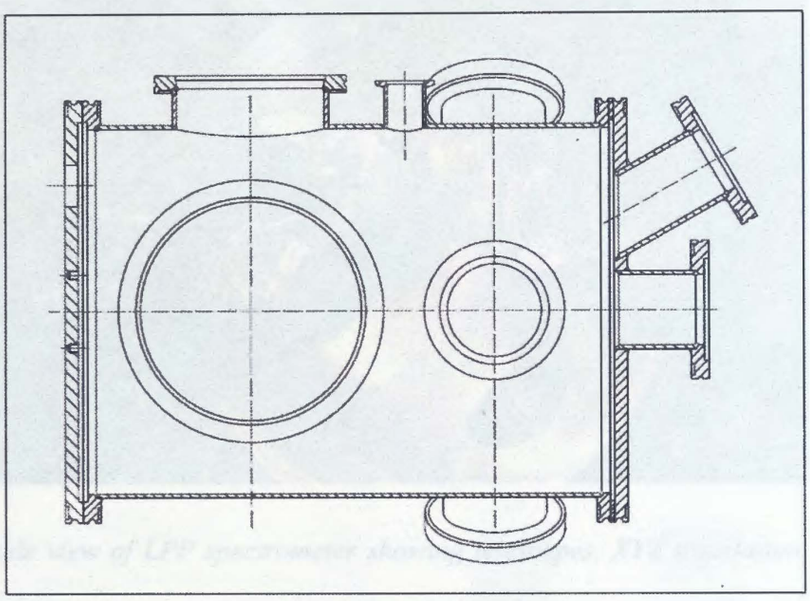

Figure 5-1 The design of the LPP spectrometer showing details of 6 in-plane ports for the diagnostics of LPP plume and the end-flange with laser window.

Figure 5-2 shows the details of components inside the LPP spectrometer. UV laser pulses from a XeCl excimer laser (Lambda Physik LPX105E) were led to the target placed inside the LPP spectrometer. The excimer laser beam profile was rectangular, with $l\times b$ ~7×26 mm. A 2" diameter MgF_2 spherical lens having 30 cm focal length was used to focus the laser radiation to ~50×250 μm focal spot. The energy of the laser beam could be varied from 30 to 150 mJ per pulse and correspondingly, the laser fluence at the target could be varied from 2.4 to 12 J/cm^2. These laser fluences were found to be sufficient to cause ablation and plasma ignition for all metal targets used in the study.

Freshly prepared metal targets having 50×50 mm dimension were mounted on a XYZ translation stage, mounted inside the LPP chamber (see Figure 5-2). The travel of each stage was 50 mm. The travel of Z-stage was set along the incident laser direction. The X and Y travel were programmed such that each laser spot fell on a fresh (previously not exposed to laser) target surface. This was

achieved by incrementing X by 0.5 mm after every laser shot, and reversing the X-direction after a suitable Y-increment at both end-points of X. Such a surface scan is known as 'raster scan'.

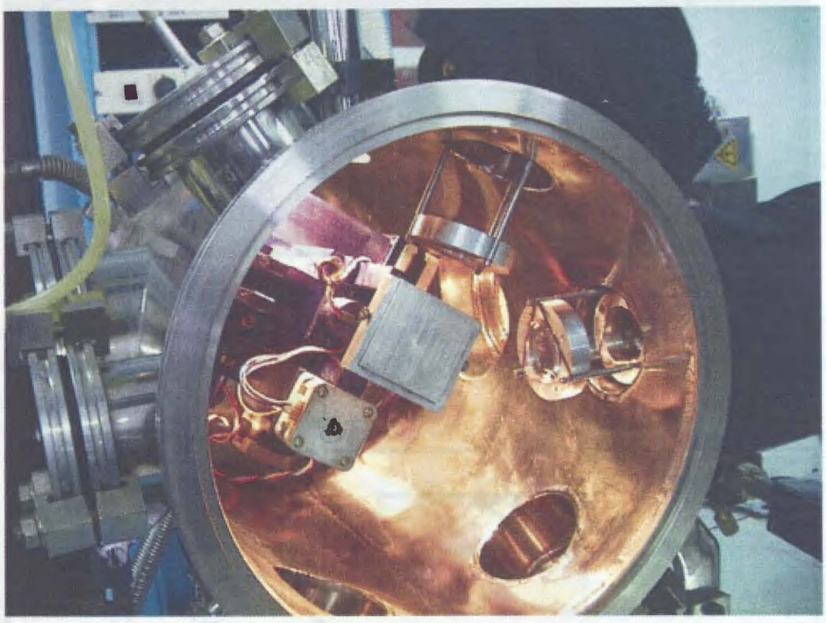

Figure 5-2 The inside view of LPP spectrometer showing telescopes, XYZ translation stage and the target mount.

One of the ISOK63 port holds a specially designed optics for spatially resolving the plasma plume. This assembly consisted of two plano-convex fused silica lenses and it imaged the plume on to an iris held at the ISO63K flange. The magnification of this optics was slightly less than unity. Ray-tracing software (***Beam-3***, *Stellar Software*) was used to design the telescopes used in the experiment. A 250 μm aperture at the centre of the iris transmitted the light gathered from an equivalent region in the evolving plasma. The role of iris in improving the spatial resolution is demonstrated in the ray tracing diagram (Figure 5-3). By this arrangement, an over all spatial resolution of ~ 300 μm was achieved in this experiment and light transmitted through the aperture was gathered by a glass fiber bundle and was fed to a 0.5 meter monochromator with an f/no. matching optics at its entrance side.

The block diagram of the experimental set up is presented in Figure 5-4. Various components and their functions are described below.

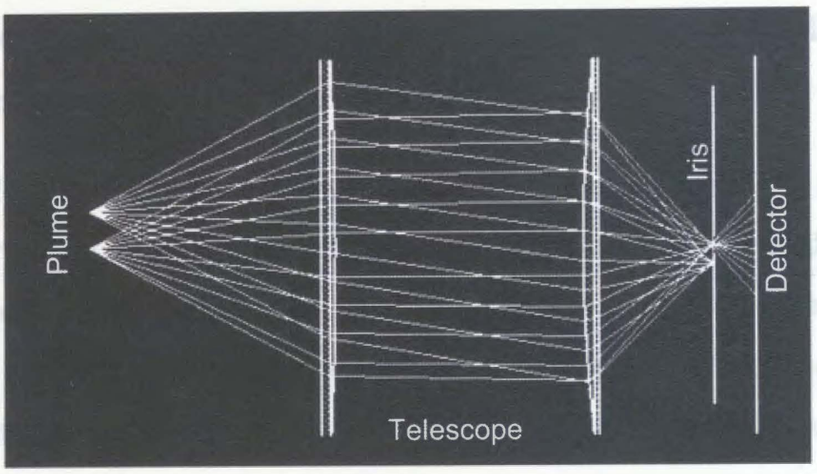

Figure 5-3 The ray diagram of the telescope designed for spatial resolution of plasma. The spatial resolution was determined by the magnification factor of the optics and size of the aperture used. The spatial resolution in the experiment was ~300 μm.

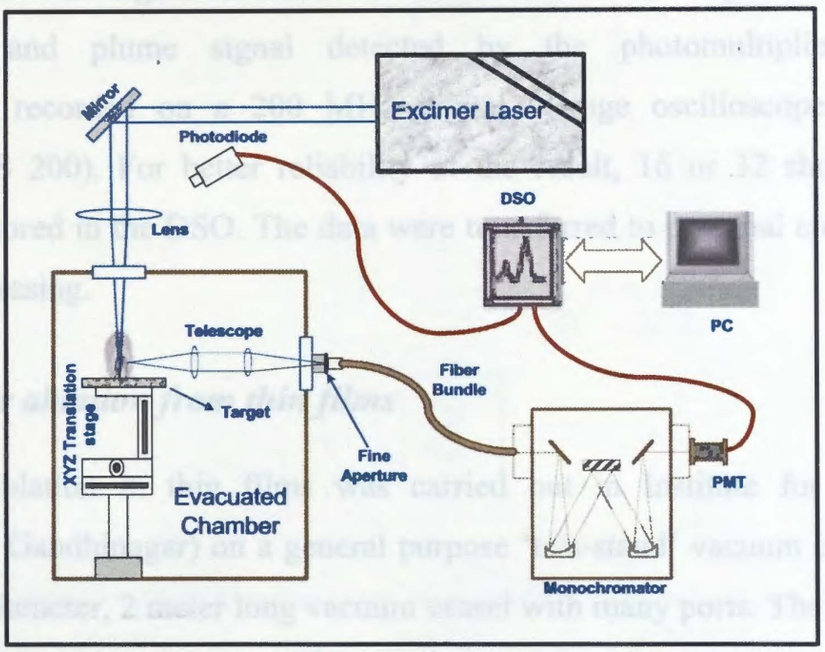

Figure 5-4 The schematic of experimental setup used to study plume evolution due to laser ablation in solids.

A 0.5 m monochromator (λ-Minuteman) was used to choose various emission lines in the plasma. The resolution of the monochromator was ~ 0.2 nm for 40 μm slit width. However, in this experiment, since monochromator was used as a filter for widely spaced emission lines, resolution was not important. For gaining light gathering, slits were kept widely open (1 mm). [Normally, monochromators are avoided in high-precision time resolved measurements due to time spreads caused by path differences inside the monochromator. However, in

the present experiment, those time spreads (~ 10^{-9} – 10^{-10} sec) were negligible as compared to the time scales in the experiment (~ 10^{-8} – 10^{-6} sec).]

An EMI 9882 photomultiplier was used as the light detector. The rise-time of this detector was 1.8 ns and was suitable for the time-resolved studies. The detector was mostly recording photon piled-up signals (where, individual photon signals can not be resolved) and was configured in low-output impedance current mode. A few capacitors were provided at the last stages of the bleeding circuit as boosters for piled-up pulses.

A small portion of light signal reflected from windows, were detected by a fast photo diode. This signal served as the time-marker in the experiment. Both time marker and plume signal detected by the photomultiplier were simultaneously recorded on a 200 MHz digital storage oscilloscope (DSO) (Tektronix TDS 200). For better reliability of the result, 16 or 32 shots were averaged and stored in the DSO. The data were transferred to personal computers for offline processing.

5.2.2 For laser ablation from thin films

Laser ablation in thin films was carried out in Institute for Plasma Research (IPR, Gandhinagar) on a general purpose 'test-stand' vacuum chamber. This was a 1' diameter, 2 meter long vacuum vessel with many ports. The vacuum chamber was pumped down to 2×10^{-6} mbar pressure using an oil diffusion pump. On this apparatus, it was not convenient to mount the light collecting optics inside the vacuum chamber. It was possible to change the target position (only along the radial direction) by manipulating the target holder from outside. Due to these limitations, it was not possible to average signals over many laser shots, and therefore all observations were made in 'single-shot' mode.

The sketch of the experimental scheme used is shown in Figure 5-5. Commercially procured LiF-C multilayer films were used as the target. The target was composed of uniform layers of 0.5 μm thick carbon film and 0.05 μm of LiF film on a 1.2 mm thick quartz substrate. The LiF film was sandwiched between

the substrate and the carbon film. As LiF is transparent to the incident laser light, practically no material would ablate when it is irradiated with a laser. The carbon layer was used to couple the laser energy to the LiF film. The carbon layer almost completely absorbs the incident laser energy of the laser light (emerging from the substrate side) and energetically couples with the LiF film as well, resulting in complete ablation of both thin films. However, in this process, practically no ablation results from the substrate. In this experiment, laser fluence could be varied between 2 to 40 J/cm^2 (techniques used are described later). It was ensured that the substrate material was not ablated even at the highest laser fluence.

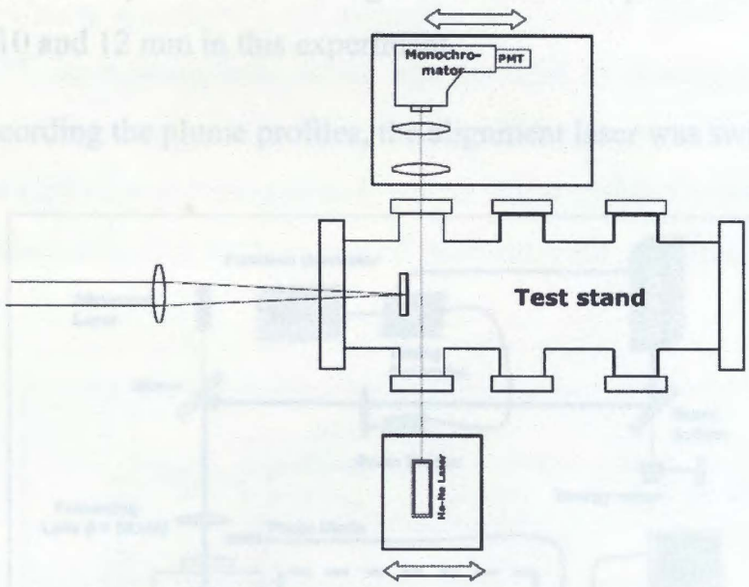

Figure 5-5 The laser blow-off (LBO) spectrometer assembled on a general purpose Test Stand vacuum chamber.

A 0.2 m monochromator ($\Delta\lambda$~1.25 nm) with a fast photomultiplier (Burle 31034) as the detector was mounted on a platform, which was mounted on a single-stage translation stage. In front of the entrance slit of the monochromator, a 2-element optics designed using ***Beam-3*** ray-tracing optics was mounted on the same platform. This optics images the plume formed by the laser ablation on the entrance slit of the monochromator. The slit width determined the spatial resolution, and in this set of experiments, it was ~0.5 mm.

A Nd:YAG laser, operated in fundamental wavelength ablated the thin film, and the plume evolved along the axis of the apparatus, in the direction of incident laser light. Details of the laser are described later.

Using a pair of He-Ne lasers, set along orthogonal directions, the axis and the plane of observation were determined. The alignment laser beam, grazing the target plate was made to fall at the center of the entrance slit of the monochromator (after passing through the 2-lens optics). This alignment laser was mounted on a single-stage stage with a calibrated scale and with micrometer control. In order to vary the distance from the target and plane of observation, first the alignment laser is translated by the required distance. Then the platform holding the telescope and the monochromator was also moved in the same direction, bringing the alignment laser beam right at the middle of the entrance slit of the monochromator. By this method, target-to-observation plane distances were set to 2, 4, 6, 8, 10 and 12 mm in this experiment.

While recording the plume profiles, the alignment laser was switched off.

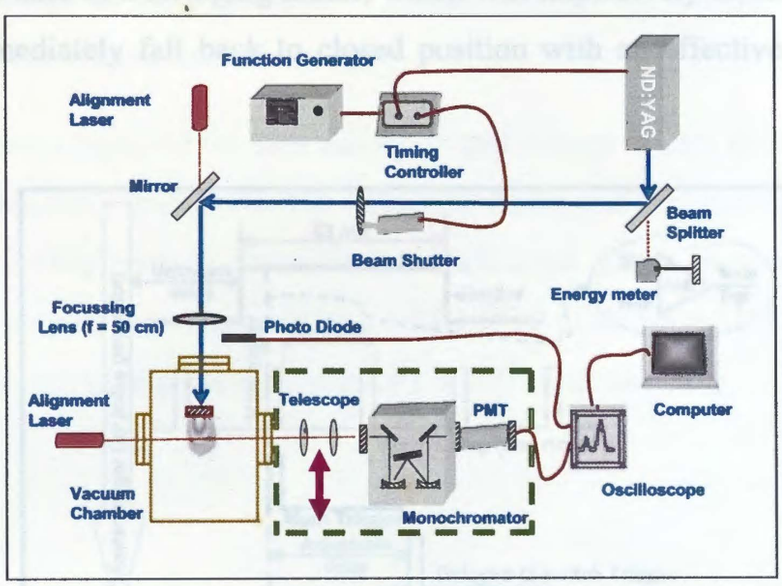

Figure 5-6 The schematic of laser blow-off (LBO) experiment, showing various modules used for recording the plume profile.

Figure 5-6 shows the scheme of the LBO experiment. A flash lamp pumped Nd:YAG laser (Quantel, France), operated at its fundamental wavelength was used to ablate the thin film. The maximum energy of this laser was 1.6 J. A 5% beamsplitter reflected most of the light onto another folding mirror, which directed the laser onto the target along the axis of the chamber. The transmitted light at the beam splitter was monitored using an energy meter. By means of the axial alignment laser and cross wire at two axial ports, first the axis of the

apparatus was determined. Then the Nd:YAG was aligned to this axis using the in-built guiding He-Ne laser beam of the YAG laser (not shown in the figure). Similarly, before setting up the monochromator, the transverse He-Ne laser also aligned using cross wire at the port.

Once the YAG laser is switched on, the flash lamp is continuously on at 30 Hz frequency. It was observed that, the flash lamp pulses contained sufficient energy to ablate the LiF-C film from the substrate. Therefore, some scheme had to be made to block-off the flash lamp pulses, but to open the shutter at a command signal and to allow the following Q-switched laser pulse to interact with the thin film. For this purpose, a normally-off swinging mechanical shutter was placed along the Nd:YAG laser beam path, which was operated by issuing a logic pulse to its control unit by means of a pulse generator. The thin metallic shutter was secured onto the axel of a swinging motor, which will impulsively turned its axis by 90^{O} and immediately fall back to closed position with an effective opening time of 83 ms.

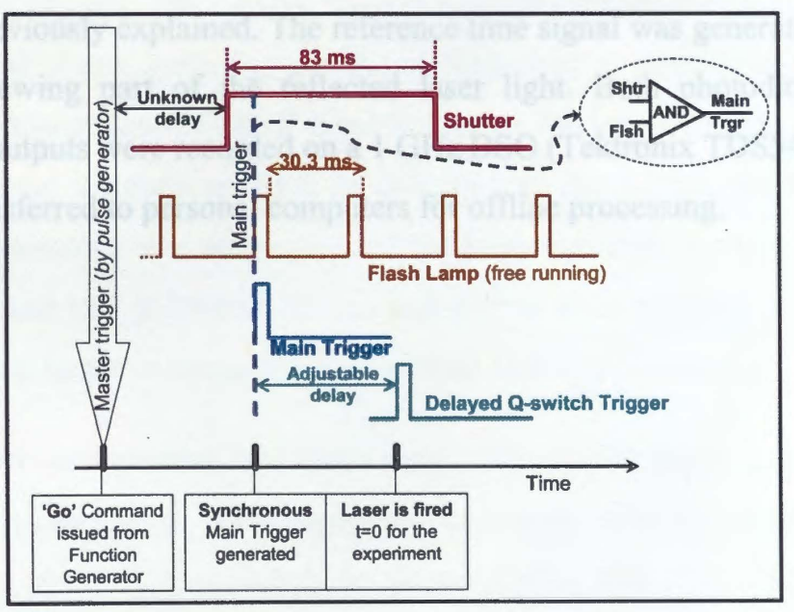

Figure 5-7 The sequencing of timings and scheme of time synchronization used in the LBO experiment.

The period of flash lamp is 30.3 ms (reciprocal of frequency) and therefore the shutter opening will allow more than two flash lamp pulses to be transmitted to the apparatus side (see Figure 5-7). One has to ensure that the laser is Q-switched on the first admitted flash lamp pulse itself. Further, since there is no

time correlation between the 'master trigger' and the 'first-admitted-flash lamp pulse', it is necessary to make a synchronization scheme between these two timed events. This is achieved by ANDing the two pulses using a fast-AND circuit. The AND circuit generated a fast logic pulse synchronous with the flash lamp, thereby Q-switching of the laser in single-shot mode.

The 'Go' command to the Q-switch is issued using another pulse, which is delayed with respect to the main trigger. This was generated by a delay generator. The energy stored in the YAG crystal was maximum after 280 μs from the pulsing of flash lamp. So, for obtaining maximum YAG laser energy, the Q-switch was turned on after a delay of 280 μs. Laser pulses with lesser, but stable energies were generated by further delaying trigger to the Q-switch. It was possible to operate the laser at as low energies as ~100 mJ in a stable and reproducible manner. The energy in each pulse was determined by the energy monitor, normalized with respect to a known energy.

The scheme employed for data collection and storage is very much similar to the scheme previously explained. The reference time signal was generated from a photodiode viewing part of the reflected laser light. Both photodiode and Photomultiplier outputs were recorded on a 1 GHz DSO (Tektronix TDS540). The records were transferred to personal computers for offline processing.

Chapter 6

Initial observations on the dynamics of plasma plume and isolation of plasma components

6.1 Introduction

The feverish research activity in the field of laser produced plasma has lead to a considerable increase in our knowledge regarding the dynamics of plasma plume in vacuum as well as in ambient at higher pressures [1, 2]. Various models have been propounded to explain the motion of the plasma plume and the transient nature of the plasma parameters [3-6]. Numerous experiments have been performed to investigate the evolution of the plasma plume, the major observations (within the purview of the plume dynamics) being the plume splitting phenomena [7-9], dependence of plume dynamics on the mass of the target [10], and varied angular distribution of the charged and neutral species of the plasma plume [11, 12]. The present chapter concerns the investigation of the factors affecting the plume dynamics and the methodology to numerically isolate the various components (ensemble of plasma species having a unique velocity distribution) from the temporal profiles. In this context, the technique of optical time of flight spectroscopy was employed and the temporal profiles of the neutral species Al I, Cu I and Pb I at 396nm, 522nm and 414nm were recorded at various distances away from target in vacuum and at various ambient pressures.

This chapter is organized into three main sections. Section 6.2 discusses the impact of the atomic mass of the target on the expansion velocity of plasma front in vacuum. Here, it has also been demonstrated that the square root dependence of the expansion velocities on the atomic mass of the target could be improved if one considers the translational temperature of the plasma species. Besides this, the expansion of plasma plume in medium at higher pressures has also been studied to establish the relation between atomic mass of the target and the time at which the expansion dynamics of the plume makes a transition from blast wave regime to drag regime. Section 6.3 deals with the component specific

analysis of the temporal profiles. This section explicitly explains the logistic underlying the procedure of isolating the components from the temporal profiles. The temporal profiles corresponding to vacuum have been analyzed using the proposed methodology and the spatial variation of retrieved plasma has been discussed. Finally, the important findings of the experiment have been summarized in section 6.4.

6.2 Influence of atomic mass on gas dynamics of plume expansion

6.2.1 Free expansion of plume

Temporal profiles of the transitions at specific wavelength corresponding to neutral species were recorded at various distances normal to the target. The details of the lines investigated are enlisted below.

Species	Wavelength (A)	Transition
Al I	3961.520	$3s^2 3p\text{-}3s^2 4s$
Cu I	5218.20	---
Pb I	4057.807	---

Table 6-1 Atomic lines investigated to study the dynamics of plasma plume.

In vacuum the plasma moves without any friction and the expansion of the plume is modeled by free expansion model [13, 14]. According to this model, the position plume front is directly proportional to time elapsed *i.e.*

$$R(t) = V_f \times t + R_0 \qquad (6.1)$$

where R is the position of the plume front at time t and V_f is the velocity of the plasma plume . Hence the linearity of the position-time plot of the plasma front is an indication of free expansion of plasmas. Figure 6-1 depicts the spatial dependence of the plume front on time in vacuum (10^{-5} mbar) for Aluminum, Copper and Lead plasmas.

From the figure it is observed that for the distances less than 6 mm the plume front position of all the elements shows deviation from linear dependence on time. The observed non-linearity is due the fact that during the initial stages of

plasma evolution, the thermal energy of the plasma constituents is very high. As plasma expands the thermal energy of the plasma species get converted to its kinetic energy thereby imparting very high velocities to the plasma front.

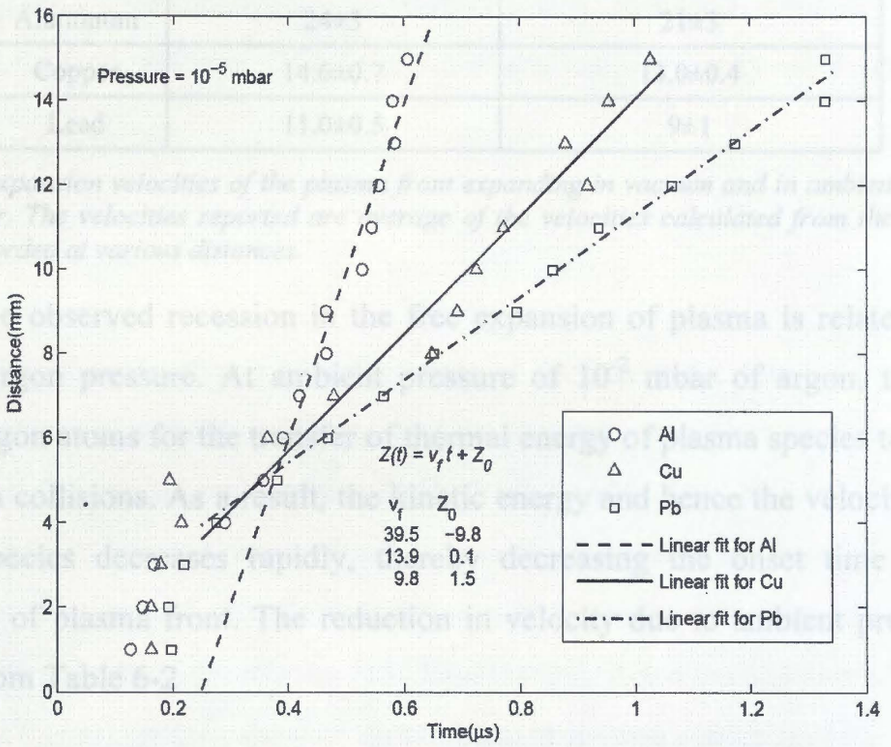

Figure 6-1 Linear expansion of the plume front of various targets with respect to time in vacuum. The velocity of aluminum species is about four times higher than that of Lead.

Once all the thermal energy is used up in plasma expansion, the plasma front no more accelerates and moves with a constant velocity thereafter. The constancy of the expansion velocities is evident from the linearity of the distance-versus-time plots for distances beyond 6 mm. It is interesting to observe that for all the three targets studied, the free expansion commences after about 0.4 μsec of plasma expansion. Similar studies were performed at 10^{-2} mbar argon pressure in the expansion region of the plume. The velocities of various species averaged over the distances beyond 6 mm in vacuum and 10^{-2} mbar pressure are presented in Table 6-2

The distance versus time plot for plasmas of various elements at 10^{-2} mbar argon pressure is shown in Figure 6-2. As evident from the figure, the free plasma expansion now begins at around 0.3 μsec after plasma expansion. Thus the onset time for free expansion has receded from about 0.4 μsec to 0.3 μsec as pressure increased from 10^{-5} mbar to 10^{-2} mbar.

Element	Velocity at 10^{-5} mbar (Averaged over Distance) (Km/sec)	Velocity at 10^{-2} mbar of argon (Averaged over distance) (Km/sec)
Aluminum	24±3	21±3
Copper	14.6±0.7	13.0±0.4
Lead	11.0±0.5	9±1

Table 6-2 Expansion velocities of the plasma front expanding in vacuum and in ambient pressure of 10^{-2} mbar. The velocities reported are average of the velocities calculated from the temporal profiles recorded at various distances.

The observed recession in the free expansion of plasma is related to the ambient argon pressure. At ambient pressure of 10^{-2} mbar of argon, there are enough argon atoms for the transfer of thermal energy of plasma species to kinetic energy via collisions. As a result, the kinetic energy and hence the velocity of the plasma species decreases rapidly, thereby decreasing the onset time of free expansion of plasma front. The reduction in velocity due to ambient pressure is evident from Table 6-2

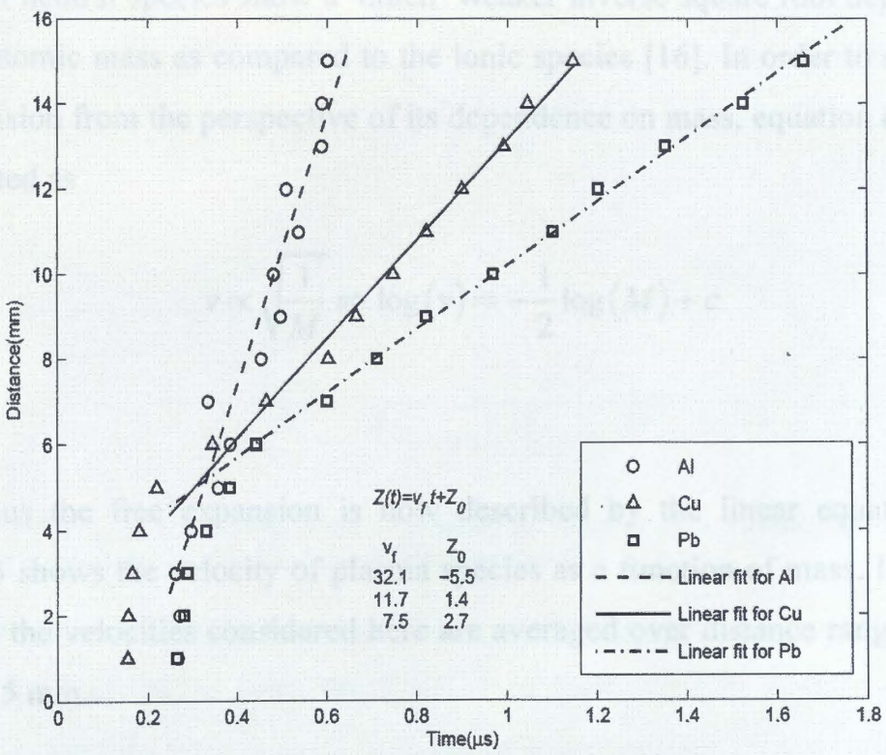

Figure 6-2 Linear expansion of the plume front of various targets with respect to time in ambient at pressure 10^{-2} mbar of argon. Despite there the linearity relation being obeyed, there is a noticeable reduction in expansion velocities due to ambient gas.

The free expansion of the plume is also characterized by the inverse square root dependence of the plasma front velocity on the atomic mass of the ablated species [15]. As discussed earlier, after the termination of the laser pulse the plasma expands adiabatically and the thermal energy of plasma is rapidly released into its expansion velocity. The maximum attainable velocity of expansion is given by

$$v = \left(\frac{2}{\gamma - 1}\right)\sqrt{\frac{\gamma RT}{M}} \tag{6.2}$$

where R is gas constant and M is the mass of the gas atom. The inverse square root dependence of velocity of the species on its atomic mass has been thoroughly investigated for multi-component YBaCuO target [15, 16]. The species of the multi-component plasma were found to deviate considerably from the inverse square root relation and this discrepancy was attributed to the interaction among the different species of the plasma [15] Besides this, it has been observed that the velocity of neutral species show a much weaker inverse square root dependence on of its atomic mass as compared to the ionic species [16]. In order to study the free expansion from the perspective of its dependence on mass, equation (6.2) was reformulated as

$$v \propto \sqrt{\frac{1}{M}} \Rightarrow \log(v) = -\frac{1}{2}\log(M) + c \tag{6.3}$$

Thus the free expansion is now described by the linear equation(6.3). Figure 6-3 shows the velocity of plasma species as a function of mass. It is to be noted that the velocities considered here are averaged over distance ranging from 7 mm to 15 mm.

As evident from Figure 6-3, slope of the straight line is –0.37 which differs considerably from the value –0.5 as predicted by relation (6.2). The apparent inconsistency occurs because of the negligence of the dependence of expansion velocities of plasmas on the temperature of its species. The decrease in

temperature is attributed to the adiabatic expansion of the plasma after the termination of the laser pulse. The fall in temperature due the plasma expansion is governed by the adiabatic thermodynamic equation

$$T\left[X(t)Y(t)Z(t)\right]^{\gamma-1} = const \tag{6.4}$$

where X, Y and Z are the dimensions of the plasmas, T is the temperature and γ is the ratio of the specific heats at constant pressure and volume. It is important to note here that though the temperature drops of as plasma expands, the rate of decrease of temperature is small at lower temperatures due to the energy regained in the recombination of ions.

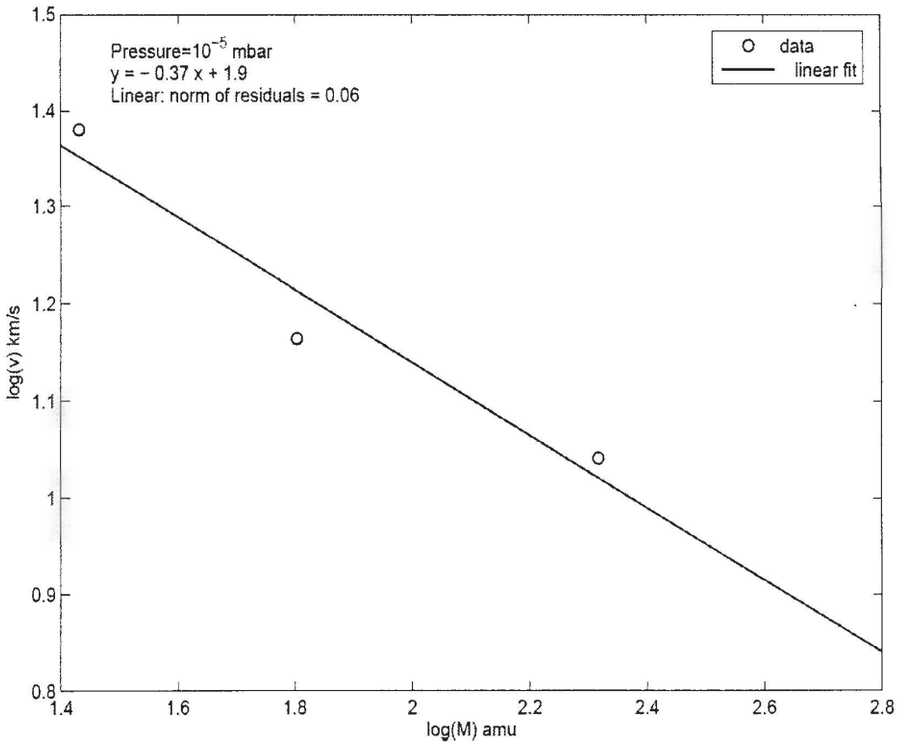

Figure 6-3 Velocity of the plasma front expanding in vacuum as a function of ratio of the translational temperature to the atomic mass of plasma species.

In the present case, temperatures of the neutral species of plasma of different elements were estimated from the FWHM of their velocity distributions. The velocity distributions were derived from the temporal profiles by applying suitable Jacobian transformation. It was observed that for all the targets investigated, the FWHM of the temporal profiles and hence the temperatures of the corresponding species were almost constant for the distance ranging from 7 mm to 20 mm. If one considers the temperature parameter, the relation (6.3) modifies to

$$v \propto \sqrt{\frac{T}{M}} \Rightarrow \log(v) = \frac{1}{2}\log\left(\frac{T}{M}\right) + c \tag{6.5}$$

The role of temperature is evident from Figure 6-4. It shows the dependence of velocity of the plasma species on the ratio of its temperature and mass. According to equation (6.3), the slope of the fitted line in above figure is expected to be 0.5 as against the observed value 0.44. However, the value 0.44 is a considerable improvement over the previous case where the temperature was not considered as a factor determining the velocity of the plume front. The importance of temperature in determining the velocity of the species is further indicated by the improvement in the fitting brought about by including the temperature in the expression determining the velocity of the plasma plume front. Further the value of ratio c_p/c_v as determined from the intercept of the fitted line is 1.9 and is considerably closer to the known value 1.66.

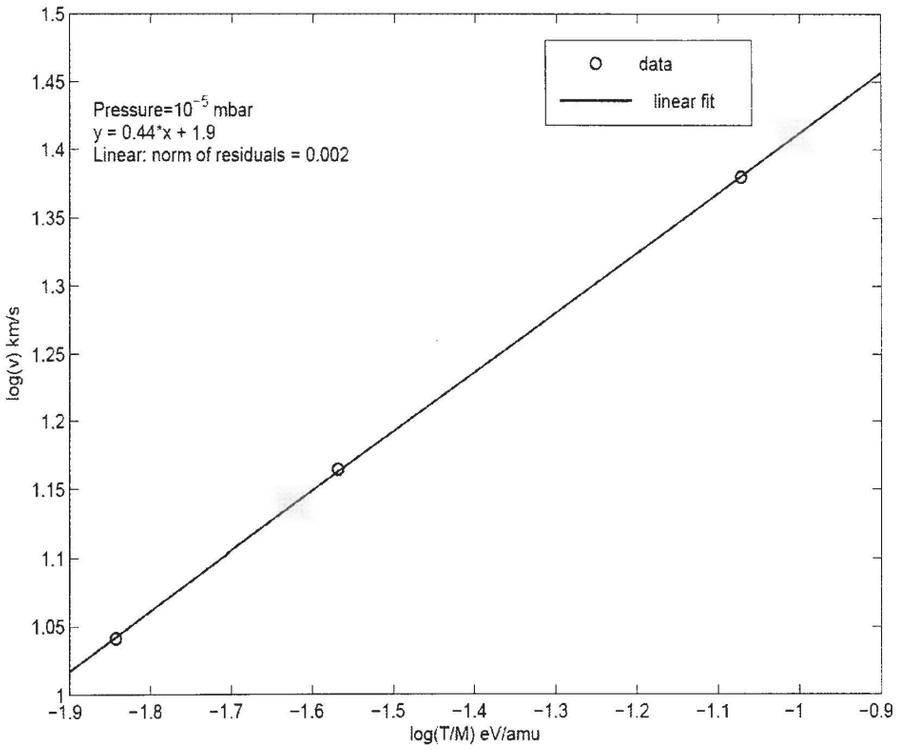

Figure 6-4 Velocity of the plasma front expanding in vacuum as a function of ratio of the translational temperature to the atomic mass of plasma species.

6.2.2 Influence of atomic mass of plasma species on expansion of plume in ambient gas

The expansion of the plasma plume into the buffer gas is widely understood by blast wave model [17, 18]. According to this model, the position of the shock front from the point of explosion R at time t is given by

$$R(t) = \xi \left(\frac{E_p}{\rho_g} \right)^{\frac{1}{5}} t^{\frac{2}{5}} \tag{6.6}$$

where E is the energy the laser pulse deposits in ρ_g plasma plume. E_p is the background gas density and ξ is a numerical constant. In writing equation (6.6), the hemispherical expansion of plume is assumed. Background gas has profound effect on the formation and evolution of shock waves. In fact, for the blast waves to occur, the ambient pressure has to be negligible in comparison to the pressure inside the plasma plume. In other words, the explosion energy must far exceed the internal energy of the ambient gas which has been set to motion by the plume[17, 19]. Thus the blast wave model is expected to explain the expansion of the plume only during its early period of evolution which corresponds to a small region in the vicinity of the target. At later times the density of the plume has decreased considerably in comparison to that of the ambient gas and the blast wave model ceases to describe the motion of plume. In this regime where the density of the plume is comparable to the density of the ambient gas, the plasma plume experiences a viscous drag proportional to the velocity of the plume due to the denser ambient and the expansion is best modeled by drag force model [17, 20, 21]. According to this model, position of the plume front at time t is given by

$$R(t) = R_0 \left[1 - e^{-\beta t} \right] \tag{6.7}$$

where R is the position of the plume front at time t. R_0 is the stopping distance. β is the drag coefficient.

As the plume expands, it transfers its kinetic energy to the ambient gas and the maximum fraction of the energy transferred to the ambient is given by

$$f = \frac{\Delta E}{E} = \frac{M_a}{M_a + M_p} \tag{6.8}$$

where E is the kinetic energy of the plume species. ΔE is the energy transferred to the ambient gas. M_p is the atomic mass of the plume species and M_a is the atomic mass of the ambient gas atom [19, 22]. It is evident from the above expression that for a collision event involving the particles with small difference in their masses, the transfer of the energy is more efficient. Table 6-3 shows the fraction of the kinetic energy transferred when Aluminum, Copper and Lead atoms collide with the ambient argon atoms.

Element	Mass (amu)	Fraction of energy transferred
Aluminum (M_p)	26.98	0.60
Copper (M_p)	63.54	0.37
Lead (M_p)	207.2	0.16
Argon (M_a)	39.94	

Table 6-3 Fraction of the kinetic energy of the plume species transferred to the ambient gas atoms.

From Table 6-3, it is obvious that the species of the aluminum plasma transfers its kinetic energy most efficiently to the ambient argon gas atom. As a result it is very likely that the thermal energy of the plasma is rapidly transferred to the ambient argon atoms, which imply that the transition of the expansion regime of aluminum plasma from the point blast regime to drag regime takes place at shorter distances as compared to the plasmas of copper and lead. Figure 6-5, Figure 6-6 and Figure 6-7 depict the influence of the atomic mass on the transition of the expansion regime from point blast wave to the drag regime for plasmas of three different elements. It is evident from the figure (*cf.* Figure 6-5 to Figure 6-7) that with the increase in atomic mass the transition takes place at larger distances away from the target. For aluminum the transition takes place at around 5 mm away from the target while for lead this distance turns out to be 20 mm.

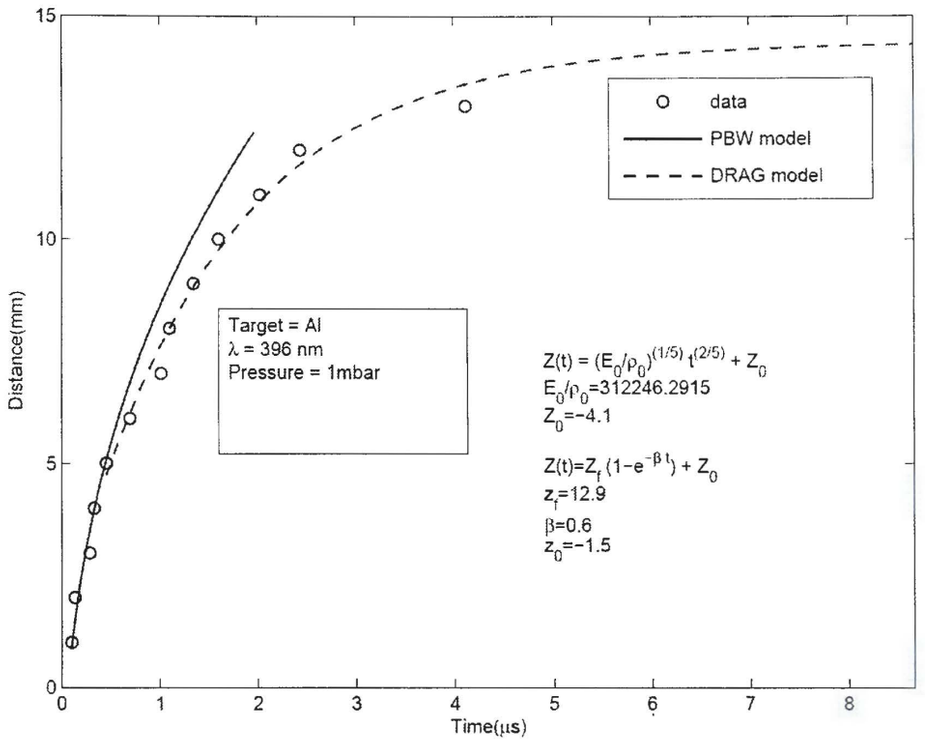

Figure 6-5 Nonlinear expansion of aluminum plasma front in ambient at pressure of 1 mbar of Argon. A combination of PBW model and drag model is required to explain the expansion of plasma front. The transition from PBW to drag model takes place at around 5mm.

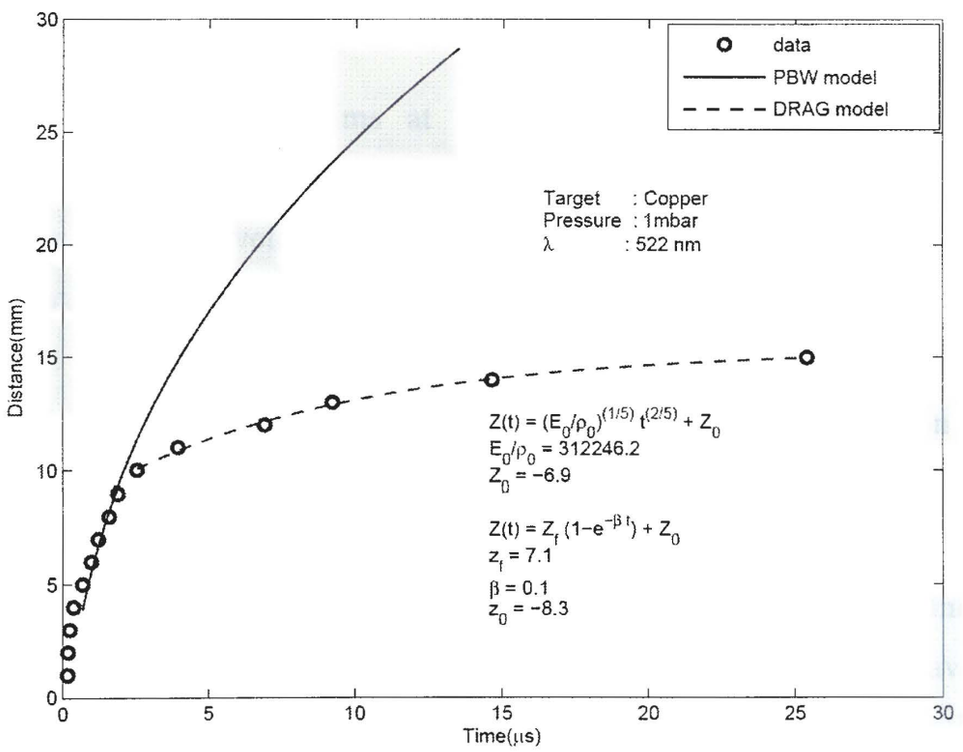

Figure 6-6 Nonlinear expansion of copper plasma front in ambient at pressure of 1 mbar of Argon. The transition from PBW to drag model takes place at around 10mm.

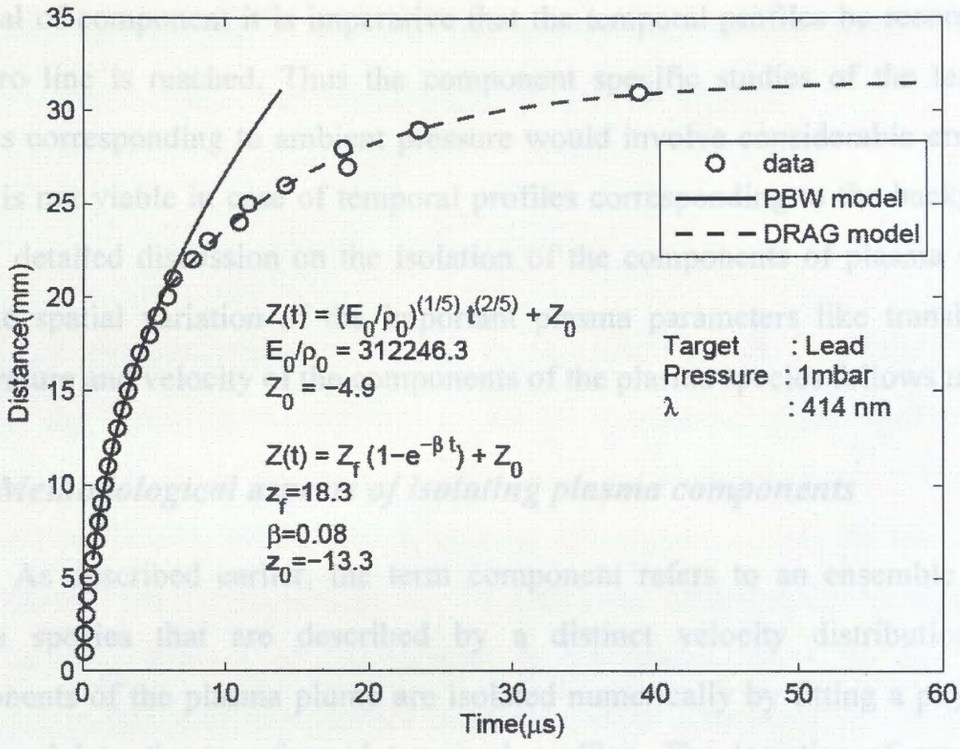

Figure 6-7 Nonlinear expansion of lead plasma front in ambient at pressure of 1 mbar of Argon. The transition from PBW to drag model takes place at around 20mm.

6.3 Component specific studies of plume species

The present section aims at analyzing the TOF profiles from the component view point. The term component here refers to an ensemble of species described by a distinct velocity distribution and it is assumed that the plasma species is stratified into different components. Such an analysis is justified on the premise that the plasma plume consists of the species having distinct velocity distributions whose genesis could be traced to plume splitting phenomenon. Prior to isolation of the components, the temporal profiles are first transformed to the velocity domain. The transformation of the temporal profiles to the velocity domain offers a twofold advantage. Firstly, the undue interference of the fast component which contributes negligible to the temporal profile can be avoided and secondly the averaging of the profile involved during transformation mitigates the ill-effects of the noise present in the temporal profile. In present context, only the evolution of the plasma components in vacuum has been addressed. Such studies were not undertaken in presence of ambient gases for the following reasons. At higher pressure the temporal profiles broadens considerably and the temporal signal relapses to zero base level very slowly. However, for the correct

retrieval of component it is imperative that the temporal profiles be recorded till the zero line is reached. Thus the component specific studies of the temporal profiles corresponding to ambient pressure would involve considerable error and hence is not viable in case of temporal profiles corresponding to the background gas. A detailed discussion on the isolation of the components of plasma species and the spatial variation of the important plasma parameters like translational temperature and velocity of the components of the plasma species follows next.

6.3.1 Methodological aspects of isolating plasma components

As described earlier, the term component refers to an ensemble of the plasma species that are described by a distinct velocity distribution. The components of the plasma plume are isolated numerically by fitting a physically valid model to the transformed temporal profiles. The logistics of employing shifted Maxwell-Boltzmann distribution (SMB) to model the plasma species has already been discussed in chapter 4. During evaporation due to laser heating all the desorbed particles moves away from the surface and will have a positive velocity along the normal to the target surface. Hence, after cessation of the laser pulse the gas cloud generated at the target surface acts as a thermodynamically closed system whose center-of-mass moves in the direction normal to the surface. During initial stages, when the density of the ablated cloud is high, the frequent occurrence of collisions among the ablated particles causes the system to relax to its thermodynamical equilibrium [23]. In other words, the particles now exhibit Maxwell-Boltzmann behavior in the moving frame. Further, the velocity distribution of the plasma species is known to be consisting of more than single Maxwellian [24]. Hence the model to be fitted to the transformed temporal profile is given by

$$f(v)=\sum_{k=1}^{N} a_k v^3 e^{-b_k(v-c_k)^2} \tag{6.9}$$

where a_k, b_k and c_k are the model parameters of the k^{th} component. The physical interpretation of these parameters is as follows: a_k is normalization constant, c_k

is the flow velocity, and b_k is related to translation temperature T_k and the mass m_k of the species under consideration according to the relation

$$b_k = \frac{m}{2k_b T_k}$$

where k_b is the Boltzmann constant. It is worth noting that the temperature T_k signifies the spread in the velocity of the k^{th} component of the species under investigation. Owing to the non-orthogonality of the SMB functions, it is possible that the two models with different number of component may fit the velocity distribution of the plasma species equally well. Such an ambiguity increases with the increasing number of components in the model. Thus, to summarize, numerical isolation of components faces two main drawbacks *viz.* no *a priori* knowledge regarding the number of components and lack of uniqueness in components. We propose here a scheme to deal with this problem. The curve peeling philosophy is central to this scheme [25]. First of all single SMB is fitted to the initial portion of the velocity distribution whose lower and upper limits are zero and most probable velocity respectively. The fitted SMB represents the slowest component of the plasma species. The contribution of this slowest component is then subtracted from the velocity profile so that the remnant essentially constitutes the components with higher mean velocities. The higher components are subsequently isolated by recursively following the above steps. The proposed methodology of isolating plasma components is summarized and illustrated in the following points.

1. Transform the given temporal profile to velocity distribution (cf. Figure 6-8)

2. Fit single SMB to the initial part of the velocity distribution. The initial part of the velocity distribution is essentially bound by the end points, zero and the most probable velocities (cf. Figure 6-9)

3. Subtract the fitted SMB from the original velocity distribution. As a result the modified velocity distribution is devoid of one of the components. (cf. Figure 6-10)

4. Calculate the area of the remnant distribution. If it is significant then repeat the steps from 2 to 4 to isolate subsequent components with successively higher mean velocities. (cf. Figure 6-11)

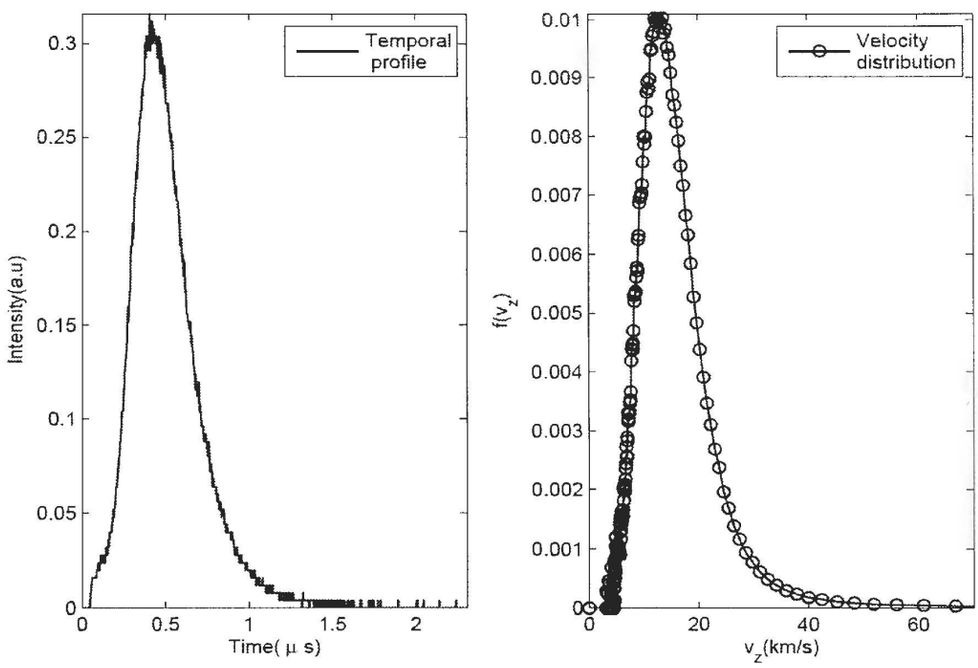

Figure 6-8 Transformation of the velocity distribution of the plasma species in the time domain to velocity domain.

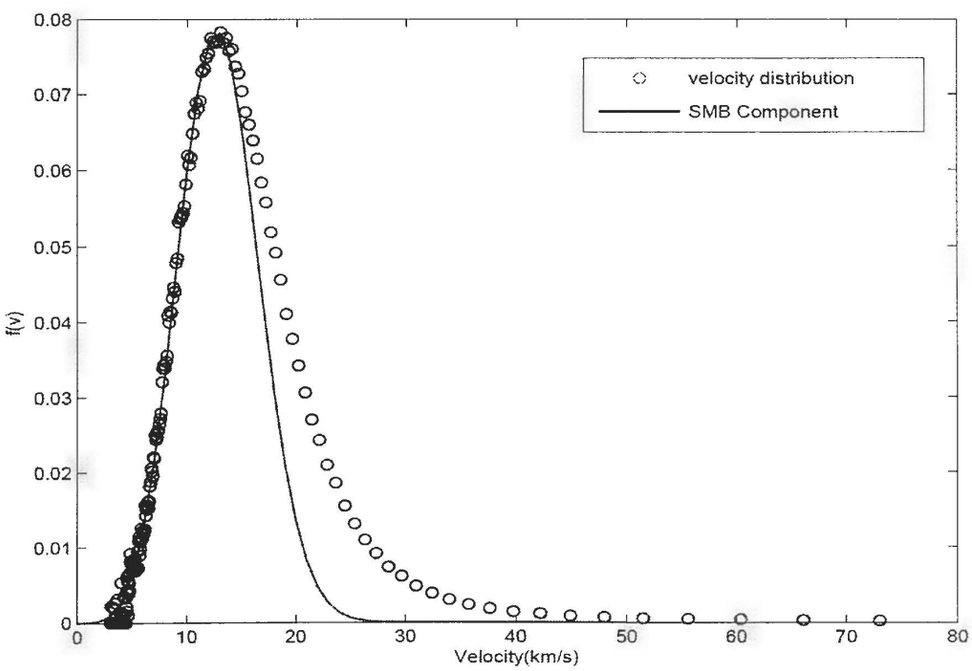

Figure 6-9 A single SMB component is first fitted to the initial part of the velocity distribution.

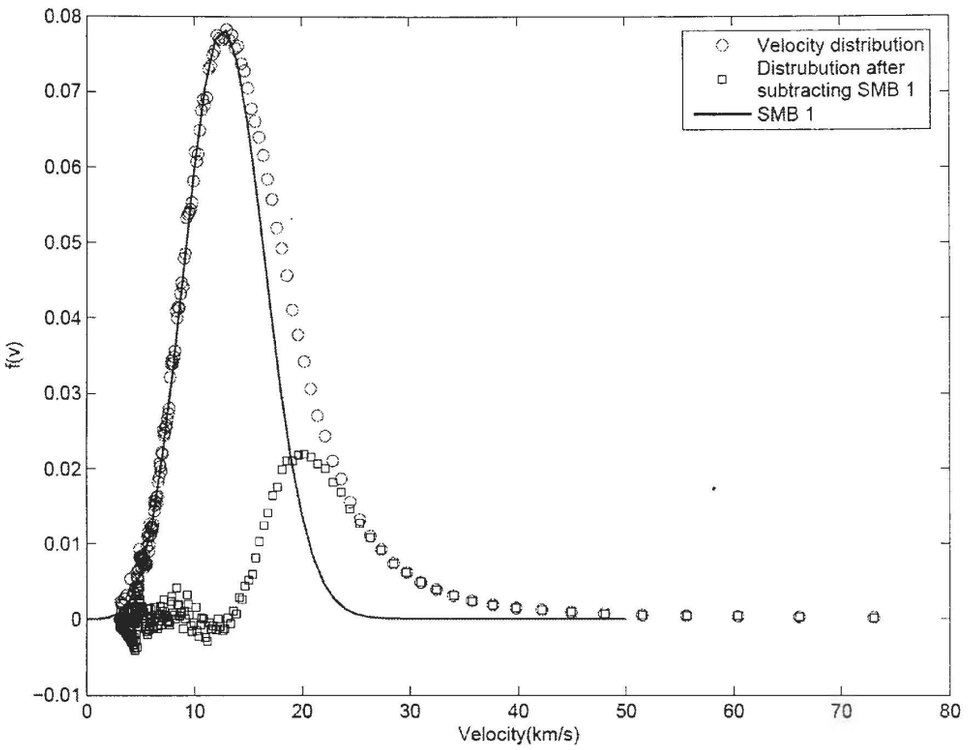

Figure 6-10 The contribution of the component fitted in the previous step is subtracted from the velocity distribution to get the distribution which represents the remaining components.

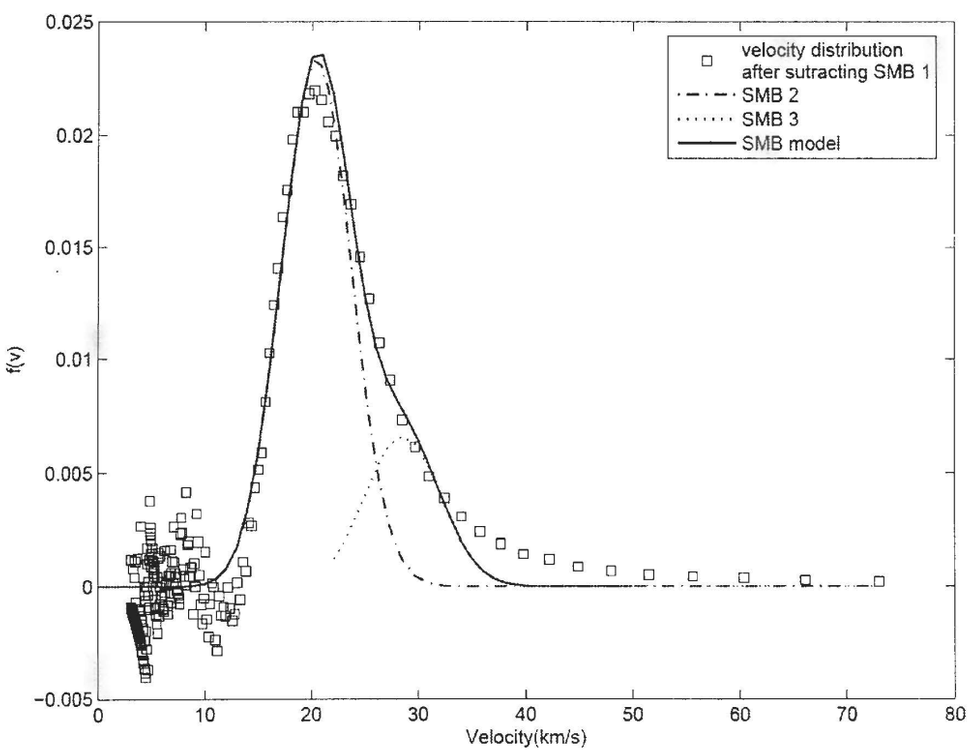

Figure 6-11 Two more components fitted to the remaining distribution following the steps from 2 to 4 of the proposed methodology

It is important to mention here that the successful isolation of components depends on the signal-to-noise (SNR) as well as the resolution with which the data

has been recorded. If either of them is poor the isolation of components is not possible.

6.3.2 Spatial variation of plasma component parameters

As discussed in section 6.2, the plasma formed at the surface of the target expands rapidly whereby the thermal energy of the plume is converted to the kinetic energy of the plasma particles. Hence the plasma parameters vary significantly with both distance and time. Owing to their charge, the charged species are known to have higher velocity as compared to their neutral counterparts. However, neutral species can also have higher kinetic energy if they are formed as a result of recombination. In fact, the multi-Maxwellian nature of the temporal profile could be attributed to the recombination of rapidly moving ion with the electron.

Of late the multi-Maxwellian nature of the temporal profile has been attributed to the nature of the processes involved in ablation of target [26]. Explosive boiling and subsequent absorption of laser light via IB have been associated with the presence of two populations of species with distinct velocity distribution. When a short laser pulse of appropriate intensity is incident on the target, it gets heated rapidly causing the temperature of the target to rise to an extent that the target material reaches the critical point. As a result, the breakdown of material occurs and the mixture of vapor and particulate matter are ejected into the ambient in the direction normal to the surface of the target. The rapid temperature changes cause significant broadening of the velocity distribution of the plasma species. Besides, these species further gain considerable amount of translation energy by IB. Thus, the ensemble of species with such an origin essentially represents the fast component of the velocity distribution. The genesis of the slow component can be understood by considering the fraction of the ejected cloud of material whose constituents constantly undergo collisions among themselves. The collisions, mainly inelastic, of the atomic species with the larger particulate matter ejected concurrently with the atoms reduce its velocity, thereby giving rise to the slow component.

To further investigate the properties of the plasma components, the plasmas of Aluminum, Copper, and Lead expanding in vacuum were studied. Figure 6-12 shows the velocity distribution of the neutral Aluminum species at a distance 10 mm away from the target.

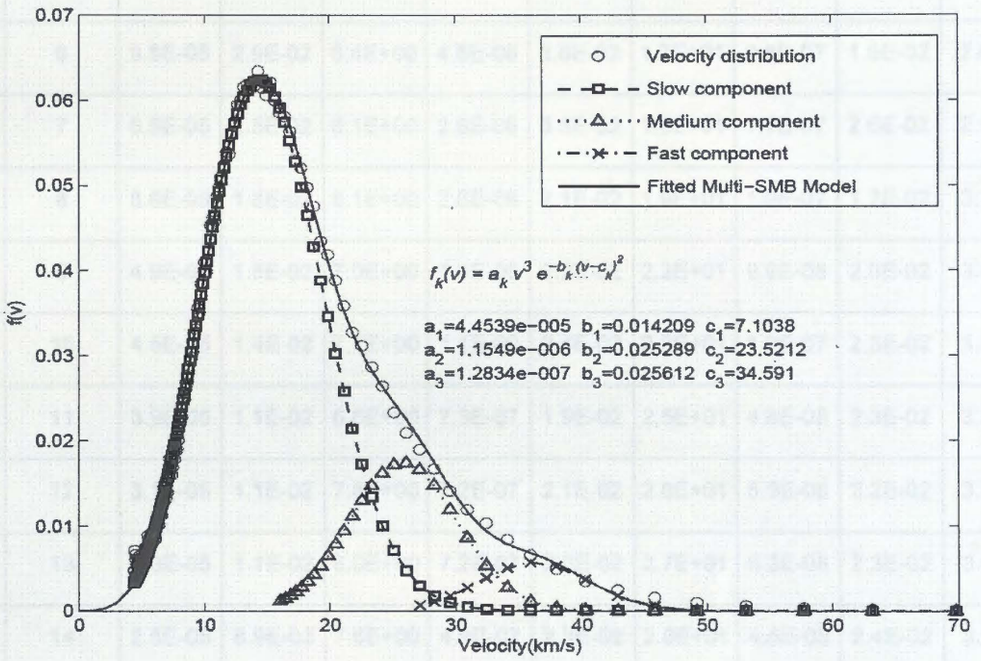

Figure 6-12 Three component multi-Maxwellian model fitted to the data.

The velocity distribution was obtained after numerical transformation of the temporal profile the velocity domain. The solid line tracing the transformed data points represents the multi-Maxwellian model fitted to the data. As evident from the figure, the fitting is excellent. The parameters of the multi-Maxwellian model and corresponding 90% confidence interval (CI) have been presented in the Table 6-4.

Compo-nent	a $\times 10^{-7}$	90% C.I. $\times 10^{-7}$		b $\times 10^{-2}$	90% C.I. $\times 10^{-2}$		c	90% C.I.	
Slow	445	437	453	1.42	1.33	1.51	7.10	6.81	7.39
Medium	11.5	10.9	12.2	2.53	2.05	3.00	23.5	23.2	23.9
Fast	1.28	1.01	1.56	2.56	1.21	3.91	34.6	33.3	35.9

Table 6-4 The values of parameters of the components comprising the multi-Maxwellian model and their 90% confidence interval.

Generally, for all the velocity distributions analyzed, the fitting was good and the value of error (fitting error) in parameters was considerably low. The

values of the model parameters for the temporal profiles of different metals at varied distances have been summarized in Table 6-5, Table 6-6 and Table 6-7.

Sr. No.	Distance (mm)	Fast Component			Medium Component			Slow Component		
		a	b	c	a	b	c	a	b	c
1	6	9.8E-05	2.9E-02	6.4E+00	4.5E-06	3.6E-02	1.7E+01	2.8E-07	1.6E-02	2.6E+01
2	7	6.5E-05	2.5E-02	8.1E+00	2.6E-06	3.5E-02	1.9E+01	1.7E-07	2.6E-02	2.9E+01
3	8	8.6E-05	1.8E-02	5.1E+00	2.6E-06	2.1E-02	1.9E+01	1.9E-07	1.7E-02	3.1E+01
4	9	4.9E-05	1.5E-02	7.0E+00	1.4E-06	2.2E-02	2.2E+01	9.9E-08	2.0E-02	3.4E+01
5	10	4.5E-05	1.4E-02	7.1E+00	1.1E-06	2.4E-02	2.3E+01	1.2E-07	2.3E-02	3.4E+01
6	11	3.9E-05	1.1E-02	6.8E+00	7.3E-07	1.9E-02	2.5E+01	4.8E-08	2.3E-02	3.8E+01
7	12	3.1E-05	1.1E-02	7.8E+00	7.2E-07	2.1E-02	2.6E+01	5.9E-08	2.2E-02	3.8E+01
8	13	3.0E-05	1.1E-02	8.0E+00	7.2E-07	2.3E-02	2.7E+01	6.2E-08	2.3E-02	3.8E+01
9	14	2.5E-05	8.9E-03	7.6E+00	4.9E-07	2.3E-02	2.8E+01	4.5E-08	2.4E-02	3.9E+01
10	15	2.6E-05	1.0E-02	7.8E+00	8.0E-07	2.2E-02	2.6E+01	6.8E-08	2.9E-02	3.8E+01
11	16	2.3E-05	9.3E-03	7.8E+00	6.9E-07	1.9E-02	2.7E+01	4.9E-08	1.9E-02	3.9E+01
12	17	2.6E-05	8.2E-03	6.5E+00	6.0E-07	2.5E-02	2.7E+01	7.1E-08	2.7E-02	3.7E+01
13	18	3.7E-05	5.1E-03	7.2E-01	3.8E-07	1.5E-02	2.8E+01	2.5E-08	1.6E-02	4.4E+01

Table 6-5 The values of parameters of the components comprising the multi-Maxwellian model that was fitted to the velocity distribution of the neutral species of Aluminum plasma

Sr. No.	Distance (mm)	Fast Component			Medium Component			Slow Component		
		a	b	c	a	b	c	a	b	c
1	6	1.3E-03	1.0E-01	2.0E+00	9.1E-05	1.1E-01	7.8E+00	1.4E-05	8.6E-02	1.3E+01
2	7	1.7E-03	5.7E-02	7.9E-01	6.2E-05	9.3E-02	8.8E+00	1.0E-05	1.1E-01	1.4E+01
3	8	2.0E-03	4.7E-02	1.3E-01	6.7E-05	1.7E-01	8.7E+00	2.0E-05	5.1E-01	1.2E+01
4	9	8.4E-04	5.2E-02	2.2E+00	3.7E-05	5.5E-02	1.0E+01	2.0E-06	5.8E-02	1.9E+01
5	10	7.3E-04	4.0E-02	1.7E+00	3.0E-05	1.1E-01	1.1E+01	6.4E-06	1.7E-01	1.6E+01
6	11	5.7E-04	6.4E-02	3.0E+00	4.6E-05	6.7E-02	1.0E+01	3.9E-06	4.8E-02	1.7E+01
7	12	4.1E-04	5.0E-02	3.5E+00	3.3E-05	6.5E-02	1.1E+01	2.2E-06	6.3E-02	1.8E+01
8	13	3.3E-04	5.8E-02	4.3E+00	3.2E-05	5.7E-02	1.1E+01	2.3E-06	6.3E-02	1.9E+01
9	14	3.1E-04	1.1E-01	5.0E+00	5.7E-05	8.6E-02	1.0E+01	7.4E-06	6.6E-02	1.6E+01
10	15	2.7E-04	5.6E-02	4.4E+00	3.3E-05	6.7E-02	1.2E+01	3.1E-06	6.9E-02	1.8E+01
11	16	2.2E-04	7.7E-02	5.6E+00	3.3E-05	7.0E-02	1.2E+01	3.3E-06	6.6E-02	1.8E+01
12	17	2.0E-04	5.0E-02	5.6E+00	2.3E-05	8.5E-02	1.3E+01	3.1E-06	8.6E-02	1.8E+01
13	18	2.9E-04	2.1E-02	3.6E+00	9.5E-06	7.3E-02	1.5E+01	1.8E-06	9.4E-02	2.1E+01
14	19	2.4E-03	3.1E-02	7.9E+00	1.1E-04	7.8E-02	1.8E+01	1.5E-05	1.4E-01	2.4E+01
15	20	4.2E-04	4.4E-02	3.2E+00	4.3E-05	9.3E-02	1.2E+01	7.6E-06	1.2E-01	1.7E+01

Table 6-6 The values of parameters of the components comprising the multi-Maxwellian model that was fitted to the velocity distribution of the neutral species of Copper plasma

Sr. No.	Distance (mm)	Fast Component			Medium Component			Slow Component		
		a	b	c	a	b	c	a	b	c
1	9	3.7E-03	1.3E-01	9.5E-01	2.3E-04	6.0E-02	5.8E+00	8.6E-06	6.7E-02	1.3E+01
2	10	2.4E-03	1.2E-01	1.2E+00	2.0E-04	6.2E-02	6.3E+00	9.4E-06	5.7E-02	1.3E+01
3	11	1.9E-03	8.0E-02	1.1E+00	1.2E-04	7.5E-02	7.7E+00	7.6E-06	7.0E-02	1.4E+01
4	12	1.5E-03	6.1E-02	1.3E+00	9.1E-05	8.3E-02	8.4E+00	6.4E-06	7.8E-02	1.5E+01
5	13	1.4E-03	4.4E-02	6.7E-01	5.9E-05	6.3E-02	8.9E+00	2.8E-06	7.0E-02	1.6E+01
6	14	1.2E-03	4.4E-02	1.1E+00	5.5E-05	7.4E-02	9.1E+00	2.9E-06	7.8E-02	1.6E+01
7	15	8.7E-04	3.2E-02	1.2E+00	1.6E-05	7.7E-02	1.2E+01	1.9E-06	6.3E-02	1.7E+01
8	16	9.3E-04	2.9E-02	8.8E-01	8.0E-06	5.6E-02	1.2E+01	6.4E-07	5.2E-02	1.8E+01
9	17	9.3E-04	2.5E-02	3.4E-01	7.1E-06	7.8E-02	1.2E+01	1.1E-06	8.3E-02	1.8E+01
10	18	6.7E-04	3.1E-02	1.9E+00	8.1E-06	1.0E-01	1.3E+01	1.3E-06	9.0E-02	1.8E+01
11	19	7.0E-04	2.4E-02	9.1E-01	3.5E-06	8.2E-02	1.5E+01	4.3E-07	6.5E-02	2.1E+01
12	20	7.3E-04	2.8E-02	1.2E+00	5.8E-06	6.9E-02	1.4E+01	5.3E-07	7.3E-02	2.1E+01
13	21	4.7E-04	5.3E-02	3.9E+00	2.2E-05	1.0E-01	1.1E+01	2.7E-06	1.0E-01	1.7E+01
14	22	5.8E-04	3.4E-02	2.3E+00	9.9E-06	9.5E-02	1.2E+01	1.7E-06	1.2E-01	1.8E+01
15	23	6.8E-04	2.5E-02	9.1E-01	4.2E-06	1.7E-01	1.4E+01	1.3E-06	1.2E-01	1.8E+01
16	24	6.7E-04	2.1E-02	1.3E-01	1.8E-06	1.1E-01	1.5E+01	6.0E-07	3.9E-01	2.0E+01
17	25	3.8E-04	2.5E-02	2.3E+00	5.0E-06	7.2E-02	1.3E+01	1.3E-06	2.3E-01	1.8E+01
18	26	3.7E-04	2.5E-02	2.4E+00	3.6E-06	3.5E-02	1.4E+01	1.9E-07	1.1E-01	2.5E+01
19	28	4.7E-04	2.7E-02	2.2E+00	4.5E-06	1.4E-01	1.4E+01	1.5E-06	1.3E-01	1.8E+01
20	29	6.4E-04	2.5E-02	9.2E-01	2.9E-06	5.4E-02	1.4E+01	2.8E-07	3.6E-02	2.2E+01
21	30	4.0E-04	5.3E-02	4.5E+00	1.3E-05	2.8E-01	1.2E+01	4.4E-06	2.4E-01	1.5E+01

Table 6-7 The values of parameters of the components comprising the multi-Maxwellian model that was fitted to the velocity distribution of the neutral species of Lead plasma

Using these model parameters the translational temperature and the centre-of-mass velocities were calculated to study the spatial evolution of these plasma parameters for different components. The spatial variation in the translational temperature and the centre of mass velocity of different components is presented in Figure 6-13.

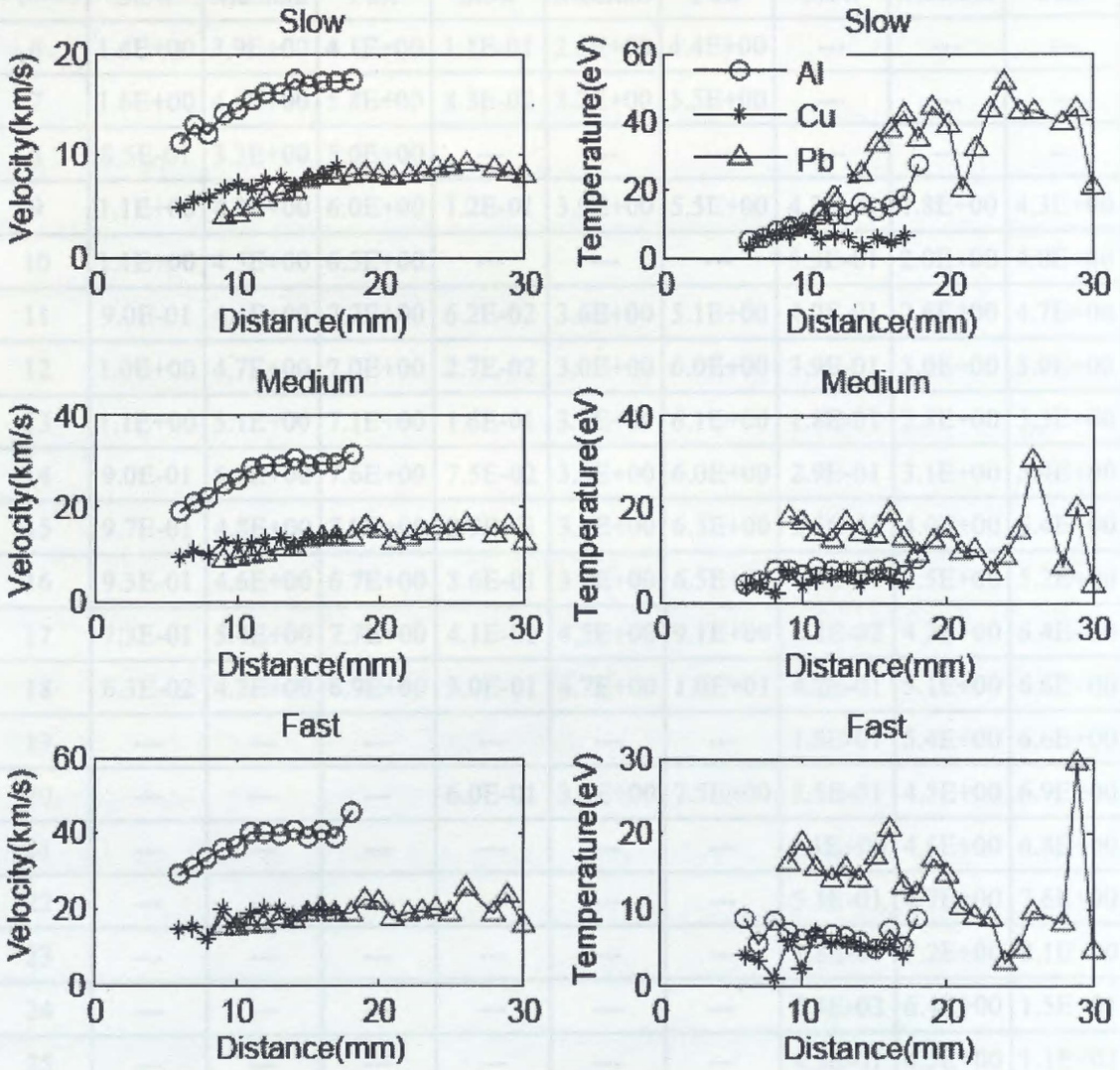

Figure 6-13 Spatial variation in the centre-of-mass velocity and the translational temperature of various species expanding in vacuum.

Further, to quantify the randomness of the particle motion of the plasma species, the Mach number M was calculated [27]. The Mach number is related to centre-of-mass velocity u and the translational temperature T by

$$M = \sqrt{\frac{m v_0^2}{\gamma k T}} \tag{6.10}$$

where γ is the usual specific heat ratio. Here, considering the degrees of freedom associated with ionization and excitation, the value of γ was taken to be 1.3. The values of Mach number at different distances for different metals are listed in Table 6-8.

Z (mm)	Mach Number (Aluminum)			Mach Number (Copper)			Mach Number (Lead)		
	Slow	Medium	Fast	Slow	Medium	Fast	Slow	Medium	Fast
6	1.4E+00	3.9E+00	4.1E+00	1.1E-01	2.5E+00	4.4E+00	---	---	---
7	1.6E+00	4.4E+00	5.8E+00	8.3E-02	3.2E+00	5.5E+00	---	---	---
8	8.5E-01	3.3E+00	5.0E+00	---	---	---	---	---	---
9	1.1E+00	4.1E+00	6.0E+00	1.2E-01	3.9E+00	5.5E+00	4.2E-01	1.8E+00	4.3E+00
10	1.1E+00	4.5E+00	6.5E+00	---	---	---	5.3E-01	2.0E+00	4.0E+00
11	9.0E-01	4.4E+00	7.2E+00	6.2E-02	3.6E+00	5.1E+00	4.0E-01	2.6E+00	4.7E+00
12	1.0E+00	4.7E+00	7.0E+00	2.7E-02	3.0E+00	6.0E+00	3.9E-01	3.0E+00	5.0E+00
13	1.1E+00	5.1E+00	7.1E+00	1.6E-01	3.7E+00	6.1E+00	1.8E-01	2.8E+00	5.3E+00
14	9.0E-01	5.3E+00	7.6E+00	7.5E-02	3.5E+00	6.0E+00	2.9E-01	3.1E+00	5.4E+00
15	9.7E-01	4.8E+00	7.9E+00	2.9E-01	3.4E+00	6.3E+00	2.6E-01	4.0E+00	5.4E+00
16	9.3E-01	4.6E+00	6.7E+00	3.6E-01	3.7E+00	6.5E+00	1.9E-01	3.5E+00	5.2E+00
17	7.3E-01	5.4E+00	7.7E+00	4.1E-01	4.5E+00	9.1E+00	6.7E-02	4.2E+00	6.4E+00
18	6.3E-02	4.3E+00	6.9E+00	3.0E-01	4.7E+00	1.0E+01	4.2E-01	5.1E+00	6.6E+00
19	---	---	---	---	---	---	1.8E-01	5.4E+00	6.6E+00
20	---	---	---	6.0E-01	3.5E+00	7.5E+00	2.5E-01	4.5E+00	6.9E+00
21	---	---	---	---	---	---	1.1E+00	4.6E+00	6.8E+00
22	---	---	---	---	---	---	5.3E-01	4.7E+00	7.6E+00
23	---	---	---	---	---	---	1.8E-01	7.2E+00	8.1E+00
24	---	---	---	---	---	---	2.3E-02	6.4E+00	1.5E+01
25	---	---	---	---	---	---	4.5E-01	4.5E+00	1.1E+01
26	---	---	---	---	---	---	4.8E-01	3.3E+00	1.0E+01
28	---	---	---	---	---	---	4.5E-01	6.4E+00	8.0E+00
29	---	---	---	---	---	---	1.8E-01	4.1E+00	5.2E+00
30	---	---	---	---	---	---	1.3E+00	8.0E+00	9.3E+00

Table 6-8 Mach number for various components of various plasma species at different distances away from the target

6.4 Conclusion

The role of atomic mass of the species of the laser produced plasma in determining expansion dynamics of plasma in vacuum as well as in ambient argon environment has been investigated. Analysis of the free expansion velocities of aluminum, copper and lead plasmas revealed that the plasma front accelerated up to a distance about 6 mm followed by the free expansion. The time at which the free expansion began was observed to be significantly influenced by the ambient pressure. Further, the velocities of the plasma front were found to depend weakly on inverse square root of the atomic mass. This dependence was strengthened by the inclusion of the temperature as determined from the FWHM of the temporal profiles recorded at varied distances.

The expansion of the plasma plume at ambient pressure of 1 mbar of argon was explained by a combination of point blast wave model and drag model. The transition of the plasma expansion from point blast wave regime to drag regime was found to strongly depend on the atomic mass of the species of the expanding plasma and the observed dependence was attributed to the fraction of energy transferred to the ambient argon environment during collision. For aluminum, the transition took place at around 5 mm while for lead the transition was observed 20 mm away from the target. Further, in case of copper and lead plasmas, it was observed that below 5 mm the plasma expanded linearly in time. Thus the evolution of plasma plume could be conveniently categorized into three phases. In first phase the plasma expands linearly with time (free expansion) while in second and third phase, the expansion takes place according to point blast wave model and drag model respectively.

The neutral species was found to comprise three main components *viz.* slow, medium and fast. It is found that the components could be more conveniently isolated in the velocity domain rather than in time domain. Using the methodology proposed in this chapter it was possible to analyze the temporal profiles recorded at larger distance despite the signal being low. The model parameters of the components were used to study the spatial variation in temperature and flow velocity of the plasma plume.

References

1. Anisimov S. I., Bauerle D., and Luk'yanchuk B. S., (1993). "Gas dynamics and film profiles in pulsed-laser deposition of materials". *Physical Review B –Condensed Matter and Materials Physics*, **48**(16): pp. 12076 – 12081.

2. Sharma A. K. and Thareja R. K., (2004). "Characterization of laser-produced aluminum plasma in ambient atmosphere of nitrogen using fast photography". *Applied Physics Letters*, **84**(22): pp. 4490-4492.

3. Chen Z., Bleiner D., and Bogaerts A., (2006). "Effect of ambient pressure on laser ablation and plume expansion dynamics: A numerical simulation". *Journal of Applied Physics*, **99**(6): pp. 063304.

4. Garrelie F., Champeaux C., and Catherinot A., (1999). "Expansion dynamics of the plasma plume created by laser ablation in a background gas". *Applied Physics A: Materials Science & Processing*, **69**(0): pp. S55-S58.

5. Ho J. R., Grigoropoulos C. P., and Humphrey J. A. C., (1996). "Gas dynamics and radiation heat transfer in the vapor plume produced by pulsed laser irradiation of aluminum". *Journal of Applied Physics*, **79**(9): pp. 7205-7215.

6. Miotello A. and Kelly R., (1999). "On the origin of the different velocity peaks of particles sputtered from surfaces by laser pulses or charged-particle beams". *Applied Surface Science*, **138-139**: pp. 44-51.

7. Abhilasha, Prasad P. S. R., and Thareja R. K., (1993). "Laser-produced carbon plasma in an ambient gas". *Physical Review E –Statistical, Nonlinear, and Soft Matter Physics*, **48**(4): pp. 2929 – 2933.

8. Geohegan D. B. and Puretzky A. A., (1996). "Laser ablation plume thermalization dynamics in background gases: combined imaging, optical absorption and emission spectroscopy, and ion probe measurements". *Applied Surface Science Proceedings of Symposium F: Third International Symposium on Laser Ablation of the 1995 E-MRS Spring Conference*, **96-98**: pp. 131-138.

9. Wood R. F., Leboeuf J. N., Chen K. R., Geohegan D. B., and Puretzky A. A., (1998). "Dynamics of plume propagation, splitting, and nanoparticle formation during pulsed-laser ablation". *Applied Surface Science*, **127-129**: pp. 151-158.

10. Singh R. K., Holland O. W., and Narayan J., (1990). "Theoretical model for deposition of superconducting thin films using pulsed laser evaporation technique". *Journal of Applied Physics*, **68**(1): pp. 233-247.

11. Issac R. C., Vasudevan Pillai K., Harilal S. S., Varier G. K., Bindhu C. V., Gopinath P., Radhakrishnan P., Nampoori V. P. N., and Vallabhan C. P. G., (1998). "Dynamics of laser produced silver plasma under film deposition conditions studied using optical emission spectroscopy". *Applied Surface Science*, **125**(2): pp. 227-235.

12. Thestrup B., Toftmann B., Schou J., Doggett B., and Lunney J. G., (2002). "Ion dynamics in laser ablation plumes from selected metals at 355 nm". *Applied Surface Science*, **197-198**: pp. 175-180.

13. Arnold N., Gruber J., and Heitz J., (1999). "Spherical expansion of the vapor plume into ambient gas: an analytical model". *Applied Physics A: Materials Science & Processing*, **69**(Supplement 1): pp. S87-S93.

14. Radziemski L. J. and Cremers D. A., eds. *Lasers-induced Plasmas and Applications*. 1989, Marcel Dekker, Inc.: New York. 445.

15. Marine W., Gerri M., d'Aniello J. M. S., Sentis M., Delaporte P., Forestier B., and Fontaine B., (1992). "Analysis of the plasma expansion dynamics by optical time-of-flight measurements". *Applied Surface Science*, **54**: pp. 264-270.

16. Singh R. K., Holland O. W., and Narayan J., (1990). "Theoretical model for deposition of superconducting thin films using pulsed laser evaporation technique". *Journal of Applied Physics*, **68**(1): pp. 233-247.

17. Amoruso S., Bruzzese R., Spinelli N., Velotta R., Vitiello M., and Wang X., (2003). "Dynamics of laser-ablated MgB_2 plasma expanding in argon probed by optical emission spectroscopy". *Physical Review B –Condensed Matter and Materials Physics*, **67**(22): pp. 224503.

18. Franklin S. R. and Thareja R. K., (2004). "Simplified model to account for dependence of ablation parameters on temperature and phase of the ablated material". *Applied Surface Science*, **222**(1-4): pp. 293-306.

19. Angleraud B., Aubreton J., and Catherinot A., (1998). "Expansion of the ablation plume created by ultraviolet laser irradiation of various target materials". *The European Physical Journal - Applied Physics*, **5**: pp. 303-310.

20. Sharma A. K. and Thareja R. K., (2005). "Plume dynamics of laser-produced aluminum plasma in ambient nitrogen". *Applied Surface Science*, **243**(1-4): pp. 68-75.

21. Geohegan D. B., (1992). "Physics and diagnostics of laser ablation plume propagation for high-Tc superconductor film growth". *Thin Solid Films*, **220**(1-2): pp. 138-145.

22. Singh R. K. and Narayan J., (1990). "Pulsed-laser evaporation technique for deposition of thin films: Physics and theoretical model". *Physical Review B –Condensed Matter and Materials Physics*, **41**(13): pp. 8843 – 8859.

23. Kools J. C. S., Baller T. S., Zwart S. T. D., and Dieleman J., (1992). "Gas flow dynamics in laser ablation deposition". *Journal of Applied Physics*, **71**(9): pp. 4547-4556.

24. Harilal S. S., Bindhu C. V., Tillack M. S., Najmabadi F., and Gaeris A. C., (2003). "Internal structure and expansion dynamics of laser ablation plumes into ambient gases". *Journal of Applied Physics*, **93**(5): pp. 2380-2388.

25. Murari M. K., *Component specific luminescence of natural minerals and their application to the dosimetry of natural radiation environment.*

26. Rossa M., Rinaldi C. A., and Ferrero J. C., (2006). "Velocity distributions of Ba ($^1S_0$, ^3D_J, $^1D_2$, $^3P_1$, and $^1P_1$) and Ba^+($^2P_{3/2}$) produced by 1064 nm pulsed laser ablation of barium in vacuum". *Journal of Applied Physics*, **100**: pp. 063305.

27. Zheng J. P., Huang Z. Q., Shaw D. T., and Kwok H. S., (1989). "Generation of high-energy atomic beams in laser-superconducting target interactions". *Applied Physics Letters*, **54**(3): pp. 280-282.

Chapter 7

Dynamics of C and Li species in plasma produced by laser induced blow off of LiF-C films

7.1 Introduction

This chapter concerns the evolution of the Li and C species of the LiF-C plasma. Towards this, the time and space resolved measurements were carried out under different experimental conditions. Distance between the target and field of view, the background pressure and laser fluence were the experimental parameters varied to study the spatial and temporal evolution of the plasma plume. In present case, the scheme employed (*viz.* laser-blow-off) to generate plasma is quite different from the conventional method of producing plasma by laser ablation of solid targets. In laser-blow-off (LBO), or the laser induced forward transfer technique [1], the laser beam interacts with a thin film supported on a thick transparent substrate and the ablated material propagates along the direction of the incident laser beam. The mechanism for the formation of LBO is impulsive heating of the film, until the vapor pressure at the film support interface becomes large enough to expel the film from the support [1, 2]. While the amount of material ablated in conventional LPP plume is governed by thermo-physical properties of the target and opacity of the vapor cloud ablated by the leading edge of the incident laser pulse [3], 100% material from an area equal to the laser spot-size is ejected at every laser shot from a thin film is guaranteed in laser–blow-off technique. This essentially means that the mass ejected per shot is rather independent of the laser fluence beyond the ablation threshold, whereby the density of the plume could be determined rather accurately. Thus, the onset of instabilities in expanding plasma plume in ambient gas could be better studied in LBO experiments. In present context, a discussion pertinent to differences in plasmas produced by LPP and LBO would further elucidate the dependence of plume dynamics on the formative mechanisms involved in production of plasma.

The major difference between LPP and LBO plumes originates from the processes taking place when a laser interacts with the target. When a laser with a few ns pulse width is incident on a solid target, the following stages of plume formation will occur. The leading edge of the laser pulse ejects an envelope of fast moving atoms. Electron collisions are prevalent in this dense plume, where the initial number densities can be as high as 10^{22} cm^{-3}. This causes ionization and excitation of atoms in the front-layer (also known as a fast component). The atoms on the front layer expand unhindered by the trailing slow atoms from the core (known as a slow component). The LPP plasma is found to have a considerable fraction of multiply-charged ions, which depends on the laser fluence. The fraction of multiply-charged ions is found to be negligible in the LBO plasma. The expansion dynamics in LBO will depend on the thickness of the thin film. If the thickness is less than the skin depth, defined as the penetration depth of the laser in a solid target, then it would result in an explosive expansion of plume with less number of thermalizing collisions. In such cases, there is practically little attenuation of the fast component, and in these situations the LBO plume resembles an LPP plume.

At this point, the importance of investigating the dynamics of plasma produced by LBO scheme and the choice of LiF-C thin film as a target needs a special mention. The LBO scheme is better suited for its use in the generation of fast neutral atom beams [4] as a diagnostic tool for the tokamak plasmas. It has been observed that the neutral density in LBO plumes is about an order of magnitude larger than the neutral density in LPP plumes. Moreover, since complete ablation of the irradiated film takes place in every laser shot, the amount of material injected into the tokamak could be easily estimated. This makes interpretation of the results easier. The LBO method has been used to characterize plasma properties such as ion temperature [5], plasma rotation [6], impurity transport [7] and plasma density and electron temperature measurements [8] at the scrape-off-layer (SOL) and at the edge of the plasma. As a result, laser ablation from multi-component targets has been subjected to great attention in recent times. The expansion dynamics, the plasma property of the plume and emission features from atomic components are of particular interest in such studies [9]. A

multilayer LiF-C target is of particular importance because of the low mass and high penetration speeds. Lithium is favored due to the simplicity of its emission spectra. The interaction of laser-induced carbon plasma with ambient gas has also generated a lot of interest because of its application in the thin film preparation of advanced material like fullerenes, single-walled carbon nanotubes and diamond-like carbon (DLC) films [10-12].

In present chapter, the findings of the experiment conducted on LiF-C thin film have been organized into four main sections. Section 1 describes the cursory observations regarding the effect of physical parameters like spatial location of point of observation and ambient pressure on the shape of the temporal profiles of various species. Section 2 addresses the issue of plume stratification into fast and medium component as inferred from the study of various plasma species. Section 3 describes the evolution of the plasma plume in terms of various models. Section 4 describes the role of the laser fluence in governing the dynamics of plasma plume.

7.2 Initial observations on the temporal profiles

Temporal profiles were recorded at distances varying from 1 mm to 12 mm. In order to investigate the effect of ambient environment on the plume expansion, the experiment was performed in argon ambient with base pressure varying from 10^{-6} Torr to 3 Torr. The effect of laser fluence on the plume dynamics also forms a part of present studies and the laser fluence varied from 15 to 40 Jcm^{-2}. An overview of the species investigated and experimental parameters varied during the experiment appears in Table 7-1

Variable	Range of values
Distance between target and field of view (mm)	2 , 4 , 6 , 8 , 10 , 12
Wavelength (nm)	426.7 , 478.8 , 548.4 , 610.3 , 670.8
Pressure (mbar)	1e-6 , 1e-2 , 1 , 3
Energy density (J/cm^2)	15 to 40

Table 7-1 The range of values assumed by various experimental parameters

7.2.1 Temporal profiles in vacuum:

Figure 7-1 depicts temporal profiles recorded at three different distances. The closest distance chosen was 2 mm to avoid the contribution of the continuum emission corresponding to the dense phase of plasma plume. The higher FWHM of the temporal profiles at smaller distances could be attributed to the higher temperature of the plasma plume during its initial stages of evolution when the electron densities are high.

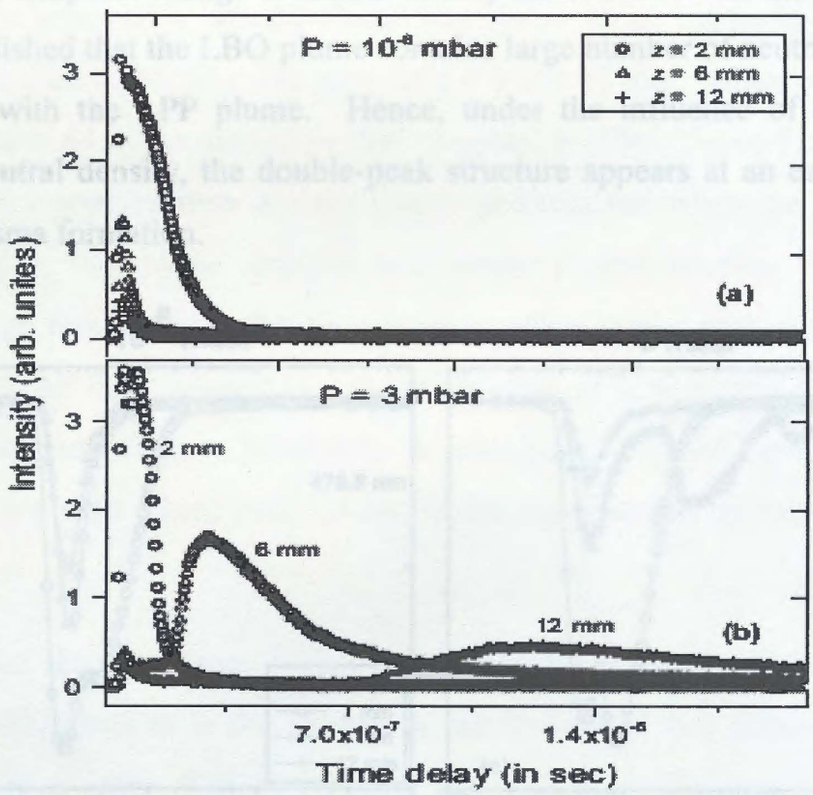

Figure 7-1 Temporal profile for CII emission line for different distance at two 10^{-6} mbar and 3 mbar argon pressures.

The electron density in the plume decreases as a function of time due to volumetric expansion of the plume. Various experimental and theoretical efforts have predicted t^{-2} and t^{-3} temporal dependence of the electron temperature and electron density respectively. The fall in electron density and electron temperature reduces the probability of the electron impact ionization/excitation, thereby drastically reducing the collisional processes in the plume. This reduction in collisional processes is evident from the reduction in intensity of temporal profiles with distance (*cf.* Figure 7-1a). Similar observations were made on lithium neutral

(Li I) and ionic (Li II) species. Figure 7-2a & Figure 7-2b show the temporal profiles for Li I and Li II at three different distances.

It has been observed that in LPP experiments, the temporal profile appears as a single-peak structure in initial stages of the plasma evolution [13-19]. In contrast to this, double-peaked structures were observed in the temporal profiles for both neutral and ionic species of lithium even in vacuum (Figure 7-2a & Figure 7-2b). The observed features in the temporal profiles are intimately related to spatial and temporal change in neutral density for both LPP and LBO plumes. It is well established that the LBO plume contains large number of neutral species in comparison with the LPP plume. Hence, under the influence of excess self-generated neutral density, the double-peak structure appears at an early stage of the LBO plasma formation.

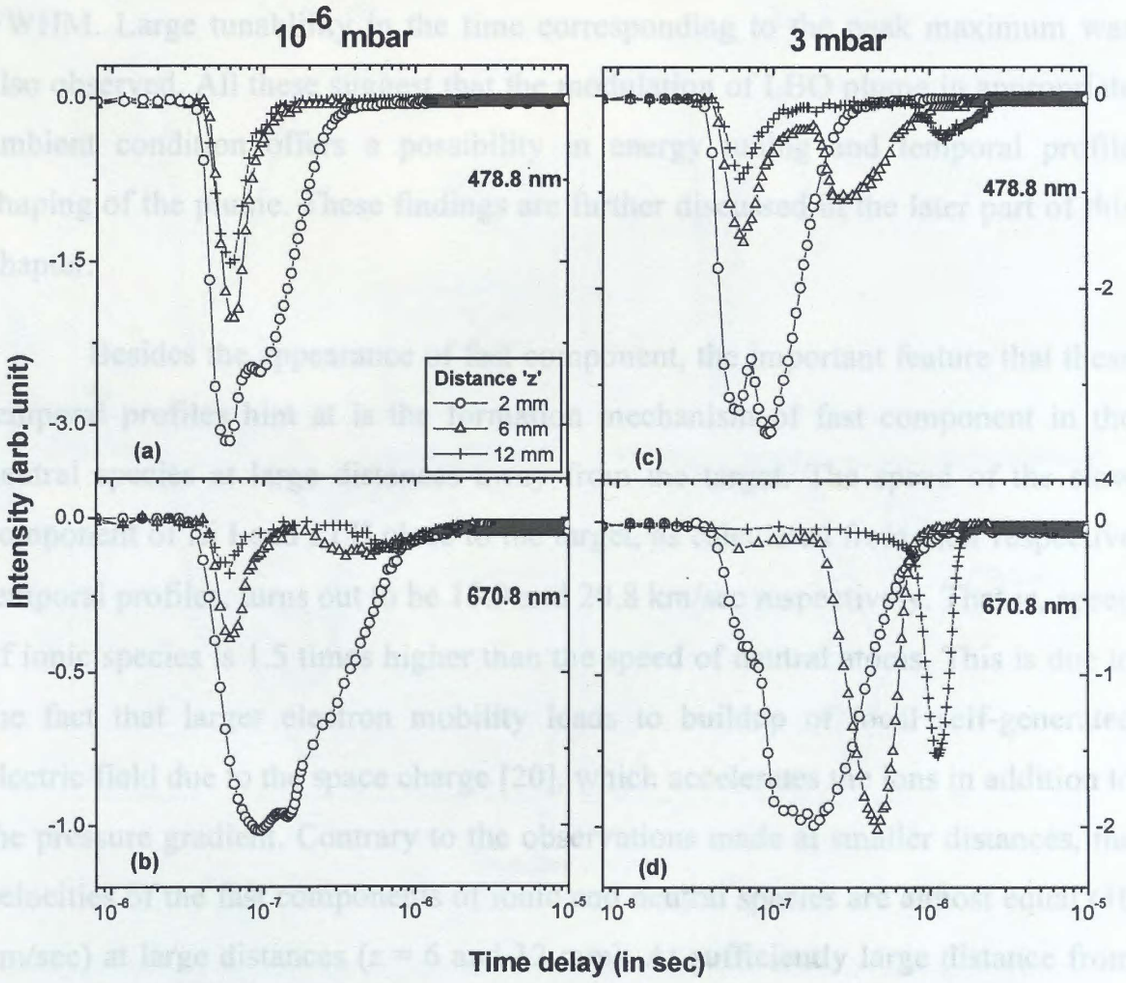

Figure 7-2 Temporal profile of Li II at 478.8nm and Li I at 670.8nm for different distance at two 10^{-6} and 3 mbar argon pressure

The origin of ions in the plume can be traced back to two fundamental processes *viz.* photo-ionization and ionization due to collisions. The ions formed by the photo-ionization have larger translational energy and constitute the ablation front of the plume. This ablation front appears as the fast component of the profile. To start with, the ionic lines are all fast, as evident single peak structure at far distances ($z > 6$ mm) from the target (figure 7.2a). However, at $z = 2$ mm (open circles in figure 7.2a), an unresolved shoulder in the ionic temporal profile suggest the presence of excessive neutrals in the plasma. At $z = 2$ mm, even at 3 mbar, not much ambient penetration into the plume was visible (open circles in figure 7.2b), whereas clear plume splitting was seen for $z = 6$ and 12 mm. An entirely different trend was observed in the case of neutral temporal profiles (figure 7.2c and 7.2d). In vacuum, the profiles were always double peaked, and when the ambient gas was introduced, they were changed into single peaked profiles with reduced FWHM. Large tunablility in the time corresponding to the peak maximum was also observed. All these suggest that the modulation of LBO plume in appropriate ambient condition offers a possibility in energy tuning and temporal profile shaping of the plume. These findings are further discussed in the later part of this chapter.

Besides the appearance of fast component, the important feature that these temporal profiles hint at is the formation mechanism of fast component in the neutral species at large distances away from the target. The speed of the slow component of Li I and Li II close to the target, as calculated from their respective temporal profiles, turns out to be 13.9 and 20.8 km/sec respectively. That is, speed of ionic species is 1.5 times higher than the speed of neutral atoms. This is due to the fact that larger electron mobility leads to buildup of local self-generated electric field due to the space charge [20], which accelerates the ions in addition to the pressure gradient. Contrary to the observations made at smaller distances, the velocities of the fast components of ionic and neutral species are almost equal (10 km/sec) at large distances ($z = 6$ and 12 mm). At sufficiently large distance from the target, electron temperature decreases rapidly, enhancing the probability of recombination processes. This observation suggests that at large distance from the

target fast component formed in Li I is mainly due to the recombination [21] of energetic ionic species.

7.2.2 Temporal profiles in ambient argon environment

The ambient environment is known to significantly affect the dynamics and propagation of the plasma plume; the major effects being plume deceleration, plume splitting and intensity enhancement of the plume. These effects modify the temporal profiles, thereby providing a means to study the influence of ambient environment on the plume dynamics. The observable features of the temporal profiles corresponding to varied distances (z) and pressures (*cf.* Figure 7-3) clearly indicate the role played by the ambient gas in governing the dynamics of the plasma plume.

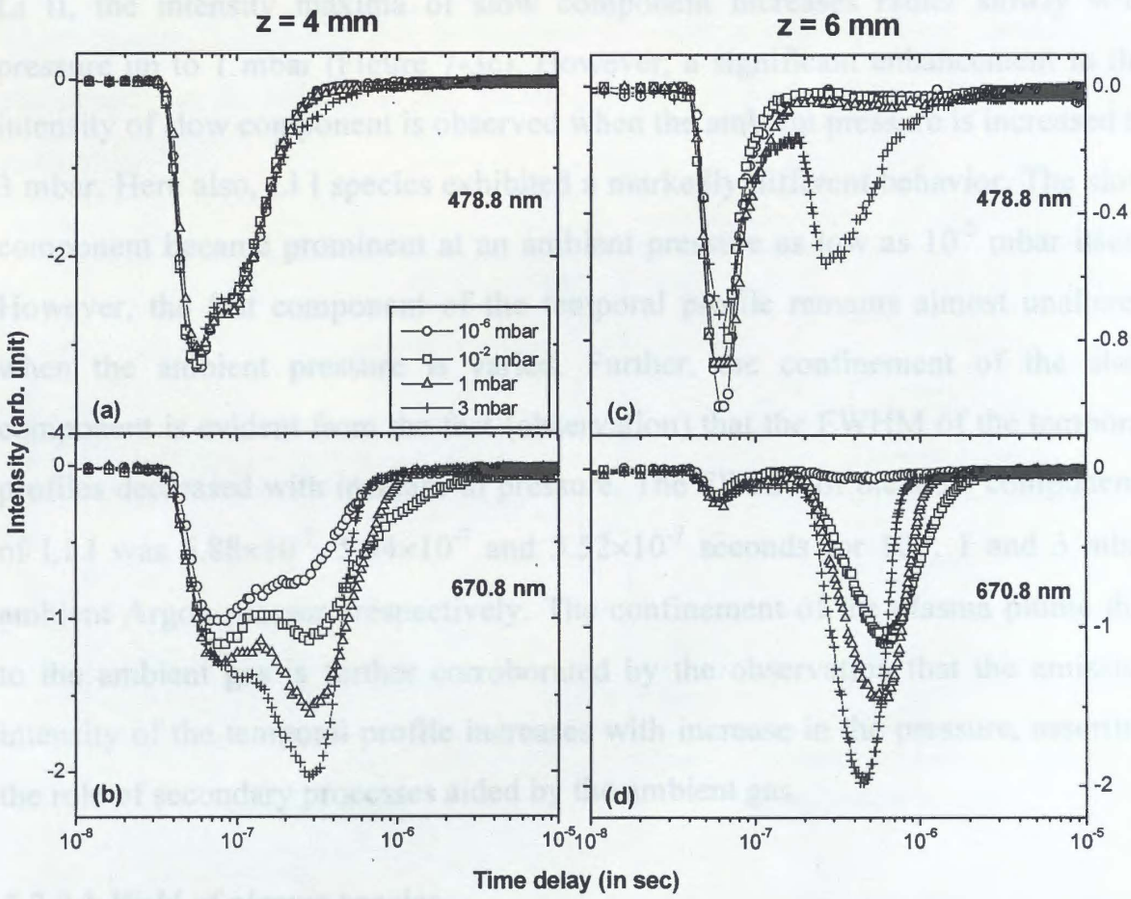

Figure 7-3 Effect of ambient gas pressure on the temporal profiles of the Li I and Li II at z = 4 mm (a and b) and z = 6 mm (c and d)

It is evident from Figure 7-3a that at z = 4 mm, the shape of the temporal profile corresponding to Li II does not change much with increase in the

background pressure. This means that at this distance the density of the plasma is high enough to prevent penetration of the ambient gas into the plume and cause deceleration of the ionic species. However, the unresolved shoulder-like structure present in the profile is due to the neutrals produced in the ablation of the thin film. The temporal profiles of C II species (not shown here) also displayed similar features. Contrary to this, the ambient gas has a profound effect on Li I species. The slow component becomes noticeable with increase in pressure. Even though the plume profiles have drastically changed, they still remain unresolved (figure 7.3b), suggesting that the plume boundary is yet not permeable to the ambient gas.

The shape of the temporal profiles of ionic and neutral species changes dramatically as the field of view is moved to a distance $z = 6$ mm away from the target. At this distance, the slow and fast components are well separated. For the Li II, the intensity maxima of slow component increases rather slowly with pressure up to 1 mbar (Figure 7-3c). However, a significant enhancement in the intensity of slow component is observed when the ambient pressure is increased to 3 mbar. Here also, Li I species exhibited a markedly different behavior. The slow component became prominent at an ambient pressure as low as 10^{-2} mbar itself. However, the fast component of the temporal profile remains almost unaltered when the ambient pressure is varied. Further, the confinement of the slow component is evident from the fact (observation) that the FWHM of the temporal profiles decreased with increase in pressure. The FWHM of the slow components of Li I was 6.88×10^{-7}, 5.34×10^{-7} and 3.52×10^{-7} seconds for 10^{-2}, 1 and 3 mbar ambient Argon pressure respectively. The confinement of the plasma plume due to the ambient gas is further corroborated by the observation that the emission intensity of the temporal profile increases with increase in the pressure, asserting the role of secondary processes aided by the ambient gas.

7.2.2.1 Yield of plasma species

As discussed in chapter 3, the intensity of the temporal profile is proportional to the plasma density. Thus the total intensity obtained by taking the whole area under the temporal profile is representative of the number of the emissive species being probed.

Figure 7-4a depicts the total intensity as a function of distance at various pressures for ionic and neutral lithium species. As evident from the figure, in vacuum, the total intensity of Li I and Li II species decreases rapidly for distances z exceeding 4 mm. At 3 mbar of argon pressure for Li II, intensity variation followed the similar trend as in the case of vacuum, but the intensity was 2-3 times higher than the observed intensity in vacuum. Presence of ambient gas strongly affects the population of excited neutral atoms. Total intensity enhancement by a factor of two with respect to the intensity observed in vacuum up to the $z = 4$ mm. At $z = 6$ mm, number of excited neutral species was 8 times higher than that in vacuum. Figure 7-4b shows intensity distribution of fast and slow component of neutral and ionic lithium atoms with respect to argon pressure at $z = 8$ mm. Intensity of the fast and slow component of Li II species increased with increase in background pressure. The physical mechanisms leading to enhancement in intensity due to increase in ambient pressure have already been explained. For the neutral atoms, intensity of fast component was almost invariant with pressure.

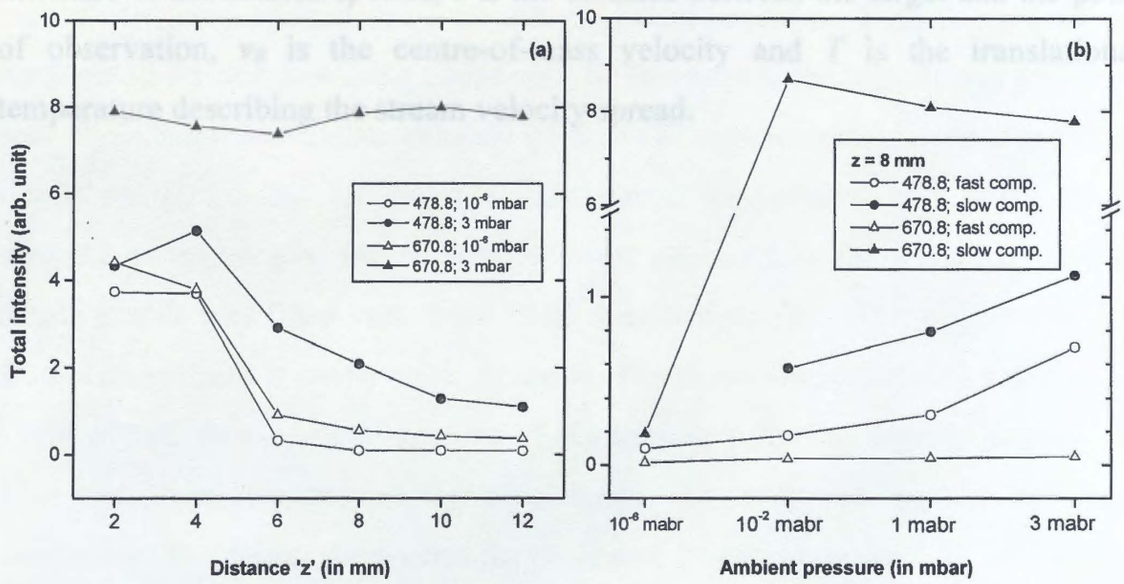

Figure 7-4 (a) Integrated yield of the emission lines at 478.8 and 670.8 nm as a function of distance 'z' from the target for 10^{-6} and 3 mbar argon pressure. (b) Variation of integrated yield of the fast and slow components for Li I and Li II lines as a function of argon pressure.

As seen in Figure 7-3d, the Li I slow component intensity was extremely sensitive to ambient gas pressure. The ratio of intensities of slow and fast components at 10^{-2} mbar pressure was ~3 and 250 respectively for ionic and

neutral species. The decreasing trend of the slow component at higher pressure (*i.e.*, at 1 and 3 mbar), might be due to the scattering loss of the ejected species at relatively higher pressure.

7.2.2.2 Shape of temporal profile

The very fact that ambient pressure has a profound effect on shape of temporal profiles, hints the role played by the ambient pressure conditions in governing the velocity distribution of the plasma species. In order to quantify the effect of ambient gas on velocity distribution of ions and neutral species, the temporal profiles were fitted with both shifted Maxwell-Boltzmann (SMB) and Gaussian distributions and a comparative study is made. The SMB distribution function to fit the time-of-flight profile is written as:

$$f(t) = At^{-4} e^{\left[\frac{-m}{2k_B T}\left(\frac{z}{t} - v_0\right)^2\right]} \tag{7.1}$$

where $f(t)$ is the intensity of emitting species, A is the normalization constant, m is the mass of the ablated species, z is the distance between the target and the point of observation, v_0 is the centre-of-mass velocity and T is the translational temperature describing the stream velocity spread.

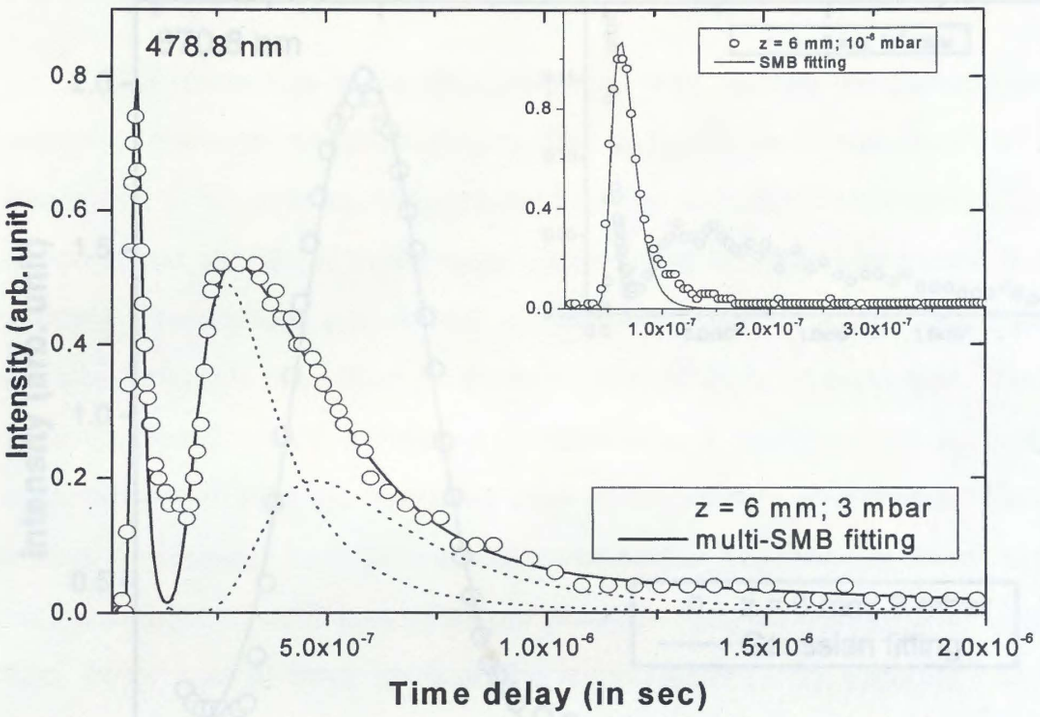

Figure 7-5 The arrival time distribution of Li II species for 10^{-6} mbar (shown in inset) and 3 mbar argon pressure. The profiles were recorded at z = 6 mm. Solid line represents the multi-SMB fit of the profiles. Doted lines represent the different components of SMB.

Figure 7-5 shows the arrival time distribution of Li II observed at 6 mm from the target in vacuum and 3 mbar background pressures. Solid line represents the SMB fit for our data using equation(7.1). In vacuum, the best fit was achieved with an average translation velocity of 8.5×10^6 cm/sec which corresponded to kinetic energy of 260 eV and the translational temperature of 1.3×10^5 K. In presence of argon gas, the slow component appeared in the emission profile. Whole profile was fitted with three SMB distributions. The fitting parameter for the fast component is nearly same as above. The slow component was found to be a sum of two time-of-flight profiles of the lithium ions. The superimposition of these two components exactly reproduced the observed profile of slow component. The fitting parameters for these two distributions are 1.2×10^6 cm/sec, 3×10^4 K and 3.5×10^5 cm/sec, 1.6×10^4 K respectively.

Different scenario was observed in arrival distribution of neutral atoms (Figure 7-6).

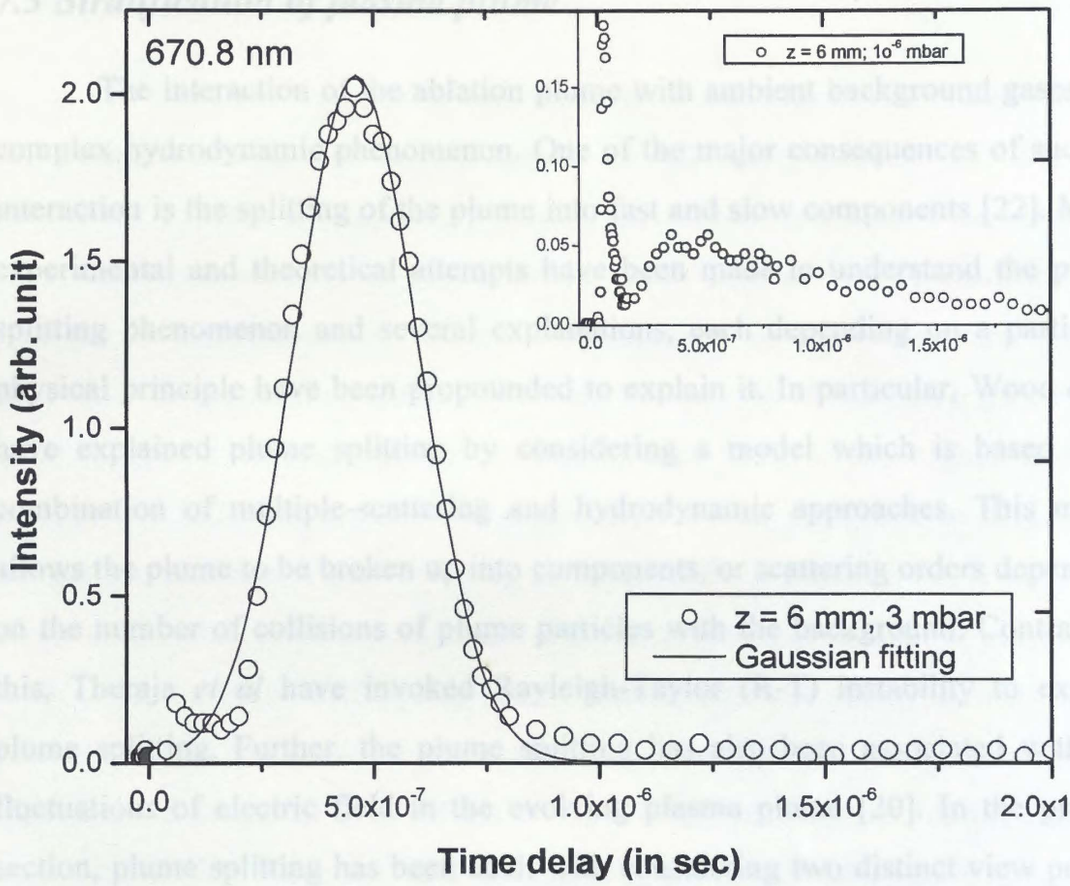

Figure 7-6 The arrival time distribution of Li I species for 10 $^{-6}$ mbar (shown in inset) and 3 mbar argon pressure. The profiles were recorded at z = 6 mm. Solid line represent the single Gaussian fit of the profiles.

The observed slow component in vacuum looked like a multi-component SMB distributions. Kinetic distribution of neutral species changed completely in presence of argon gas. Looking at the symmetric nature of the TOF profile, we attempted to fit a Gaussian distribution rather than SMB. Interestingly the profile was best fitted by a single Gaussian function. This was an important finding that, presence of relatively high pressure background gas transforms the kinetic distribution of neutral species from SMB to Gaussian distribution. Thus, we propose that this method can be well adapted for the production of good quality neutral atom beam for various applications. The absence of fast component and the symmetrically distributed species ensures that a minimal damage be done to the structure of the deposited film. This makes it useful in pulsed laser deposition of high quality film.

7.3 Stratification of plasma plume

The interaction of the ablation plume with ambient background gases is a complex hydrodynamic phenomenon. One of the major consequences of such an interaction is the splitting of the plume into fast and slow components [22]. Many experimental and theoretical attempts have been made to understand the plume splitting phenomenon and several explanations, each depending on a particular physical principle have been propounded to explain it. In particular, Wood *et al.* have explained plume splitting by considering a model which is based on a combination of multiple-scattering and hydrodynamic approaches. This model allows the plume to be broken up into components, or scattering orders depending on the number of collisions of plume particles with the background. Contrary to this, Theraja *et al* have invoked Rayleigh-Taylor (R-T) instability to explain plume splitting. Further, the plume splitting has also been associated with the fluctuations of electric field in the evolving plasma plume [20]. In the present section, plume splitting has been dealt with considering two distinct view points, one correlating the plume splitting to the change in the population of Li I and Li II in the plasma plume and another relating the plume splitting to Raleigh-Taylor instability.

7.3.1 Population dynamics of Li I and Li II species

As discussed earlier, the presence of ambient gas is known to greatly influence the temporal profiles of the expanding plume (shown in Figure 7-2c & Figure 7-2d). This clearly hints towards the role played by ambient in stratifying the plume into fast and slow components. Several authors [13, 19] have previously reported the stratification of LPP plume in presence of ambient gas. In LBO plume, major constituent is the neutral species and this necessarily implies that ambient gas is the prime source responsible for excitation/ionization of neutral atoms. The increase in emission intensity of expanding plume in background gas is mainly due two processes:

1. excitations due to collisions with background atoms

2. electron impact excitation.

Of these two cases, electron impact processes plays the dominant role in the enhancement of the excited species in expanding plasma [23, 24]. The interaction between the expanding plasma and ambient gas causes the ionization of ambient gas resulting in production of more number of free electrons. The increase in electron density leads to enhancement of excited species. This is supported by the results reported by others for the role of ionization potential of ambient gas in enhancement of excited species [25], where higher emission intensity of LPP was observed in argon environment compared to helium and oxygen environment. Again referring to Figure 7-3c & Figure 7-3d, it was noted that enhancement of slow component is more pronounced for Li I in comparison with Li II. As stated earlier, the second component was mainly formed by the electron impact excitation or ionization of neutral species. Energy required for excitation of neutral Li at 670.8 nm ($^2S_{1/2} - {}^2P^0_{1/2}$ transition) is 1.8 eV, which is much lower than both the first ionization potential of Li (5.36 eV) and the excitation energy of Li II ion (2.56 eV) at 478.8 nm ($^1P^0_1 - {}^1D_2$ transition). The electron impact single ionization cross section of neutral Li is about $5\times10^{-}16$ cm^2 for typically 15 eV impact energy [26]. For the same impact energy, the excitation cross-section of Li I ($^2S_{1/2} - {}^2P^0_{1/2}$ transition) is about 40×10^{-16} cm^2 [26]. This means that excitation cross section is 8 times higher than the ionization cross-section. All the analysis discussed above based on atomic data is in agreement with the observed result and it is ascertained that the electron impact processes favor the enhanced population of excited neutral atom.

The above phenomenon may give rise to two different mechanisms for the front and core expansion of the plasma. The plasma front mainly represents the highly energetic ions, which expand freely in ambient environment, while the slow component that represents the core of the plasma (mainly the neutral species) undergoes nonlinear expansion in ambient environment. The formation of Li II ions by two different mechanisms can produce two different velocity distributions. The ions formed by the direct ablation have larger transnational energy (due to the absorption of laser light) forming the leading edge of the

plume, which penetrates the ambient gas without much attenuation. The slow component comes from the ions formed by mainly collisional ionization of the neutral atoms moving with much low translational energy as compared to its fast counterpart. We have already discussed the reason why ambient gas effect is more pronounced on the slow component of neutral species. In addition, after the laser interaction ceases, the charge composition of the plasma is mainly controlled by the balance between electron impact ionization and three body recombination processes. Since the speed of the plasma front is high, the interaction time for the three-body recombination is very low. Still, at higher pressures, effect of three-body recombination is visible in the form of a slow decrease in intensity of the fast component for L II and appearance of fast component for Li I.

The stratification of expanding plume as function of ambient gas pressure and distance form the target has been reported in literature [13, 19]. Our finding shows that in between z = 4 and 6 mm, there is a transition point where the plume species begin to experience the interaction with the background gas atoms. The collision starts when the plume dimensions are of the order of the mean free path of the ejected species. From the kinetic theory of gases [27], the mean free path of the atom with mass M_s traveling through a gas consisting of atoms of mass M_g is

$$\lambda^{-1} = \sqrt{2}\,\pi N_s \sigma_s^2 + \frac{\pi N_g}{4}\left(\sigma_s + \sigma_g\right)^2 \sqrt{\left(1+\frac{M_s}{M_g}\right)} \tag{7.2}$$

where N_s, N_g are the numbers per unit volume of the sputtered (atoms sputtered from target due to laser ablation) and gas atoms and σ_s, σ_g are the atomic diameters of sputtered and gas atoms respectively. In most cases $N_s \ll N_g$ and hence the above equation reduces to

$$\lambda^{-1} = 8.34\times10^{14}\,\rho\,\frac{\left(\sigma_s + \sigma_g\right)^2}{4}\sqrt{\left(1+\frac{M_s}{M_g}\right)} \tag{7.3}$$

where ρ is the pressure of the sputtering gas in Pascal.

Applying the relation (7.2) in present context, the mean free path of sputtered lithium atom at 5×10^{-2} mbar argon ambient pressure was estimated to be 4.8 mm. This is in good agreement with observed collisional region. Further, the average angular deviation and the relative loss of kinetic energy suffered by the sputtered particles is given by

$$\langle \cos\theta \rangle = \begin{cases} 1-\dfrac{M^2}{3}, & for \quad M<1 \\ \dfrac{2}{3M}, & for \quad M>1 \end{cases} \tag{7.4}$$

$$\langle w \rangle = \begin{cases} 1-\left[\dfrac{(1-M)^2}{2M}\right]\log\left[\dfrac{1+M}{1-M}\right], & for \quad M<1 \\ 1-\left[\dfrac{(M-1)^2}{2M}\right]\log\left[\dfrac{M+1}{M-1}\right], & for \quad M>1 \end{cases} \tag{7.5}$$

$$where\ w=\log\left(\frac{E^1}{E}\right) \quad and \quad M\equiv\frac{M_g}{M_s}$$

In the present case, where Li atoms collide with argon atom, the direction of Li atom changed by 83° and it lost about 27% of its kinetic energy [27]. Therefore in the present experiment, z = 6 mm is the distance where the collision between the plume species and background atoms begins. In this region, a model proposed by Wood *et al* [28] explains the plume splitting based on momentum transferred between the plume species and background atoms. They concluded that, if the mass of the plume species is much lower than the background atoms (as in the present case of Li and Ar) then, even single collisions are enough to retard plume atoms significantly.

7.3.2 Rayleigh-Taylor instability

A detailed study of plasma expansion in the low pressure range (less than 10^{-3} Torr) has shown that the plasma plume remains relatively homogenous during its course of evolution. The evolution of plasma in this regime is marked by rapid decrease in plasma ion density, largely due to expansion and recombination processes, which enables interpenetration of plasma and ambient gas. Such interpenetration leads to transfer of kinetic energy and momentum via ion-ion Coulomb scattering, ion-neutral collisions, charge-transfer interactions, etc. The constant expansion velocity of the plume front is characteristic of evolution of plume in this regime. In the present experiment, free expansion of plume is evident from the distance Vs. time plot shown in Figure 7-7a.

As pressure is raised from 10^{-3} Torr to ~0.1 Torr, partial confinement of high density plasma plume takes place reducing the penetration of ambient gas into the plume. Such a confinement of plume leads to the formation of an interface demarcating plasma plume from the ambient gas. The confinement effect of the ambient gas is illustrated in Figure 7-3d which depicts temporal profiles at 10^{-2}, 1 and 3 mbar argon pressure. Alternatively, one can say that as ambient pressure increases the plasma makes a transit from free expansion regime to collisional regime. The temporal profile for Li I at 10^{-2} mbar argon pressure and z = 6 mm demonstrates the plasma expansion in collisional regime (Figure 7-3d and Figure 7-7a).

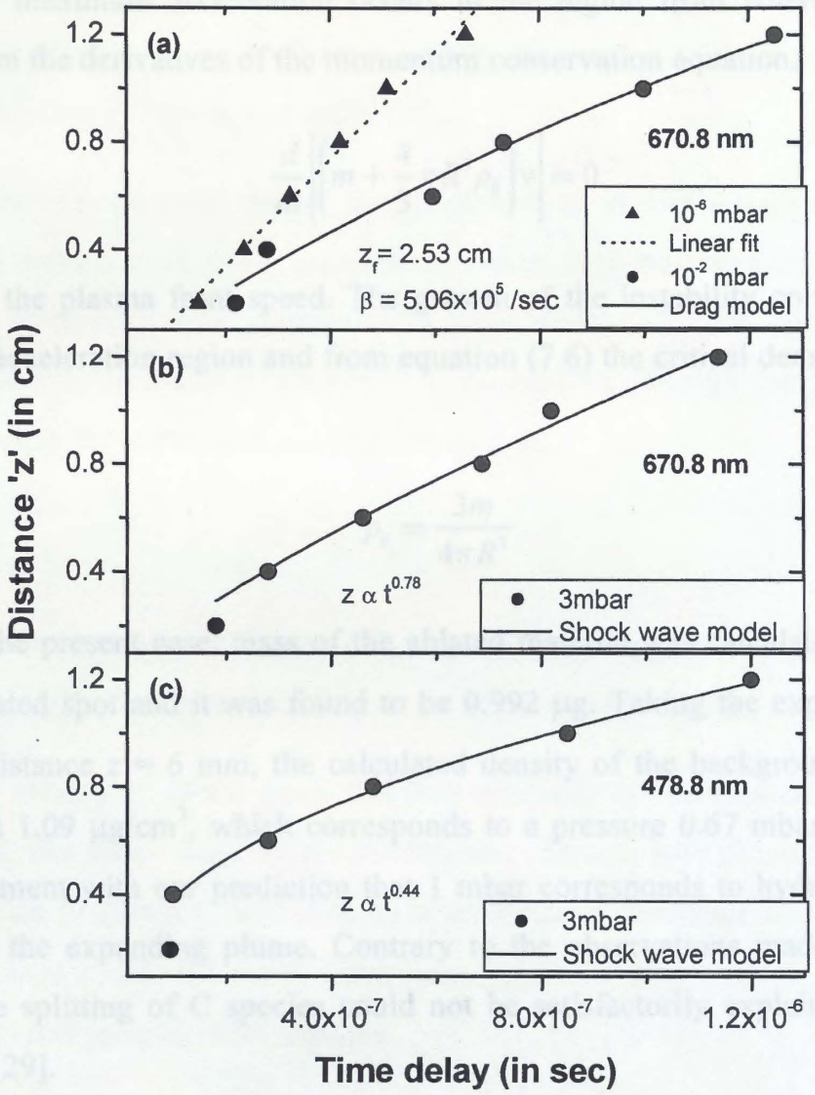

Figure 7-7 Distance from target vs. time (z-t) plot for slow component of Li I and Li II emission line. (a) The dash and solid curve represents the best fit of the experimental data for Li I in accordance with linear fit and drag model for pressure 10^{-6} and 10^{-2} mbar respectively. Data for Li I (b) and Li II (c) are fitted with shock wave model at 3 mbar pressure.

When a contact boundary is formed the plume expansion is better described by the laws of continuum fluid dynamics. In the present context, the prevailing condition of plume-gas interaction can be viewed as a heavy fluid (plume) resting on lighter fluid (ambient gas). Furthermore, the density fluctuations at the interface region lead to deceleration of plasma front finally causing the stratification of the plasma plume into fast and slow component. The stratification of plume is adjudged from appearance of fast and slow peaks in the temporal profile. In present experiment, the background gas density which produces the R-T instability was estimated at approximately 6 mm from the target surface.

The maximum acceleration occurs in the region from where it can be derived from the derivatives of the momentum conservation equation.

$$\frac{d}{dt}\left[\left(m+\frac{4}{3}\pi R^3\rho_b\right)v\right]=0 \tag{7.6}$$

where v is the plasma front speed. The growth of the instability corresponds to maximum acceleration region and from equation (7.6) the critical density is given by

$$\rho_b=\frac{3m}{4\pi R^3} \tag{7.7}$$

In the present case, mass of the ablated material was calculated from the size of ablated spot and it was found to be 0.992 μg. Taking the experimentally observed distance z = 6 mm, the calculated density of the background gas was obtained as 1.09 μg/cm^3, which corresponds to a pressure 0.67 mbar. This is in good agreement with our prediction that 1 mbar corresponds to hydrodynamical regime for the expanding plume. Contrary to the observations made on the Li species, the splitting of C species could not be satisfactorily explained by R–T instability [29].

7.4 Expansion dynamics of plasma plume

As discussed earlier, the interaction between the plume and ambient gas causes the slowing down of the speed of ablated species. The plume expansion dynamics in a different gas environment are explained with two models; the shock wave and the drag force model. For sufficiently high pressures, where the ablated mass is small compared to the mass of the background gas in motion, a shock front is formed and its propagation is given by [30],

$$z=\left(\frac{E_0}{\rho_b}\right)^{\frac{1}{5}} t^{\frac{2}{5}}+z_0 \tag{7.8}$$

where z is the distance from the target, E_0 is the constant proportional to the laser energy density and z_0 is the distance moved by the species for a time of the order of average lifetime of the excited states [25].

In the second case, where the ejected mass is much greater than the background mass (*i.e.* at lower ambient pressure), slowing down of the ejected species can be treated under classical drag force model [31]. The ejected species experience a viscous force proportional to its velocity through the background gas. In this case, the expansion can be expressed as

$$z = z_f\left[1 - e^{-\beta t}\right] + z_0 \tag{7.9}$$

where β is the slowing coefficient and z_f is the stopping distance of the plume. That is, $z_f = v_0/\beta$; v_0 being the initial velocity of the ejected species.

The validity of shock wave and drag model in the present case has been investigated. The shock wave model has limiting characteristic distance R_1, below which equation (7.8) is not valid [32]. R_1 is set by the requirement that the mass of the gas encompassed by the shock wave (in volume=$2/3\ \pi R^3$) is much greater than the initial ablated mass m. This requires

$$R_1 \geq R = \left(\frac{3m}{2\pi\rho_b}\right)^{\frac{1}{3}} \tag{7.10}$$

Taking the ablated mass m =0.992 μg, the lower limit for the validity of shock wave with our experimental parameter was estimated. We get the value of R as 28 mm, 6 mm and 4.9 mm for the background gas pressure 10^{-2}, 1 and 3 mbar respectively. This means that, most part of the plume dynamics for 10^{-2} and 1 mbar pressure follow the drag model for the considered distances from target. For 3 mbar pressure, where the estimation shows that after z = 4.9 mm, the second component follow the shock wave expansion. The shock wave type expansion is clearly seen in Figure 7-3d, where at 3 mbar, the time delay of the second component suffered a reversal. The observed acceleration is due to the generation of shock wave at this pressure.

To support the above interpretation, we have reported the dependence of time when the maximum intensity occur on the distance from the target (shown in Figure 7-7).

The linear dependence of the time delay with the distance in vacuum suggested the free expansion of lithium neutral atom (Figure 7-7a). The linear fit of the data gave the average expansion velocity for the slow component of Li I as 1.9×10^{6} cm/sec corresponding to the kinetic energy 13 eV. Depending on ambient pressure condition, the experimental data were analyzed using appropriate model based on our estimation. For gas pressure 10^{-2} mbar, the maximum intensity of the slow component is fitted with drag force model (Figure 7-7a).

The best fitting parameter gives slowing coefficient β equal to 5.06×10^{5}/sec and stopping distance equal to 2.53 cm. At 3 mbar (higher pressure regime), we have attempted to fit our experimental results with the shock wave model for $z \geq 4$ mm (Figure 7-7b & Figure 7-7c). A slight deviation from the perfect shock wave expansion ($R \propto t^{0.4}$) was observed. The slow component of Li I and Li II followed the $R \propto t^{0.78}$ and $R \propto t^{0.44}$ dependence respectively.

7.5 Effect of laser fluence

It was found that laser fluence strongly affect the dynamics as well as intensity distributions of the ejected species. Temporal profiles for Li I and Li II at $z = 2$ mm in vacuum at various laser fluence are shown in Figure 7-8. At $z = 2$ mm, the total intensity of the ionic species were nearly unchanged with increase in laser fluence. However, the intensity of the slow component of Li II reduced with increase in laser fluence. It was also observed that the fast and slow components were better resolved at higher laser fluence. With reduction in the FWHM, the plumes were more confined at higher laser fluence. As for neutrals at low laser fluence, the Li I distribution profile appeared as a single peak structure and the yield was found to be substantially higher in comparison with higher fluence. In addition, with increasing laser fluence, temporal profile broadened with an elongated tail distribution. The tail elongation may be due to the cluster formation [33].

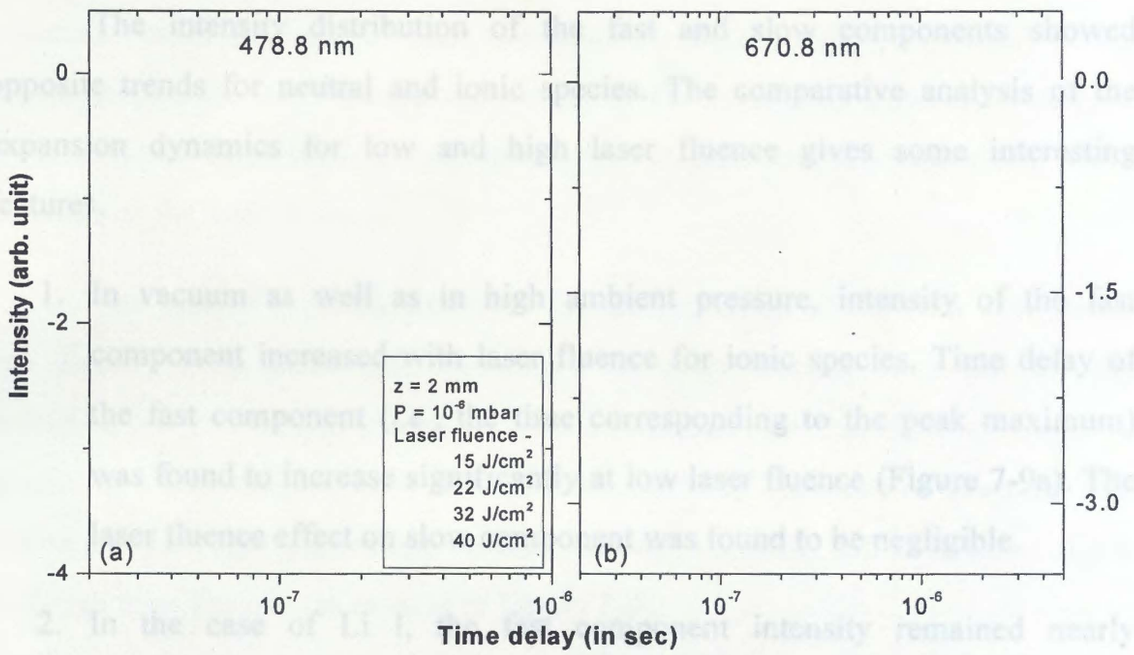

Figure 7-8 Effect of laser fluence on the temporal profiles of Li II (a) and Li I (b) lines in vacuum at z = 2 mm from the target.

For verifying fluence effect on expansion, we have presented the temporal distribution of ionic and neutral species in two different environment at z = 8 mm (shown in Figure 7-9).

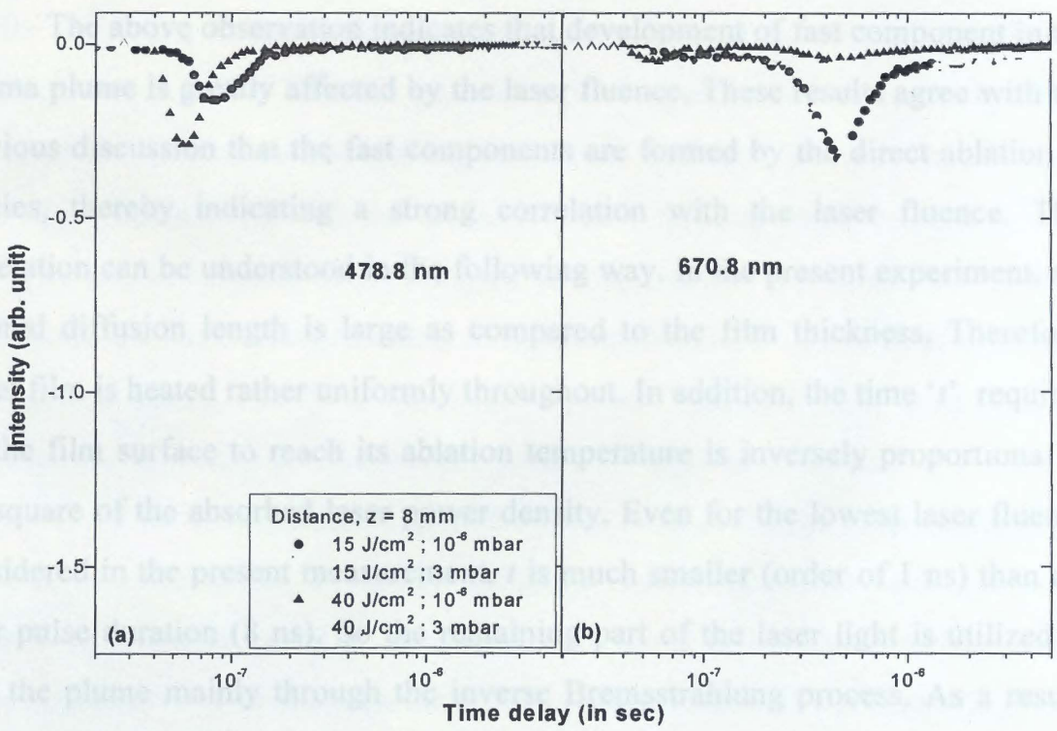

Figure 7-9 The effect of low and high laser fluence on the time-of-flight profiles of Li II (a) and Li I (b) in two different ambient pressures at z = 12 mm.

The intensity distribution of the fast and slow components showed opposite trends for neutral and ionic species. The comparative analysis of the expansion dynamics for low and high laser fluence gives some interesting features.

1. In vacuum as well as in high ambient pressure, intensity of the fast component increased with laser fluence for ionic species. Time delay of the fast component (*i.e.*, the time corresponding to the peak maximum) was found to increase significantly at low laser fluence (Figure 7-9a). The laser fluence effect on slow component was found to be negligible.

2. In the case of Li I, the fast component intensity remained nearly unchanged with respect to laser fluence at 3 mbar pressure. However, the yield of the slow component reduced with increase of fluence in both environments; that is, in vacuum and 3 mbar argon pressure.

3. The separation between fast and slow components for Li I at 3 mbar pressure was found to increase with laser fluence.

The above observation indicates that development of fast component in the plasma plume is greatly affected by the laser fluence. These results agree with the previous discussion that the fast components are formed by the direct ablation of species, thereby indicating a strong correlation with the laser fluence. This correlation can be understood in the following way. In the present experiment, the thermal diffusion length is large as compared to the film thickness. Therefore, target film is heated rather uniformly throughout. In addition, the time 't' required for the film surface to reach its ablation temperature is inversely proportional to the square of the absorbed laser power density. Even for the lowest laser fluence considered in the present measurement, t is much smaller (order of 1 ns) than the laser pulse duration (8 ns). So the remaining part of the laser light is utilized to heat the plume mainly through the inverse Bremsstrahlung process. As a result, probability of ionization is large for higher laser fluence. It is worth mentioning here that multi-photon ionization cross section is directly proportional to the power density of the laser light, which also supports the observed results. Free

expansion model [18] was invoked to explain the dependence of time delay of fast component on the laser fluence. According to this model, the terminal velocity of expansion of ablated particles is proportional to square root of temperature, which depends on the laser fluence.

The role of collision processes for the formation of the slow component has already been discussed. Therefore, the laser fluence does not directly influence the distribution profile of slow component. As the number of ablated species is a constant, increase in ionization results in depletion of neutrals. This explains the inverse relationship in intensities of Li II (fast) and Li I (slow) at low and high laser fluence (as evident in Figure 7-9).

7.6 Conclusion

Time- and space-resolved spectroscopy of the LBO plume from the multicomponent LiF–C thin film demonstrated interesting features in its evolution dynamics, which are quite different from the plume evolution in LPP experiments. The plume profile at short distance in vacuum is generally regarded as a single profile. However, in our experiment we observed signatures of unresolved slow component even at z = 2 mm in vacuum as well as at 3 mbar pressure. We have estimated the onset of collision of ambient atoms with the plume species at z = 4.8 mm, which agrees well with the dramatic plume splitting observed in $4 \leq z \leq 6$ mm. The plume splitting of Li I started at low ambient pressures ~10^{-2} mbar), whereas collisional effects resulting in the formation of Li II set in at only high pressures (3 mbar). The SMB model for time of flight of ions at large distance suggests that it retains its Maxwellian nature throughout its course of evolution. The neutral time-of-flight distribution showed a distinct change in its nature in the presence of ambient gas. The single Gaussian representation for neutral time-of-flight distribution observed in our experiment seems to have potential for wide-range applications. Our study on the effect of laser fluence on the temporal profile sheds more light on the formation of the fast and slow components in LBO plumes. The increase of the fast component of Li II at higher laser fluence clearly suggests that the plume front is composed of mainly primary ions. We have also

observed that the yield of neutral atoms is higher, and the time-of-flight distribution is a unimodel function in the case of low laser fluence ablation.

References

1. Adrian F. J., Bohandy J., Kim B. F., Jette A. N., and Thompson P., (1987). "A study of the mechanism of metal deposition by the laser-induced forward transfer process". *Journal of Vacuum Science & Technology B: Microelectronics and Nanometer Structures*, **5**(5): pp. 1490-1494.

2. Baseman R. J. and Froberg N. M., (1989). "Time-resolved transmission of thin gold films during laser blow-off". *Applied Physics Letters*, **55**(18): pp. 1841-1843.

3. Amoruso S., Bruzzese R., Spinelli N., and Velotta R., (1999). "Characterization of laser-ablation plasmas". *Journal of Physics B: Atomic, Molecular and Optical Physics*, **32**(14): pp. R131-R172.

4. Lie Y. T., Pospieszczyk A., and Tagle J. A., (1983). "Use and production of suprathermal atomic beams for the diagnostics of the scrap-off layer of Tokamaks." *Fusion Technology*, **6**(2 pt 2): pp. 447-452.

5. Suckewer S., Cecchi J., Cohen S., Fonck R., and Hinnov E., (1980). "Tracer element injection into PDX tokamak for spectral line identification and localized doppler temperature measurement". *Physics Letters A*, **80**(4): pp. 259-262.

6. Hinnov E., Suckewer S., Cohen S., and Sato K., (1982). "Observed transitions in n=2 ground-state configurations of copper, nickel, iron, chromium, and germanium in tokamak discharges". *Physical Review A*, **25**(4): pp. 2293-2301.

7. Mattioli M., Michelis C. D., and Pecquet A. L., (1998). "Laser blow-off injected impurity transport in L mode Tore Supra plasmas". *Nuclear Fusion*, **38**(11): pp. 1629-1635.

8. Pospieszczyk A., Aumayr F., Bay H. L., Hintz E., Leismann P., Lit Y. T., Ross G. G., Rusbuldt D., Schorn R. P., Schweer B., and Winter H., (1989). "Recent developments for plasma edge diagnostics using atomic beams". *Journal of Nuclear Materials*, **162-164**: pp. 574-581.

9. Koppmann R., Refaei S. M., and Pospieszczyk A., (1986). "Spectroscopic study of atomic beams generated by laser ablation of multicomponent targets". *Journal of Vacuum Science & Technology A: Vacuum, Surfaces, and Films*, **4**(1): pp. 79-85.

10. Iijima S. and Ichihashi T., (1993). "Single-shell carbon nanotubes of 1-nm diameter". *Nature*, **363**(6430): pp. 603-605.

11. Kroto H. W., Heath J. R., O'Brien S. C., Curl R. F., and Smalley R. E., (1985). "C60: Buckminsterfullerene". *Nature*, **318**(6042): pp. 162-163.

12. Lowndes D. H., Geohegan D. B., Puretzky A. A., Norton D. P., and Rouleau C. M., (1996). "Synthesis of Novel Thin-Film Materials by Pulsed Laser Deposition". *Science*, **273**(5277): pp. 898-903.

13. Amoruso S., Bruzzese R., Spinelli N., Velotta R., Vitiello M., and Wang X., (2003). "Dynamics of laser-ablated MgB_2 plasma expanding in argon probed by optical emission spectroscopy". *Physical Review B*, **67**(22): pp. 224503.

14. Bakos J. S., Ignacz P. N., Szigeti J., and Kovacs J., (1987). "Laser blow-off plasma propagating in low-pressure gas". *Applied Physics Letters*, **51**(10): pp. 734-736.

15. Baseman R. J., Froberg N. M., Andreshak J. C., and Schlesinger Z., (1990). "Minimum fluence for laser blow-off of thin gold films at 248 and 532 nm". *Applied Physics Letters*, **56**(15): pp. 1412-1414.

16. Bullock A. B. and Bolton P. R., (1999). "Laser-induced back ablation of aluminum thin films using picosecond laser pulses". *Journal of Applied Physics*, **85**(1): pp. 460-465.

17. Hermann J., Thomann A. L., Boulmer-Leborgne C., Dubreuil B., De Giorgi M. L., Perrone A., Luches A., and Mihailescu I. N., (1995). "Plasma diagnostics in pulsed laser TiN layer deposition". *Journal of Applied Physics*, **77**(7): pp. 2928-2936.

18. Singh R. K., Holland O. W., and Narayan J., (1990). "Theoretical model for deposition of superconducting thin films using pulsed laser evaporation technique". *Journal of Applied Physics*, **68**(1): pp. 233-247.

19. Harilal S. S., O'Shay B., Tao Y., and Tillack M. S., (2006). "Ambient gas effects on the dynamics of laser-produced tin plume expansion". *Journal of Applied Physics*, **99**(8): pp. 083303.

20. Gurevich A. V., Parriskaya L. V., and Pitaevskii L. P., (1973). *Sov. Phys. JETP*, **36**: pp. 274.

21. Rumsby P. T. and Paul J. W. M., (1974). "Temperature and density of an expanding laser produced plasma". *Plasma Physics*, **16**: pp. 247-260.

22. Geohegan D. B. and Puretzky A. A., (1996). "Laser ablation plume thermalization dynamics in background gases: combined imaging, optical absorption and emission spectroscopy, and ion probe measurements". *Applied Surface Science Proceedings of Symposium F: Third International Symposium on Laser Ablation of the 1995 E-MRS Spring Conference*, **96-98**: pp. 131-138.

23. Timmer C., Srivastava S. K., Hall T. E., and Fucaloro A. F., (1991). "Enhanced line emission from laser-produced plasmas". *Journal of Applied Physics*, **70**(3): pp. 1888-1890.

24. Gu H. P., Lou Q. H., Cheung N. H., Chen S. C., Wang Z. Y., and Lin P. K., (1994). "Experimental study of enhanced emission of the laser-ablated plume in backing gas". *Applied Physics B: Lasers and Optics*, **58**(2): pp. 143-148.

25. Gonzalo J., Vega F., and Afonso C. N., (1995). "Plasma expansion dynamics in reactive and inert atmospheres during laser ablation of Bi(2)Sr(2)Ca(1)Cu(2)O(7 - y)". *Journal of Applied Physics*, **77**(12): pp. 6588-6593.

26. McFarland and H. R., (1965). "Gryzinacuteski Electron-Impact Ionization Cross-Section Computations for the Alkali Metals". *Physical Review*, **139**(1A): pp. A40-A42.

27. Westwood W. D., (1978). "Calculation of deposition rates in diode sputtering systems". *Journal of Vacuum Science and Technology*, **15**(1): pp. 1-9.

28. Wood R. F., Leboeuf J. N., Geohegan D. B., Puretzky A. A., and Chen K. R., (1998). "Dynamics of plume propagation and splitting during pulsed-laser ablation of Si in He and Ar". *Physical Review B*, **58**(3): pp. 1533-1543.

29. Kumar A., Singh R. K., Subramanian K. P., Patel B. G., Sunil S., and Prajapati I. A., (2006). "Effects of ambient pressure and laser fluence on the temporal evolution of 426.7 nm CII line in laser-blow-off of multilayered LiF-C thin film". *Journal of Physics D: Applied Physics*, **39**(22): pp. 4860-4866.

30. Kumuduni W. K. A., Nakayama Y., Nakata Y., Okada T., and Maeda M., (1993). "Transport of YO molecules produced by ArF laser ablation of $YBa_2Cu_3O_{7-x}$ in ambient oxygen gas". *Journal of Applied Physics*, **74**(12): pp. 7510-7516.

31. Kools J. C. S., (1993). "Monte Carlo simulations of the transport of laser-ablated atoms in a diluted gas". *Journal of Applied Physics*, **74**(10): pp. 6401-6406.

32. Dyer P. E. and Sidhu J., (1988). "Spectroscopic and fast photographic studies of excimer laser polymer ablation". *Journal of Applied Physics*, **64**(9): pp. 4657-4663.

33. Kroto H. W., Allaf A. W., and Balm S. P., (1991). "C60: Buckminsterfullerene". *Chemical Reviews*, **91**(6): pp. 1213-1235.

Chapter 8
Summary and future prospects

8.1 Summary

The present thesis by and large deals with the evolution of plasma plume in vacuum and in presence of ambient gas. The major outcomes of the thesis are summarized here:

- The expansion of plasma in vacuum could be distinctly categorized in two phases. The plasma front initially accelerated and the free expansion of the plasma front ensued only after around 6 mm away from the target. Further, the plasma front did not follow the inverse square root of the atomic mass. However, the inverse square root dependence of the plasma front velocity on the mass of plasma species was found to improve considerably if one included the translational temperature as determined from the temporal profiles.
- The expansion of plasma in ambient pressure comprised three stages. Initially when whole of the plume energy is in form of thermal energy, the plasma front showed acceleration. Subsequently, the expansion of plasma front followed point blast wave model and drag model. The transition of the expansion law from point blast wave model to drag model depended on the mass of the plasma species. For plasma of heavy metal (lead) this transition occurred at a distance very large compared to the corresponding distance for lighter metal (Aluminum).
- The component specific analysis of the temporal profiles corresponding to plasma plume evolving in vacuum have shown that the neutral plasma species consists of slow, medium and fast components. Each of these components follows a SMB velocity distribution. A logistic approach to numerically isolate the components has also been suggested.

- Time and space resolved studies of the laser blow off plasma have shown that the evolution of this plasma to differ considerably from the plasma plume of solid targets. The temporal profiles of the solid target at smaller distances are known to be consisting of single peak. However, for laser blow off plasma the temporal profiles showed double peak structure in vacuum as well as at 3 mbar pressures at distances as low as 2 mm.

- Important phenomena like plume splitting, intensity enhancement, and onset of Rayleigh-Taylor instability were studied from the view point of the role of ambient pressure in governing the plume dynamics. The plume splitting of LiI, as inferred from the appearance of slower peak in the temporal profile, began at ambient pressures as low as 10^{-2} mbar, while the collisional effects resulting in the formation of Li II set in at only high pressures 3 mbar. The confinement effects of the ambient pressures on the plasma plume were also observed.

- Besides the evolution dynamics, the ambient pressure was found to have a profound effect on the velocity distribution of the neutral species of the plasma plume. The neutral species followed a SMB velocity distribution during expansion in vacuum. However, as the ambient pressure was increased to 3 mbar, the velocity distribution transformed from asymmetric SMB distribution to Symmetric Gaussian like velocity distribution. No such effect was observed for the ionic species.

- A detailed study of the effect of laser fluence on the plume dynamics have revealed a lot on the causative mechanisms leading to the splitting of plume into fast and slow components. The increase of the fast component of LiII with the increase in laser fluence at the target surface has convincingly proved that the plume front, which is represented by the fast component, consists mainly of the ions formed by direct ionization due to laser. Further, the yield of the neutral species was found to increase with decrease in the incident laser fluence. Also, the temporal profiles corresponding to neutral species were unimodal at low laser fluences.

8.2 Future prospects

Our findings have unambiguously explained the origin of the fast component and its dependence on the laser fluence. In the current studies the thickness of the film was considerably smaller as compared to the thermal diffusivity of the target. As a result only a small fraction of laser energy is used to vaporize the target and majority of the energy is used to ionize the neutral atom of the vapor cloud. In this context it is worthwhile to explore the effect of the thickness of the carbon and LiF layer on the yield of neutral and ionic species of the plasma.

The LiF-C plasma was analyzed without considering the chemical kinematics of plume. In order to convincingly attribute the fast component to the primary ionization of the neutrals by laser, similar experiments are planned to be performed on single component targets with varying thickness.

The electron-impact processes have known to be a key factor in controlling the neutral populations in plasma. Besides this, the electrons have also been identified as the prime source coupling the laser energy to the internal energy of the plasma by means of IB. In this context, it is would be interesting to investigate the efficiency of electron in igniting the plasma by injecting low energy electrons in the core of ablated cloud when the laser pulse persist.